

**Exploring Myelin Water Imaging:  
from Application to Atlases to Algorithms**

by

Hanwen Liu

B.Sc., Wilfrid Laurier University, 2010

M.Sc., University of Waterloo, 2013

A THESIS SUBMITTED IN PARTIAL FULFILLMENT  
OF THE REQUIREMENTS FOR THE DEGREE OF

**Doctor of Philosophy**

in

THE FACULTY OF GRADUATE AND POSTDOCTORAL  
STUDIES

(Physics)

The University of British Columbia

(Vancouver)

November 2020

© Hanwen Liu, 2020

The following individuals certify that they have read, and recommend to the Faculty of Graduate and Postdoctoral Studies for acceptance, the thesis entitled:

**Exploring Myelin Water Imaging:  
from Application to Atlases to Algorithms**

submitted by **Hanwen Liu** in partial fulfillment of the requirements for the degree of **Doctor of Philosophy in Physics**.

**Examining Committee:**

Cornelia Laule, Department of Physics & Astronomy and Department of Radiology  
*Supervisor*

John Kramer, Department of Kinesiology  
*Co-supervisor*

Roger Tam, Department of Radiology and Department of Biomedical Engineering  
*Supervisory Committee Member*

Stefan Reinsberg, Department of Physics & Astronomy  
*University Examiner*

Zhen Jane Wang, Department of Electrical and Computer Engineering  
*University Examiner*

Greg Stanisiz, Department of Medical Biophysics, University of Toronto  
*External Examiner*

**Additional Supervisory Committee Members:**

Qing-San Xiang, Department of Physics & Astronomy and Department of Radiology  
*Supervisory Committee Member*

David Li, Department of Radiology  
*Supervisory Committee Member*

Piotr Kozlowski, Department of Radiology  
*Supervisory Committee Member*

# Abstract

Myelin water imaging (MWI) is a quantitative magnetic resonance (MR) method that specifically measures the myelin content in the central nervous system. MWI operates on the principle that the MR signal of water trapped between myelin bilayers can be extracted from the total MR signal based on a characteristic short  $T_2$  relaxation time. The ratio of myelin water signal relative to the total signal is termed myelin water fraction (MWF), used as a quantitative biomarker for myelin. This thesis explores three aspects of MWI: application, atlases, and algorithms.

Firstly, the MWI was applied to study cervical spondylotic myelopathy (CSM), which is a common spinal cord neurodegenerative disease. The function of the spinal cord conduction was assessed by an electrophysiologic technique called somatosensory evoked potentials (SSEP). Significant MWF reduction was observed in those CSM patients with functional deficits (e.g. delayed SSEP latency). A linear correlation between the MWF and the SSEP latency was discovered in CSM.

Secondly, the MWI atlases, which represent the MWI normative references of the normal myelin distribution in the brain and spinal cord, were created by co-registering and averaging the MWI images acquired from many healthy volunteers. These resulting atlases were utilized to demonstrate areas of demyelination in individuals with pathological conditions such as multiple sclerosis. The MWI atlases have been uploaded on the Internet and made publicly available.

Thirdly, the current MWI data analysis, based on the non-negative least squares (NNLS) method, was accelerated by implementing the neural network (NN) algorithm. A NN model was trained by the ground truth labels produced by the commonly used NNLS method. The trained NN model achieved to yield a whole-brain MWF map in 33 seconds, which is  $150\times$  faster than the NNLS method.

Finally, a novel  $T_2$  data analysis method, namely the spectrum analysis for multiple exponentials via experimental condition oriented simulation (SAME-ECOS), was proposed. SAME-ECOS is a simulation-derived solver that tailored for different MR experimental conditions. When dealing with the MWI data, it is found that SAME-ECOS largely surpassed the NNLS method in terms of calculation accuracy and speed.

# Lay Summary

Myelin is the protective sheath around nerve fibres or axons, which is often damaged in many neurological diseases. An advanced technique called myelin water imaging can map the myelin content in human brains and spinal cords. This thesis presents how myelin water imaging works and demonstrates its application in a common spinal cord disease. Then, the thesis focuses on two challenges of myelin water imaging: (1) the analysis result is hard to tell if the myelin is damaged for a person since the myelin content can vary among people; (2) current data analysis takes too much time (in hours) and is not very accurate. Our idea to overcome these challenges is to (1) create standard myelin templates or maps showing what the pattern (where and how much) of myelin content is supposed to be in the healthy brain and spinal cord. (2) use artificial intelligence technology to calculate more accurate results more rapidly.

# Preface

The work presented in this thesis was carried out under the co-supervision of Dr. Cornelia Laule and Dr. John Kramer. I also received constructive guidance from other members of my supervisory committee, including Dr. Qing-San Xiang, Dr. Roger Tam, Dr. David Li, and Dr. Piotr Kozlowski. All data were collected by the Philips 3T scanners in the MRI Research Center of the University of British Columbia, in accordance with the Declaration of Helsinki and approved by the local ethics board (UBC CREB #H06-00282).

A version of Chapter 2 has been published as **Liu H, MacMillian EL, Jutzeler CR, Ljungberg E, MacKay AL, Kolind SH, Mädler B, Li DK, Dvorak MF, Curt A, Laule C, Kramer JL. Assessing structure and function of myelin in cervical spondylotic myelopathy: evidence of demyelination. *Neurology*. 89(6):602-10. Aug 2017.** The study design and data collection of this chapter were completed in 2009 by Dr. Armin Curt, Dr. John Kramer, Dr. Cornelia Laule, Dr. Erin MacMillian, Dr. Alex MacKay, Dr. Burkhard Madler, Dr. David Li, and Dr. Marcel Dvorak. I was responsible for the development of the analysis methodology, image processing, statistical analysis, results interpretation, and manuscript composition. Dr. Catherine Jutzeler helped with statistical analysis and drafted sections 2.2.3, 2.2.4, and 2.2.8. Dr. David Li helped with clinical assessment for all study participants. All co-authors provided helpful feedback on the intellectual content of the manuscript draft. Dr. John Kramer and Dr. Cornelia Laule were the supervisory authors involved throughout the project.

A version of Chapter 3 has been published as **Liu H, Ljungberg E, Dvorak AV, Lee LE, Yik JT, MacMillan EL, Barlow L, Li DK, Traboulsee A, Kolind SH, Kramer JL, Laule C. Myelin Water Fraction and Intra/Extracellular Wa-**

**ter Geometric Mean T<sub>2</sub> Normative Atlases for the Cervical Spinal Cord from 3T MRI. Journal of Neuroimaging. 30(1):50-57. Aug 2019.** Dr. Cornelia Laule and I conceived the idea of creating an atlas for myelin water imaging during an email discussion with Emil Ljungberg, Dr. Shannon Kolind, and Dr. John Kramer in Jun 2016. Dr. John Kramer, Dr. Cornelia Laule, Dr. Shannon Kolind, Emil Ljungberg, and I designed the study details and collected the data. I was also responsible for image processing, statistical analysis, results interpretation, and manuscript composition. My colleagues Adam Dvorak and Jackie Yik helped with the image processing. All co-authors provided helpful feedback on the intellectual content of the manuscript draft. Dr. John Kramer and Dr. Cornelia Laule were the supervisory authors involved throughout the project.

A version of Chapter 4 has been published as **Liu H, Rubino C, Dvorak AV, Jarrett M, Ljungberg E, Vavasour IM, Lee LE, Kolind SH, MacMillan EL, Traboulsee A, Lang DJ, Rauscher A, Li DKB, MacKay AL, Boyd LA, Kramer JL, Laule C. Myelin Water Atlas: A Template for Myelin Distribution in the Brain. Journal of Neuroimaging. 29(6):699-706. Nov 2019.** The idea of this chapter was conceived by all of my supervisory committee members during a committee meeting in May 2017. The study details were primarily designed by Dr. Cornelia Laule, Dr. Shannon Kolind, and me. Data were contributed from Dr. Lara Boyd's group, Dr. Shannon Kolind's group, Dr. Anthony Traboulsee's group, and Dr. Alexander Rauscher's group. I was responsible for image processing, statistical analysis, results interpretation, and manuscript composition. All co-authors provided helpful feedback on the intellectual content of the manuscript draft. Dr. Cornelia Laule was the supervisory author involved throughout the project.

A version of Chapter 5 has been published as **Liu H, Xiang QS, Tam R, Dvorak AV, MacKay AL, Kolind SH, Traboulsee A, Vavasour IM, Li DK, Kramer JK, Laule C. Myelin water imaging data analysis in less than one minute. NeuroImage. 210:116551. Apr 2020.** Dr. Qing-San Xiang and I conceived the idea of this chapter during a conversation in Sept 2018. Dr. Cornelia Laule and I designed the study details. I was also responsible for data collection, image processing, statistical analysis, results interpretation, and manuscript composition. Dr. Shannon Kolind and Adam Dvorak helped with the data collection from a second scanner in the MRI Research Center. Dr. Roger Tam had insightful suggestions on

training the deep learning neural network models. All co-authors provided helpful feedback on the intellectual content of the manuscript draft. Dr. Cornelia Laule was the supervisory author involved throughout the project.

A version of Chapter 6 has been uploaded to arXiv as **Liu H, Xiang QS, Tam R, Kozlowski P, Li DKB, MacKay AL, Kramer JK, Laule C. Introduction to a novel  $T_2$  relaxation analysis method SAME-ECOS: Spectrum Analysis for Multiple Exponentials via Experimental Condition Oriented Simulation. arXiv preprint arXiv:2009.06761.** I conceived the idea and the study design of this chapter on the SkyTrain during many times of commuting between my home and office in 2019. I was also responsible for model construction, data collection, image processing, statistical analysis, results interpretation, and manuscript composition. Dr. Qing-San Xiang and Dr. Alex MacKay had insightful suggestions on the MR data simulation. All co-authors provided helpful feedback on the intellectual content of the manuscript draft. Dr. John Kramer and Dr. Cornelia Laule provided very helpful guidance throughout the project.

# Table of Contents

<b>Abstract</b> . . . . .	<b>iii</b>
<b>Lay Summary</b> . . . . .	<b>v</b>
<b>Preface</b> . . . . .	<b>vi</b>
<b>Table of Contents</b> . . . . .	<b>ix</b>
<b>List of Tables</b> . . . . .	<b>xiv</b>
<b>List of Figures</b> . . . . .	<b>xvi</b>
<b>Acknowledgments</b> . . . . .	<b>xxvi</b>
<b>1 Introduction</b> . . . . .	<b>1</b>
1.1 Magnetic resonance imaging . . . . .	1
1.1.1 Nuclear magnetic resonance . . . . .	1
1.1.2 Bloch equation . . . . .	2
1.1.3 Spin echo . . . . .	6
1.1.4 Spatial encoding and k-space . . . . .	8
1.2 Myelin water imaging . . . . .	14
1.2.1 Background of myelin . . . . .	15
1.2.2 Background of myelin water imaging . . . . .	18
1.2.3 Data acquisition . . . . .	19
1.2.4 Data analysis . . . . .	21
1.2.5 MWI limitations . . . . .	24

1.3	Neural networks . . . . .	25
1.3.1	Feedforward neural network architecture . . . . .	25
1.3.2	Backward propagation training . . . . .	28
1.3.3	Training strategy . . . . .	33
1.4	Thesis overview . . . . .	33
<b>2</b>	<b>Assessing structure and function of myelin in cervical spondylotic myelopathy: Evidence of demyelination . . . . .</b>	<b>36</b>
2.1	Introduction . . . . .	36
2.2	Methods . . . . .	38
2.2.1	Standard Protocol Approvals, Registrations, and Patient Consents . . . . .	38
2.2.2	Participants . . . . .	38
2.2.3	Clinical assessments . . . . .	38
2.2.4	Electrophysiology . . . . .	39
2.2.5	MRI experiments . . . . .	39
2.2.6	MWI Data Analysis . . . . .	40
2.2.7	Compression Ratio, MSCC and MCC . . . . .	40
2.2.8	Statistical Analysis . . . . .	41
2.3	RESULTS . . . . .	43
2.3.1	Participants . . . . .	43
2.3.2	Neuroimaging: Structural and signal changes at the spinal cord . . . . .	43
2.3.3	Neurophysiological assessments: Changes in spinal conduction and associations with conventional MRI outcomes . . . . .	44
2.3.4	Myelin damage in CSM patients: Relationship between neurophysiological and neuroimaging parameters . . . . .	46
2.4	Discussion . . . . .	46
2.5	Conclusion . . . . .	49
<b>3</b>	<b>Myelin water atlas for the spinal cord at 3T MRI . . . . .</b>	<b>50</b>
3.1	Introduction . . . . .	50
3.2	Methods . . . . .	53

3.2.1	Subject information . . . . .	53
3.2.2	MRI experiments . . . . .	53
3.2.3	Myelin water fraction and geometric mean $T_2$ . . . . .	53
3.2.4	Myelin water fraction atlas and geometric mean $T_2$ atlases . . . . .	54
3.2.5	Z-score maps for RRMS subjects . . . . .	55
3.3	Results . . . . .	55
3.3.1	Myelin water fraction atlas and geometric mean $T_2$ atlas . . . . .	55
3.3.2	Z-score maps for RRMS participants . . . . .	57
3.4	Discussion . . . . .	57
3.5	Conclusion . . . . .	61
<b>4</b>	<b>Myelin water atlas for the brain at 3T MRI . . . . .</b>	<b>63</b>
4.1	Introduction . . . . .	63
4.2	Methods . . . . .	65
4.2.1	Participants and MR Experiments . . . . .	65
4.2.2	Data Analysis . . . . .	65
4.3	Results . . . . .	67
4.4	Discussion . . . . .	69
4.5	Conclusion . . . . .	74
<b>5</b>	<b>Acceleration of myelin water imaging data analysis via neural network algorithm . . . . .</b>	<b>76</b>
5.1	Introduction . . . . .	76
5.2	Methods . . . . .	80
5.2.1	MWI data acquisition and pre-processing . . . . .	80
5.2.2	Ground truth . . . . .	81
5.2.3	Neural network model and model training . . . . .	82
5.2.4	Trained model evaluation . . . . .	84
5.2.5	Normalized data training . . . . .	85
5.3	Results . . . . .	85
5.3.1	MWF calculation time . . . . .	85
5.3.2	Healthy brains . . . . .	85
5.3.3	MS lesions . . . . .	87

5.3.4	Spinal cord . . . . .	87
5.3.5	Data from a different scanner . . . . .	88
5.3.6	Robustness of the trained model . . . . .	89
5.4	Discussion . . . . .	90
5.4.1	Prediction accuracy . . . . .	90
5.4.2	NN_opt vs. NN_norm . . . . .	92
5.4.3	Trained NN_opt sensitivity to flip angle and SNR . . . . .	94
5.4.4	Implementation: NN vs. NNLS . . . . .	94
5.4.5	Limitations of current model . . . . .	95
5.4.6	Other quantitative MRI techniques . . . . .	96
5.4.7	Comparison to kernel regression . . . . .	96
5.5	Conclusion . . . . .	97
<b>6</b>	<b>Novel T<sub>2</sub> data analysis method: SAME-ECOS . . . . .</b>	<b>99</b>
6.1	Introduction . . . . .	99
6.2	Methods . . . . .	102
6.2.1	In-vivo MRI experiment . . . . .	102
6.2.2	SAME-ECOS workflow . . . . .	102
6.2.3	SAME-ECOS model performance evaluation . . . . .	106
6.2.4	Apply SAME-ECOS to experimental data . . . . .	107
6.3	Results . . . . .	108
6.3.1	Performance evaluation via simulation tests . . . . .	108
6.3.2	In-vivo experimental data: MWF maps . . . . .	111
6.4	Discussion . . . . .	112
6.4.1	SAME-ECOS vs. NNLS . . . . .	112
6.4.2	Advantages of SAME-ECOS . . . . .	115
6.4.3	Disadvantages of SAME-ECOS . . . . .	117
6.4.4	Other quantitative MRI techniques and beyond . . . . .	118
6.5	Conclusion . . . . .	118
<b>7</b>	<b>Conclusion and future work . . . . .</b>	<b>120</b>
7.1	Chapters recap . . . . .	120
7.1.1	MWI applied in CSM . . . . .	120

7.1.2	MWI atlases . . . . .	121
7.1.3	MWI data analysis acceleration . . . . .	121
7.1.4	MWI data analysis accuracy improvement . . . . .	121
7.2	Contributions of the thesis . . . . .	122
7.3	Limitations of the thesis . . . . .	122
7.4	Future work . . . . .	124
	<b>Bibliography . . . . .</b>	<b>128</b>

# List of Tables

Table 2.1	<b>Demographic, neuroimaging, and neurophysiologic details of the study cohorts.</b> Abbreviations: CSM = cervical spondylotic myelopathy; JOA = Japanese Orthopaedic Association; SSEP = somatosensory evoked potential. Results are displayed as mean±SD. . . . .	44
Table 4.1	<b>Summary of myelin water fraction (MWF) in different regions of interest in white matter for all subjects, and males and females separately.</b> P-value indicates comparison between male and female participants. All regions of interest (ROI) from 50 participants are tested for normality (Shapiro-Wilk W statistics). . . . .	68
Table 4.2	<b>Pairwise comparisons (paired t-test) of myelin water fraction (MWF) between 7 white matter regions in healthy subjects.</b> Bonferroni correction (significant level: $p < 0.002$ ) was used to corrected for multiple comparisons. . . . .	72
Table 5.1	<b>Validation loss of 7 NN models.</b> 7 candidate NN models with different hidden layers were constructed and trained respectively. The training stopped when the validation loss (mean squared error) did not decrease for 100 epochs. . . . .	84
Table 5.2	<b>Summary of results for the two testing healthy brains.</b> Absolute and relative differences were evaluated. . . . .	87

Table 6.1 **Four pre-defined ground truth spectra.** The  $T_2$  locations of each spectrum are selected obeying the resolution limit. Amplitudes are normalized to one. . . . . 107

# List of Figures

Figure 1.1	<b>Schematics of the NMR phenomenon.</b> At equilibrium, the magnetization $M$ initially aligns with the direction of external magnetic field $B$ . After being excited by a $90^\circ$ RF pulse, $M$ is tipped to the transverse plane, followed by $T_2$ decay and $T_1$ recovery immediately. This figure is attributed to Arijit Hazra. [78] . . . . .	4
Figure 1.2	<b>Time evolution of longitudinal and transverse magnetization.</b> (a) The rate of longitudinal recovery is governed by $T_1$ . (b) The rate of transverse relaxation is governed by $T_2$ . . . . .	5
Figure 1.3	<b>Carr–Purcell sequence showing the first two echoes in the rotating frame.</b> (a) Excitation by a $90^\circ$ RF pulse; (b) spin dephasing; (c) spin flipped by a $180^\circ$ RF pulse; (d) spin rephasing; (e) spin refocused to form a spin echo; (f)–(i) formation of the second echo. This figure is attributed to Richard Ansorge. [7] . . . . .	7
Figure 1.4	<b>Illustration of phase encoding.</b> The induction signal of the element is phase shifted at each cycle after a different phase encoding ( $k_{y,1}, k_{y,2}, k_{y,3}\dots$ ). If the amplitude of the induction signal is recorded at the same time for every cycle and plotted in the $k_y$ axis, then the composite oscillation will have a frequency that is equal to the rate of phase shift $f_{\phi,y}$ . . . . .	11

Figure 1.5	<b>Spin-echo (SE) MRI sequence (A) and k-space (B) &amp; (C).</b> The $90^\circ$ RF pulse is applied with gradient $G_z$ on to select a slice. Initially, the k-space filling takes the trajectory from $1 \rightarrow 2$ due to the gradients $G_y$ and $G_x$ (from 1 to 2 in (A)); $2 \rightarrow 3$ due to the $180^\circ$ pulse (the curved line is only for visualization); $3 \rightarrow 4$ due to the gradient $G_x$ (from 3 to 4 in (A)) while recording the data at the same time. The cycle is repeated with a different $G_y$ at each time. TE: echo time; TR, repetition time; ACQ: analog-to-digital converter. This figure is attributed to Kiruluta. [99] . . . . .	13
Figure 1.6	<b>Examples of MRI image contrast.</b> Brain images with contrasts of $T_1$ -weighting, $T_2$ -weighting, and PD-weighting are presented in axial view. This Figure is attributed to Tamir. [208]	15
Figure 1.7	<b>Neuron anatomy.</b> The figure is attributed to Quasar Jarosz at English Wikipedia. [36] The length of an axon ranges from millimeters to meters. . . . .	16
Figure 1.8	<b>Grey and white matter.</b> This figure is attributed to Mandira P. at Socratic Q&A. [150] . . . . .	16
Figure 1.9	<b>Transmission electron micrograph of a myelinated axon.</b> This figure is attributed to Electron Microscopy Facility at Trinity College, Hartford, Connecticut. [188] . . . . .	17
Figure 1.10	<b>The concept of myelin water imaging (MWI).</b> The $T_2$ decay curve is analyzed by non-negative least squares (NNLS) to obtain the $T_2$ distribution, from which the myelin water fraction (MWF) is calculated. . . . .	19
Figure 1.11	<b>Multi-echo spin echo (MSE) sequence.</b> A slice selective $90^\circ$ excitation pulse is followed by a series of non-selective $180^\circ$ refocusing pulses. Crushers with alternating polarity and varying amplitude are applied before and after the refocusing pulse. $G_{SS}$ : slice selection gradient; $G_{PE}$ : phase encoding gradient; $G_{FE}$ : frequency encoding gradient. This figure is attributed to Alonso-Ortiz. [6] . . . . .	21

Figure 1.12	<b>Gradient and spin echo (GRASE) sequence.</b> A selective $90^\circ$ is followed by a series of selective $180^\circ$ refocusing pulses. Each spin echo is sandwiched by two gradient echoes. $G_{SS}$ : slice selection gradient; $G_{PE}$ : phase encoding gradient; $G_{FE}$ : frequency encoding gradient. This figure is attributed to Alonso-Oritz. [6] . . . . .	22
Figure 1.13	<b>Anatomy of a neural network node.</b> A node takes inputs $(x_1, x_2, \dots, x_n)$ , performs some calculations with them, and produces one output $a$ . . . . .	26
Figure 1.14	<b>A typical neural network architecture.</b> A NN consists of an input layer to take the input data, a number of hidden layers to perform calculations, and an output layer to yield the result. . . . .	27
Figure 1.15	<b>Backward propagation.</b> A tree diagram depicts the backward propagation mechanism. . . . .	29
Figure 1.16	<b>Overview of the thesis.</b> . . . . .	34
Figure 2.1	<b>Work flow chart.</b> One example is depicted here for calculating the average MWF in the whole cord and dorsal column. . . . .	41
Figure 2.2	<b>Calculations of conventional MRI parameters and comparisons between healthy controls and CSM patients.</b> (A) & (B): The methods for calculating compression ratio, maximum spinal cord compression (MSCC) and maximum canal compromise (MCC). $D_1$ : transverse diameter; $D_2$ : anterior-posterior diameter; $D_i$ ( $d_i$ ): canal (spinal cord) diameter at compression level; $D_a$ ( $d_a$ ): canal (spinal cord) diameter of non-compressed level from above; $D_b$ ( $d_b$ ): canal (spinal cord) diameter of non-compressed level from below. (C) Significant differences were observed in compression ratio, maximum spinal cord compression (MSCC) and maximum canal compromise (MCC) between healthy controls and CSM patients. . . . .	42

Figure 2.3	<b>MWF and SSEPs comparisons between healthy controls and CSM patients (A), and interaction effect (B).</b>	A): Myelin water fraction (MWF) (whole cord and dorsal column) and tibial SSEP latencies (left and right) between healthy controls and CSM patients are compared. No differences were observed between groups. B) An interaction between the interpretation of tibial SSEPs ('pathology'/'normal') the diagnosis of CSM ('yes'/'no') was observed for MWF of the whole cord. Patients with CSM and pathological tibial SSEPs had reduced MWF (indicated by *).	45
Figure 2.4	<b>Correlations between SSEPs and MWF in CSM patients and healthy controls.</b>	Correlations of tibial SSEPs (left and right) with dorsal column and whole cord myelin water fraction (MWF) in CSM participants (A-D) and healthy controls (E-H). Significant correlations are only found in CSM group (trend lines are fitted R-Squared and p-value). No correlations are observed in healthy controls.	48
Figure 3.1	<b>MWF atlas and IEGMT<sub>2</sub> atlas.</b>	The resulting myelin water fraction (MWF) atlas and geometric mean T <sub>2</sub> (IEGMT <sub>2</sub> ) atlas of all 8 slices from C2 to C3. Averaged anatomical images (mFFE) are also displayed.	56

Figure 3.2	<b>Comparison of z-score maps from 3 relapsing remitting multiple sclerosis (RRMS) subjects.</b>	Z-score maps were calculated based on myelin water fraction (MWF) and $T_2$ times of the intra- and extra-cellular (IE) water (IEGMT <sub>2</sub> ) atlases and their standard deviation for C2 to C3 cord and representative slices are presented in sagittal, coronal, and axial view. Sagittal and coronal views are showing at the middle of the cord, and axial view are showing at C2 and C3 levels. Axial slices are also thresholded for regions of significance ( $z < -1.96$ or $z > 1.96$ ) and displayed on MWF and IEGMT <sub>2</sub> atlases respectively. An average of all 50 axial z-score maps is also shown for each participant. Axial anatomical multi-echo fast field echo (mFFE) images are shown to compare with the z score maps at different levels. . . . .	58
Figure 3.3	<b>Compare MWF and IEGMT<sub>2</sub> atlases with individual metric maps.</b>	In this illustrative example, the created atlases showed much better image quality and contrast between structures compared to individual myelin water fraction (MWF) and geometric mean $T_2$ (IEGMT <sub>2</sub> ) maps of 5 subjects. All slices are shown at the same level. . . . .	59
Figure 4.1	<b>Workflow chart.</b>	Myelin water fraction (MWF) map of each individual subject was registered to standard space of MNI152 T <sub>1</sub> 1 mm brain. A myelin water atlas was created by averaging all registered MWF maps from the 50 healthy participants. . .	66
Figure 4.2	<b>Myelin water atlas.</b>	Four representative axial slices of myelin water fraction (MWF) from the resulting myelin water atlas (in grayscale and colormap [color scale: 0 – 0.2]), the corresponding SD maps, the voxel-wise normality test P-value (color scale: 0 – 0.05), and the voxel-wise P-value (color scale: 0 – 0.05) of t-test between males and females MWF are shown and compared to a T <sub>1</sub> structural 1 mm brain (MNI152). . . . .	69

Figure 4.3 **Myelin water fraction of different regions of interest (ROIs) in white matter in healthy participants.** The box plot shows the myelin water fraction (MWF) in forceps major, forceps minor, corpus callosum splenium, corpus callosum genu, corpus callosum body, anterior limb of internal capsule, and posterior limb of internal capsule for 50 healthy adults. Each line is connecting the data points from the same participant to trace the MWF variations in different ROIs across an individual. Similar patterns of variation between regions were present for all participants. . . . . 70

Figure 4.4 **Z-score maps for three individuals with multiple sclerosis.** (A) T<sub>2</sub>-weighted images in individual space of three relapsing remitting multiple sclerosis (MS) participants with lesions indicated by arrows; (B) proton density weighted images in individual space; (C) corresponding z-score maps (color scale: -5 to 5); and (D) z-score maps thresholded for significant reduction ( $z < -1.96$ , uncorrelated, color scale: -5 to 0). Regions with coefficient of variation (mean divided by standard deviation) larger than 0.75 were excluded. MS subject 1 was a 25-year-old female with expanded disability status score (EDSS) = 0. MS subjects 2 and 3 were 26-year-old females with EDSS = 2.0. MS subject 3 demonstrates the most extensive global demyelination. . . . . 71

Figure 5.1	<b>Schematic of workflow.</b> 32-echo data from 5 brains (4 healthy, 1 multiple sclerosis (MS)) were used for training. Two healthy brains, 1 MS brain with segmented lesions, and 1 spinal cord acquired by the same scanner were used as testing data. One healthy brain acquired by a different scanner were also used for testing. The ground truth was calculated by regularized non-negative least squares (NNLS) with stimulated echo correction. The neural network was constructed with fully connected layers (activation function: ReLU, optimizer: Adam, loss: mean square error). . . . .	83
Figure 5.2	<b>Visual comparison of brain MWF maps.</b> The brain MWF maps carried out by the neural network models (NN_opt and NN_norm) and the NNLS ground truth, as well as the error map between the two are shown side by side for 4 representative axial slices from healthy brain #1. Note that NN_opt was trained by non-normalized data while NN_norm was trained by normalized data. . . . .	86
Figure 5.3	<b>Voxel-wise comparison of MWF within six different brain ROIs.</b> ROIs include all gray matter, all white matter, corpus callosum, corticospinal tract, forceps major, and forceps minor from healthy brain #2. R-square, p values from paired t-test, and mean absolute errors (MAE) were evaluated. . . . .	88
Figure 5.4	<b>MWF comparison for lesions.</b> The lesion mask was first manually drawn on the proton density image of a MS brain and then registered to the GRASE space. MWF maps carried out by the trained neural network model (NN_opt) and the NNLS ground truth are visually the same. Highly significant voxel-wise MWF correlation between NN_opt and NNLS is shown for the lesions. . . . .	89

Figure 5.5	<b>Comparison of spinal cord MWF.</b> The MWF maps of a healthy spinal cord were carried out by the neural network model (NN_opt) and the NNLS ground truth. No visual differences or regional biases were found. Excellent voxel-wise MWF correlation between NN_opt and NNLS was observed in the spinal cord. . . . .	90
Figure 5.6	<b>Analysis of brain data acquired by a different scanner.</b> The brain MWF maps carried out by the neural network models (NN_opt and NN_norm) and the NNLS ground truth, as well as the error maps are shown side by side for one representative axial slice from a healthy brain data collected by a different scanner (Philips Elition). Note that NN_opt was trained by non-normalized data while NN_norm was trained by normalized data. . . . .	91
Figure 5.7	<b>Neural network prediction error vs. flip angle.</b> The actual refocusing flip angle deviates from the prescribed 180 degrees due to B1 inhomogeneity. The voxel-wise flip angle was estimated using extended phase graph algorithm. The neural network (NN_opt) prediction error is plotted against the actual flip angle. . . . .	92
Figure 5.8	<b>Neural network prediction at different SNR levels.</b> Additional noise is injected at SNR = 100 and SNR = 50. Neural network (NN_opt) predictions are compared with NNLS ground truth. MWF and its error maps of one representative axial slice are shown. . . . .	93
Figure 6.1	<b>SAME-ECOS workflow.</b> . . . . .	101

Figure 6.2	<p><b>T<sub>2</sub> spectra produced by SAME-ECOS (blue) and NNLS (red) respectively are compared with the ground truth spectra (green).</b> Simulated decay data, which are generated from 4 pre-defined ground truth spectra (<b>Table 1</b>) each with 100 different noise realizations, are fed into the trained SAME-ECOS model and NNLS algorithm to generate the T<sub>2</sub> spectra. Faded gray lines indicate the produced spectra for each noise realization. The mean and standard deviation of cosine similarity scores of 100 realizations are shown for each sub-figure. . . .</p>	109
Figure 6.3	<p><b>Myelin water fraction (MWF) produced by SAME-ECOS (blue) and NNLS (red) are compared with the ground truth MWF (green).</b> 10,000 randomly simulated decay data examples were analyzed by SAME-ECOS and NNLS respectively. The MWF (fraction of signal with T<sub>2</sub>s &lt; 40ms) was extracted from each predicted spectrum. . . . .</p>	110
Figure 6.4	<p><b>Flip angle (FA) dependence of myelin water fraction (MWF) prediction errors.</b> 10,000 randomly simulated decay data examples were analyzed by SAME-ECOS and NNLS. Errors of MWF (fraction of signal with T<sub>2</sub>s &lt; 40ms) was calculated and compared with FA. The mean error of each FA was also presented for a visual check for biases. . . . .</p>	111
Figure 6.5	<p><b>SAME-ECOS and NNLS derived in-vivo myelin water fraction maps.</b> Six representative slices of the GRASE first echo, the resulting MWF maps produced by both methods (T<sub>2</sub>s &lt; 40ms), and the voxel-wise MWF difference map (SAME-ECOS MWF – NNLS MWF), are shown. . . . .</p>	112

Figure 6.6 **Voxel spectra (gray), the mean spectra (blue: SAME-ECOS; red: NNLS), and the mean MWF ( $T_2s < 40ms$ ) within the four ROIs of the experimental in-vivo data.** ROIs include the corpus callosum, corticospinal tract, forceps major, and forceps minor. The voxel spectra are only plotted for a fraction of the total number of voxels for a visual-friendly presentation as indicated in each subfigure. The mean spectrum and mean MWF are calculated from all voxels within each ROI. . . . . 113

Figure 7.1 **Motivation of random refocusing flip angle (FA).** The time evolution of transverse magnetization of two spins with similar  $T_2$  values driven by (a) the current and (b) proposed sequences are simulated using Bloch equations. Larger differences are observed with the proposed sequence. . . . . 126

# Acknowledgments

First and foremost, I would like to thank my parents for giving me unconditional love throughout my life and supporting me to choose the path I wanted. It is truly a privilege.

I would like to express my sincerest gratitude to my supervisors Cornelia Laule (Corree) and John Kramer (Kip), who provided tremendous support and guidance during these years. Corree, I have an endless list of things that I need to thank you for. In the simplest terms, thank you for giving me so many opportunities, showing me what attention to detail means, and pushing me to succeed. Your kindness and thoughtfulness make everyone around you happier. Kip, it has been a pleasure to work with you. You always give me generous support whenever I need it the most. I always find strength and motivation simply by chatting with you, thinking of your intriguing questions, and of course seeing your devotion to your family.

I would like to thank Qing-San Xiang, who is a committee member and also a mentor, for showing me a graceful approach to see the beauty of MRI, and encouraging me to explore the infinite possibilities of MRI. San, your unique taste in science has a great impact on me. Thank you for sharing with me your fascinating stories within and beyond the MRI world. It is always a pleasure to have a conversation with you anytime, anywhere.

I would also like to thank other committee members Roger Tam, David Li, and Piotr Kozlowski, for all the valuable suggestions and discussions, which undoubtedly made this work significantly better. Roger, thank you for guiding me in the field of deep learning whenever I have difficulties. David, thank you for providing your clinical expertise and always being sharp. Piotr, thank you for being so patient, approachable, and supportive along the way.

I would also like to thank Alex MacKay for pioneering the myelin water imaging technique, which is the isocenter of this thesis. Alex, thank you for your encouragement and support for my work. You are a perfect role model of being so knowledgeable, yet so humble.

I would also like to thank my colleagues and collaborators for their support: Catherine Jutzeler, Erin MacMillian, Shannon Kolind, Emil Ljungberg, Adam Dvorak, Sarah Morris, Lisa Lee, Jackie Yik, Andrew Yung, Laura Barlow, Irene Vavasour, Donna Lang, Anthony Traboulsee, Alex Rauscher, Cristina Rubino, and Lara Boyd. Especially, I would like to thank Susan Shinn and Farah Samadi from ICORD for making the lab such a warm place for me.

I would like to acknowledge the MS Society of Canada for providing me with the funding support, and the fantastic experience of three summer schools in Vancouver, St. John's, and Toronto.

As always, special thanks go to my life partner Jiali Liu for your company, understanding, support, encouragement, and love. You always take good care of me and our dear cat Lingling, who brings so much joy to our life. I am incredibly fortunate to have you by my side for this journey, and I cannot wait to start another adventure with you.

# Chapter 1

## Introduction

This chapter contains an overview of the background knowledge associated with the work in this thesis, including the principles of magnetic resonance imaging, an introduction to myelin water imaging, a discussion about the neural network algorithm, and finally an overview for this thesis work.

### 1.1 Magnetic resonance imaging

Magnetic resonance imaging (MRI) is a widely used medical imaging technique that utilizes the physical phenomenon of nuclear magnetic resonance (NMR) to create images. Immediately upon its discovery, MRI's advantages over other medical imaging modalities (e.g. X-ray) for better soft tissue contrast and the absence of ionizing radiation were clearly recognized. After several decades of research and development, MRI nowadays is capable of providing not only anatomical but also physiological, functional, and chemical information. In this thesis, relevant background knowledge of MRI is briefly introduced chronologically from a historical perspective.

#### 1.1.1 Nuclear magnetic resonance

In 1938, Isidor Issac Rabi sent a beam of LiCl molecules through a sufficiently strong magnetic field and observed that the molecule beam could absorb energy from a small oscillating magnetic field at certain frequencies. [180, 181] Rabi's

finding was an experimental proof of the NMR phenomenon, where the magnetic moment of a nucleus with non-zero spin precesses about an external magnetic field and can be perturbed by an oscillating magnetic field at specific frequencies. As its name 'NMR' indicates, the largest perturbation effect can take place when the oscillating field is resonating with the precession of nuclear magnetic moment. The precession frequency  $\omega_0$  is known as the Larmor frequency and defined in the following equation 1.1.

$$\omega_0 = \gamma B_0 \quad (1.1)$$

where  $\gamma$  is called the gyro-magnetic ratio only determined by the kind of nuclei and  $B_0$  is the external magnetic field strength. For example, hydrogen  $^1\text{H}$  has  $\gamma = 42.58$  MHz/Tesla, which corresponds to a Larmor frequency  $\omega_0 = 127.74$  MHz at 3.0 Tesla (T).

### 1.1.2 Bloch equation

In 1946, Felix Bloch's group [19] and Edward Purcell's group [179] independently extended the NMR experiment to liquid and solid by using induction and absorption methods, respectively. In both methods, the oscillating magnetic field was achieved by using a radio frequency (RF) coil with an alternating current. In the absorption method used by Purcell's group, a significant power loss in the RF coil was observed when the frequency of alternating current was equal to the Larmor frequency  $\omega_0$ . In the induction method used by Bloch's group, which later dominates modern NMR technologies, a second RF coil was placed orthogonal to the first RF coil to receive any signal emitted by the sample. An induction signal was only detected by the receiver RF coil when the frequency of the alternating current in the first RF coil reached Larmor frequency  $\omega_0$ .

Although NMR is a quantum phenomenon related to nuclear spin, it can readily be explained by classical mechanics more intuitively. When placing an ensemble of spins in an external magnetic field  $B$ , the spin ensemble exhibits a net magnetization  $M$ , which is the vector sum of the magnetic moment of all spins in the ensemble. The magnetization  $M$  aligns with and precesses about the direction of  $B$  at Larmor frequency  $\omega_0$  in equilibrium. Then, using an oscillating magnetic field (e.g. RF pulse) at Larmor frequency,  $M$  can be tipped away from its precess-

ing axis, projecting  $\mathbf{M}$  into the transverse plane and continuing to precess with a so-called flip angle  $\alpha$  (the angle between the tipped  $\mathbf{M}$  and  $\mathbf{B}$ ), the value of which can be obtained by

$$\alpha = \gamma B_1 \tau \quad (1.2)$$

where  $B_1$  is the magnitude of the oscillating magnetic field strength, and  $\tau$  is the duration of the applied RF pulse. The tipped magnetization  $\mathbf{M}$  will gradually return to the equilibrium position (aligning with  $\mathbf{B}$ ) due to the dephasing of the magnetic moments of spins in the ensemble caused by spin-spin and spin-lattice interactions. The recovery to the equilibrium position is characterized by two time constants known as the spin-lattice relaxation time  $T_1$  and the spin-spin relaxation time  $T_2$ , which correspond to the longitudinal and transverse directions, respectively. Schematics of the NMR phenomenon described by classical mechanics is depicted in Figure 1.1.

To put the classical understanding of NMR into a mathematical context, Bloch [18] formulated the following equation 1.3, known as the Bloch equation, to describe the time evolution of the magnetization vector  $\mathbf{M} = (M_x, M_y, M_z)$  with an equilibrium value of  $M_0$  in a magnetic field  $\mathbf{B}$ .

$$\frac{d\mathbf{M}}{dt} = \gamma \mathbf{M} \times \mathbf{B} - \frac{M_x \hat{x} + M_y \hat{y}}{T_2} - \frac{(M_z - M_0) \hat{z}}{T_1} \quad (1.3)$$

Assuming the magnetic field is along z direction,  $\mathbf{B} = B_0 \hat{z}$ , and  $M_x(0)$ ,  $M_y(0)$ ,  $M_z(0)$  are the initial values right after the magnetization  $\mathbf{M}$  is perturbed by an RF pulse, then the general solution to the Bloch equation can be expressed as:

$$M_x(t) = [M_x(0) \cos \omega_0 t + M_y(0) \sin \omega_0 t] \exp\left(-\frac{t}{T_2}\right) \quad (1.4)$$

$$M_y(t) = [-M_x(0) \sin \omega_0 t + M_y(0) \cos \omega_0 t] \exp\left(-\frac{t}{T_2}\right) \quad (1.5)$$

$$M_z(t) = M_0 + [M_z(0) - M_0] \exp\left(-\frac{t}{T_1}\right) \quad (1.6)$$

Subsequently, the time evolution of the transverse magnetization  $M_{xy}$  using a com-

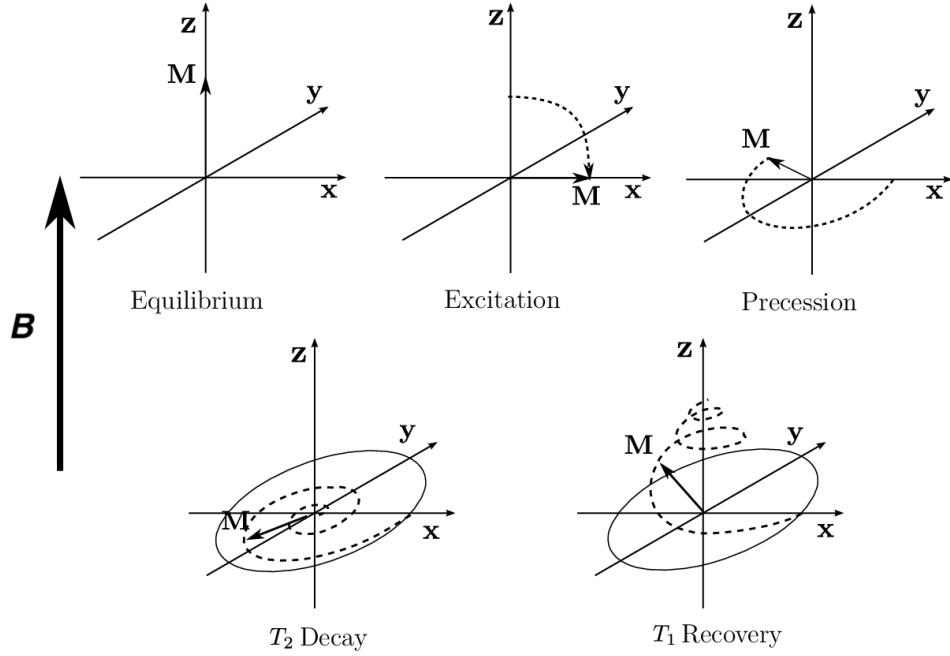


**Figure 1.1: Schematics of the NMR phenomenon.** At equilibrium, the magnetization  $M$  initially aligns with the direction of external magnetic field  $B$ . After being excited by a  $90^\circ$  RF pulse,  $M$  is tipped to the transverse plane, followed by  $T_2$  decay and  $T_1$  recovery immediately. This figure is attributed to Arijit Hazra. [78]

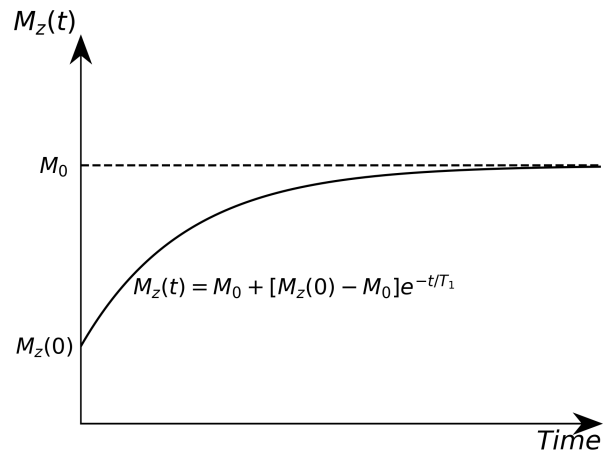
plex plane representation ( $M_{xy} = M_x - iM_y$ ) is :

$$M_{xy}(t) = M_{xy}(0)e^{-t/T_2}e^{i\omega_0 t} \quad (1.7)$$

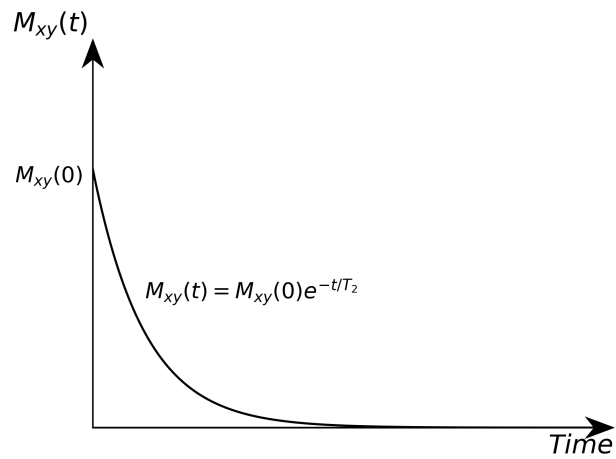
where  $M_{xy}(0) = \sqrt{M_x(0)^2 + M_y(0)^2}$  is the initial value of the transverse magnetization. If a reference frame rotating at  $\omega_0$  about the  $z$  axis is used, then the term  $e^{i\omega_0 t}$  in equation 1.7 can be demodulated out to give

$$M_{xy}(t) = M_{xy}(0)e^{-t/T_2} \quad (1.8)$$

which is simply an exponential decay function characterized by  $T_2$ . The time evolution of longitudinal magnetization  $M_z$  and transverse magnetization  $M_{xy}$  are illustrated in Figure 1.2.



(a) Longitudinal magnetization recovery



(b) Transverse magnetization relaxation

**Figure 1.2: Time evolution of longitudinal and transverse magnetization.**

(a) The rate of longitudinal recovery is governed by  $T_1$ . (b) The rate of transverse relaxation is governed by  $T_2$ .

The transverse magnetization generated by a single RF pulse induces a decay signal in the receiver RF coil, known as the free induction decay (FID). However, in reality, the relaxation of transverse magnetization is not only driven by the spin-spin relaxation time  $T_2$ . The magnetic field inhomogeneity can also cause the dephasing of the spins, making the signal loss much faster. The effect of field inhomogeneity is quantified using the parameter  $T_2'$ , and thus the decay rate of FID  $T_2^*$  is defined as a combination of  $T_2$  and  $T_2'$ :

$$\frac{1}{T_2^*} = \frac{1}{T_2} + \frac{1}{T_2'} \quad (1.9)$$

Unlike the random spin dephasing caused by spin-spin interactions ( $T_2$ ), the spin dephasing due to magnetic field inhomogeneity ( $T_2'$ ) is static and thus reversible by using a spin echo pulse sequence that is introduced in the next section.

### 1.1.3 Spin echo

In 1950, Erwin Hahn discovered that the signal loss due to field inhomogeneity could be recovered by applying two successive  $90^\circ$  RF pulses, and he coined the term 'spin echo' for the recovered signal. [74] Later in 1954, Herman Carr and Edward Purcell modified the spin-echo experiment by using a  $90^\circ - 180^\circ$  RF pulse pair (CP sequence). [28] For simplicity, only the modified spin-echo experiment is discussed here.

In a rotating frame of reference ( $x' - y' - z$  coordinate), the CP sequence begins with a  $90^\circ$  excitation pulse applied in the  $x'$  direction to flip the magnetization into  $y'$  direction. Then the spins dephasing starts in the transverse plane due to the  $T_2$  and  $T_2'$  effects. After time  $\tau$ , a  $180^\circ$  pulse is also applied in the  $x'$  direction to flip over all spins into their opposite directions, leading to a rephasing effect for the dephased spins. Waiting exactly for another time  $\tau$ , the rephasing spins are refocused in the  $-y'$  direction, and the transverse magnetization is recovered to generate a strong induction signal known as the spin echo. Moreover, the CP sequence can be extended to produce a train of spin echoes by applying the  $180^\circ$  refocusing pulses repeatedly at times of  $\tau$ ,  $3\tau$ ,  $5\tau$ ..., and consequently the spin echoes are formed at times of  $2\tau$ ,  $6\tau$ ,  $6\tau$ ... The above described spin-echo experiment using the CP pulse sequence is depicted in figure 1.3. However, only the  $T_2'$  dephasing effect

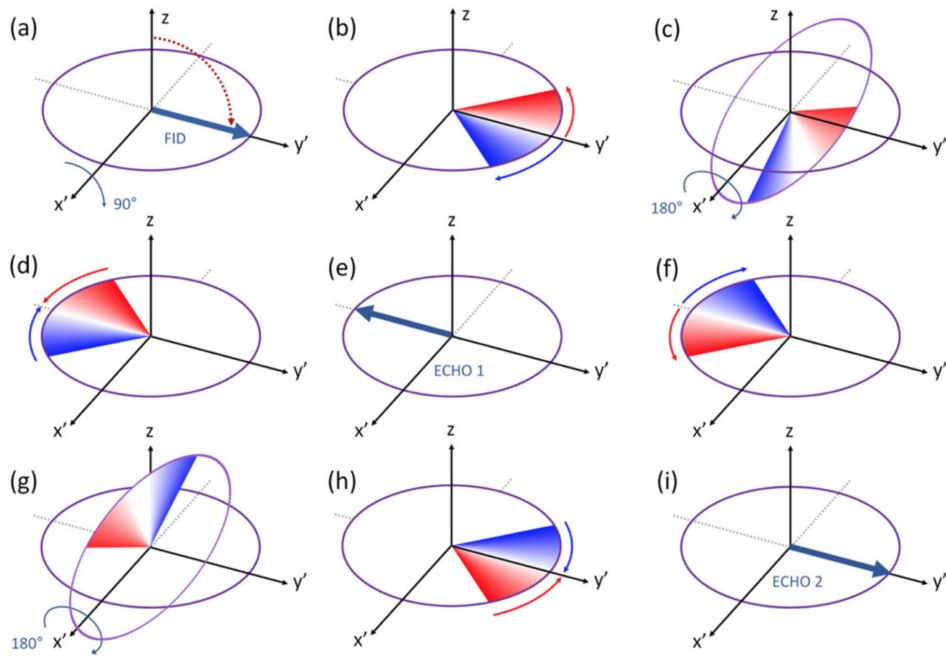


**Figure 1.3: Carr–Purcell sequence showing the first two echoes in the rotating frame.** (a) Excitation by a  $90^\circ$  RF pulse; (b) spin dephasing; (c) spin flipped by a  $180^\circ$  RF pulse; (d) spin rephasing; (e) spin refocused to form a spin echo; (f)–(i) formation of the second echo. This figure is attributed to Richard Ansorge. [7]

is reversible so that the recovery of transverse magnetization (spin echoes) is still modulated by the  $T_2$  relaxation.

In 1958, Saul Meiboom and David Gill [158] further modified the CP pulse sequence by applying the  $180^\circ$  refocusing pulses in the  $y'$  direction instead of the  $x'$  direction, resulting in a much higher tolerance of the flip angle error, which is commonly encountered due to system imperfections even for today's technology. This further modified spin-echo method is known as the CPMG (Carr-Purcell-Meiboom-Gill) sequence, which has been widely used in various MR spectroscopy and imaging techniques.

### 1.1.4 Spatial encoding and k-space

In the 1970s, Paul Lauterbur and Peter Mansfield pioneered the possibilities of using the magnetic field gradient to localize NMR signals to create an image that maps the distribution of magnetization [120, 152]. Apparently, spatial encoding bridges NMR to MRI, and hence they are recognized as the inventors of modern MRI. The initial method proposed by Lauterbur in 1973 was to reconstruct the object from one-dimensional projections at various orientations using a spatial gradient. In 1977, Mansfield took Lauterbur's initial work one step further by extending the use of spatial gradient from one dimension to all three dimensions to encode the spatial information, achieving the data acquisition in a drastically shorter time. The technique of spatial encoding via gradients was quickly adopted and significantly refined by others. A formalism called 'k-space' was subsequently proposed by Richard Likes in 1981 and Stig Ljunggren in 1983 to formulate the spatial encoding technique for practical use. [133, 142] In this section, the concepts of spatial encoding and k-space are introduced.

The spatial encoding of NMR signals is based on making the magnetic field non-uniform, which is realized by superposing the magnetic gradient field on top of the main field  $B_0$  in three orthogonal directions. The resulting non-uniform field in space takes the form of

$$\mathbf{B}(x, y, z) = \hat{z}(B_0 + xG_x + yG_y + zG_z) \quad (1.10)$$

where  $G_x$ ,  $G_y$ ,  $G_z$  are the strengths of the gradient field in the  $x$ ,  $y$ ,  $z$  directions. The non-uniform field is  $B_0$  at the isocenter and varies linearly with coordinates. During imaging,  $G_x$ ,  $G_y$ ,  $G_z$  are independently controlled by three sets of coils, switching on and off rapidly, to realize slice selection, frequency encoding, and phase encoding, details of which are described below.

According to equation 1.10, when a certain gradient field ( $G_x$ ,  $G_y$ ,  $G_z$ ) is applied, it can be inferred that a plane perpendicular to the applied gradient field will have the same field strength. Then, nuclear spins in that particular plane will have the same Larmor frequency

$$\omega = \gamma(B_0 + xG_x + yG_y + zG_z) \quad (1.11)$$

and spins outside that plane will precess at different Larmor frequencies other than  $\omega$ . Therefore, when the gradient is on, RF pulses with the frequency  $\omega$  can only excite spins within the selected plane where the Larmor frequency is exactly  $\omega$ . However, a realistic RF pulse always carries a certain frequency bandwidth  $\Delta\omega_{rf}$ , which makes the selected plane to have a thickness of

$$d = \frac{\Delta\omega_{rf}}{\gamma |\hat{x}G_x + \hat{y}G_y + \hat{z}G_z|} \quad (1.12)$$

Although the gradient is usually applied along the main field direction ( $\hat{z}$ ) for slice selection in most MRI applications, a slice can be selected at any orientation by a combination use of  $G_x$ ,  $G_y$ , and  $G_z$ . This property is one of the MRI's advantages compared with other imaging modalities. But for simplicity, slice selection along z direction is assumed hereafter.

Once a slice is excited, the receiver coil can detect the induction signal coming from all spins within the whole selected slice. If a gradient field is turned on during the signal detection period, for instance along the x direction for duration  $T_x$ , the Larmor frequency will vary linearly in the x direction:

$$\Delta\omega_x = x \frac{k_x}{T_x} \quad (1.13)$$

where  $\Delta\omega_x$  is the variation of Larmor frequency along the x direction and  $k_x$  is a known quantity defined as

$$k_x = \gamma G_x T_x \quad (1.14)$$

Then, the resulting signal will become a mixture of oscillations at different frequencies. Later, this mixed signal can be mathematically decomposed (via Fourier analysis) into a spectrum of frequency components, amplitudes of which indicate how many spins are precessing at each frequency. Since the frequency and the position are linearly correlated due to the application of frequency encoding gradient, contributions to the signal can thus be spatially resolved along the x direction.

In between slice selection and frequency encoding, phase encoding is usually applied to discriminate signals along the y direction. For example, if a gradient is turned on for phase encoding along the y direction for duration  $T_y$ , then spins along

y axis will precess at different Larmor frequencies during  $T_y$  and acquire additional phases after  $T_y$  as a function of their positions in the y axis:

$$\Delta\phi_y = yk_y \quad (1.15)$$

where  $k_y$  is a known quantity defined as

$$k_y = \gamma G_y T_y \quad (1.16)$$

When the gradient field is turned off after  $T_y$ , all spins along the y direction will precess at the same Larmor frequency again, but the phase shift  $\Delta\phi_y$  of each spin will persist and have an impact on the recorded signal after frequency encoding. Now, one cycle of slice selection, phase encoding, frequency encoding, and signal recording is completed.

However, to recover the full image, this cycle needs to be repeated for a number of times with a different phase encoding at each time to acquire a signal with a different phase shift. After all cycles, the phase encoding steps are repeated for a range of  $k_y$  values by varying the  $G_y$  or  $T_y$  to linearly increase the  $\Delta\phi_y$  of each spin from negative maximum to positive maximum. For each spin along the y direction, the phase shift  $\Delta\phi_y$  changes between cycles since the  $k_y$  changes at every cycle. It can be derived from equation 1.15 that the rate of the phase shift change  $f_{\phi,y}$  between cycles, which is the partial derivative of the phase shift  $\Delta\phi_y$  with respect to the  $k_y$ , only depends on its position in the y axis:

$$f_{\phi,y} = \frac{\partial\Delta\phi_y}{\partial k_y} = y \quad (1.17)$$

Consequently, the rate  $f_{\phi,y}$  equals to zero at the isocenter and gets higher as moving away from the isocenter. Using one element from a column object as an example illustrated in Figure 1.4, the rate of phase shift  $f_{\phi,y}$  of this element is exactly the frequency of a composite oscillation, amplitudes of which are measured on the induction signals of this element at the same time for every cycle and plotted along the  $k_y$  axis. Then, the total composite signal from all elements will be a mixture of oscillations at different frequencies. The value of each frequency indicates its

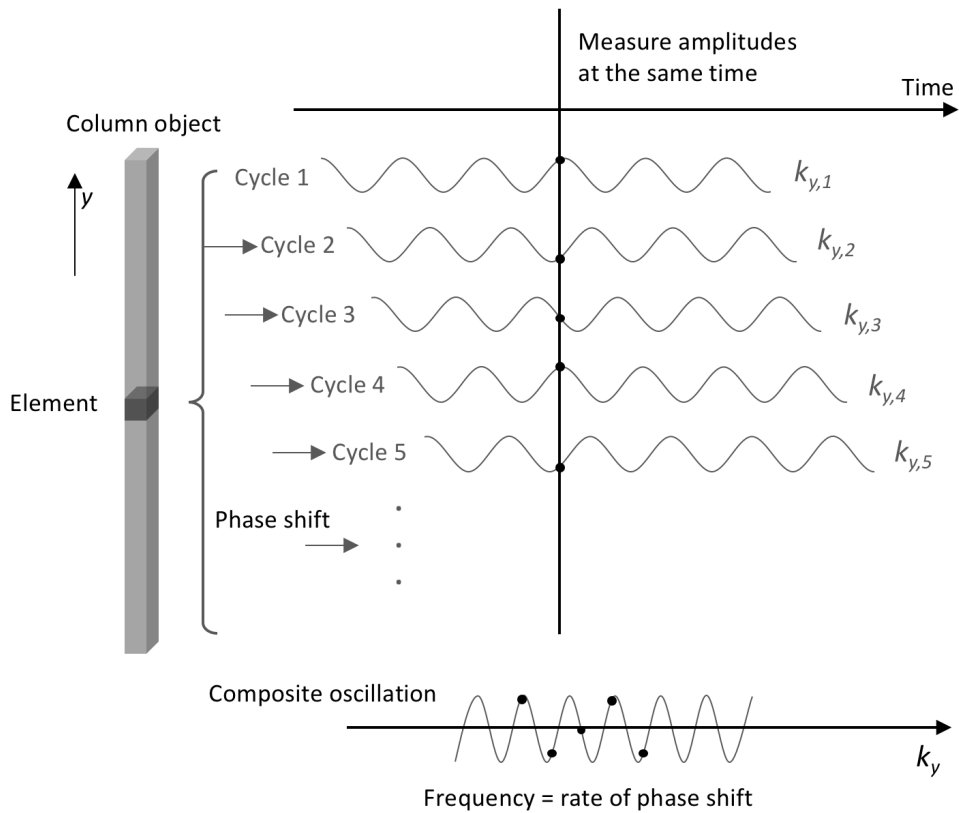


**Figure 1.4: Illustration of phase encoding.** The induction signal of the element is phase shifted at each cycle after a different phase encoding ( $k_{y,1}$ ,  $k_{y,2}$ ,  $k_{y,3}$ ...). If the amplitude of the induction signal is recorded at the same time for every cycle and plotted in the  $k_y$  axis, then the composite oscillation will have a frequency that is equal to the rate of phase shift  $f_{\phi,y}$ .

position along the  $y$  axis. Again, Fourier analysis can be applied to decompose the total composite signal into individual frequency components so that the elements along the  $y$  direction can be resolved spatially due to the linear mapping between the frequency and the position.

In the rotating frame of reference, any magnetization located in the selected transverse plane, denoted as  $M(x,y)$ , is modulated by frequency encoding and phase encoding to give a signal  $S(x,y)$ , which can be derived from equations 1.13

and 1.15 to give the form of

$$S(x, y) = M(x, y)e^{i[\Delta\omega_x t + \Delta\phi_y]} \quad (1.18)$$

$$= M(x, y)e^{ixk_x}e^{iyk_y} \quad (1.19)$$

When the receiver coil records a signal in the time domain, all magnetization elements from the selected slice are emitting their signals simultaneously. Due to the position information being encoded and thus obscured, the signal's amplitude at any time point cannot directly be stored in a  $(x, y)$  coordinate. To deal with this issue of raw data storage, a new coordinate is constructed with  $k_x$  and  $k_y$  being the orthogonal axis. Because the signal at any time point can be uniquely identified by a pair of  $k_x$  and  $k_y$  values, making the  $(k_x, k_y)$  coordinate system, known as the k-space, a natural choice for the raw data storage. In k-space, the recorded signal is denoted as  $S(k_x, k_y)$ , which relates to the  $S(x, y)$  and  $M(x, y)$  in the form of

$$S(k_x, k_y) = \iint S(x, y) dx dy \quad (1.20)$$

$$= \iint M(x, y) e^{ixk_x} e^{iyk_y} dx dy \quad (1.21)$$

Clearly,  $S(k_x, k_y)$  and  $M(x, y)$  compose a pair of 2-dimensional (2D) Fourier transform. After enough spatial encoding cycles, the k-space is filled with  $S(k_x, k_y)$  for all possible  $k_x$  and  $k_y$  values. Then, the magnetization distribution  $M(x, y)$ , which is essentially an image, can be recovered by a 2D Fourier transformation with respect to the  $k_x$  and  $k_y$  directions and takes the form of

$$M(x, y) = \frac{1}{4\pi^2} \iint S(k_x, k_y) e^{-ixk_x} e^{-iyk_y} dk_x dk_y \quad (1.22)$$

Finally, an MRI image is carried out from NMR signals through steps of slice selection, phase encoding, frequency encoding, k-space filling, and Fourier transformation. To put all together, a spin-echo (SE) MRI sequence that represents the timing of these steps and its corresponding k-space filling trajectory are presented in Figure 1.5. By the definitions of  $k_x$  and  $k_y$  (equations 1.14 and 1.16), navigation in k-space is achieved by varying the gradient strength and duration. Then, a desired data filling trajectory can be planned accordingly in an MRI sequence. As

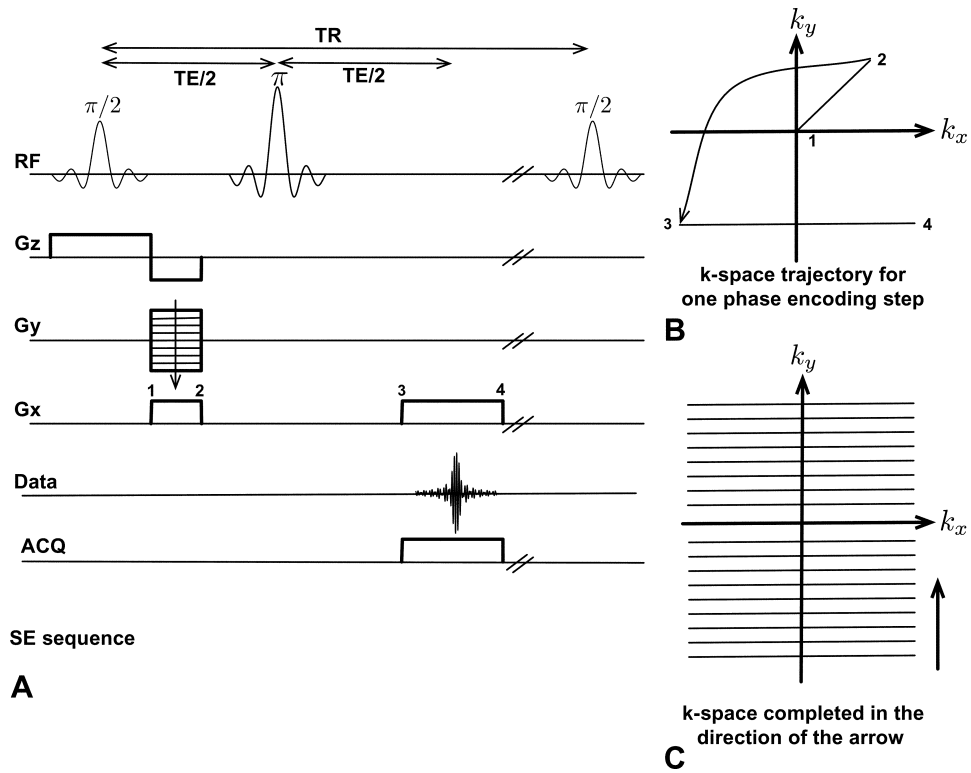


**Figure 1.5: Spin-echo (SE) MRI sequence (A) and k-space (B) & (C).** The  $90^\circ$  RF pulse is applied with gradient  $G_z$  on to select a slice. Initially, the k-space filling takes the trajectory from 1→2 due to the gradients  $G_y$  and  $G_x$  (from 1 to 2 in (A)); 2→3 due to the  $180^\circ$  pulse (the curved line is only for visualization); 3→4 due to the gradient  $G_x$  (from 3 to 4 in (A)) while recording the data at the same time. The cycle is repeated with a different  $G_y$  at each time. TE: echo time; TR, repetition time; ACQ: analog-to-digital converter. This figure is attributed to Kiruluta. [99]

illustrated in Figure 1.5, the SE sequence takes the trajectory of  $1 \rightarrow 2 \rightarrow 3 \rightarrow 4$ , with  $1 \rightarrow 2$  due to the positive gradients  $G_y$  and  $G_x$  (from point 1 to point 2 in sub-figure (A));  $2 \rightarrow 3$  due to the  $180^\circ$  RF pulse;  $3 \rightarrow 4$  due to the positive gradient  $G_x$  (from point 3 to point 4 in sub-figure (A)) while reading out the data at the same time. The negative lobe of  $G_z$  and positive the lobe of  $G_x$  before the  $180^\circ$  RF pulse are applied to compensate the phase dispersion caused by slice selection and frequency encoding, since they are not designed for phase encoding, and the phase dispersion is just a side effect. Consequently, the strongest signal appears at echo time (TE) when the spins are refocused, and the phase dispersion is fully compensated. The cycle is repeated with a different  $G_y$  at each time until k-space is fully sampled, and the time interval between cycles is defined as the repetition time (TR).

For most medical MRI applications, free and loosely bound water protons  $^1\text{H}$  are of primary interest because of their natural abundance in the human body and their convenient  $T_1$  and  $T_2$  relaxation times (not too short) for measurement. The contrast of an MRI image mainly comes from the distinctive  $T_1$  and  $T_2$  values of the water protons as well as the proton density (PD) in different tissue types. An MRI sequence can be designed by varying the flip angle of the RF pulse, and the timing of TE and TR to reveal the differences in  $T_1$ ,  $T_2$ , or PD among tissues. Therefore, the MRI image contrast is typically referred to as  $T_1$ -weighting,  $T_2$ -weighting, or PD-weighting, depending on the specific sequence used. Examples of MRI contrast are presented in Figure 1.6. In modern years, more sophisticated MRI sequences and analysis methods are developed to provide information even at the molecular level, such as the myelin water imaging, details of which are introduced in the next section.

## 1.2 Myelin water imaging

In this section of introduction to myelin water imaging (MWI), the background of myelin and myelin water imaging is introduced first, followed by the MWI data acquisition and the MWI data analysis.

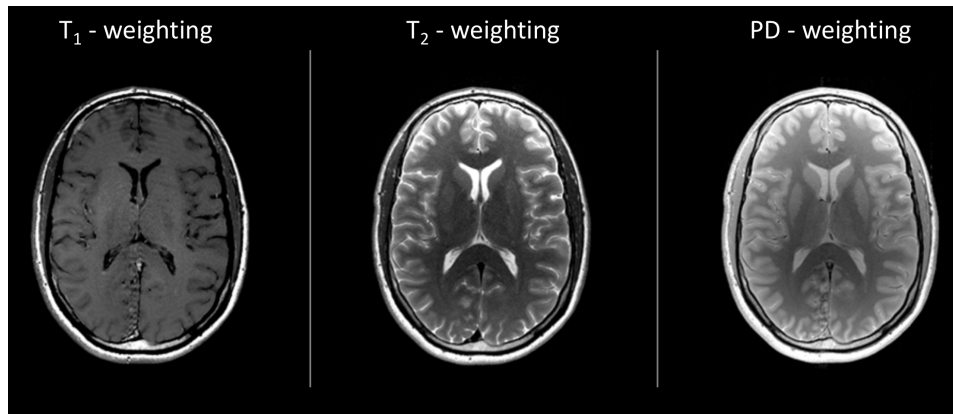


**Figure 1.6: Examples of MRI image contrast.** Brain images with contrasts of  $T_1$ -weighting,  $T_2$ -weighting, and PD-weighting are presented in axial view. This Figure is attributed to Tamir. [208]

### 1.2.1 Background of myelin

The central nervous system (CNS) contains approximately 86 billion neurons [80] that facilitate the transmission and processing of information in terms of electrical signals. A typical neuron is made up of four parts: (1) the cell body (soma), which contains the nucleus; (2) the axon, which transmits electrical signals between neurons; (3) the dendrites, which receive signals from other neurons; and (4) the axon terminals, which release neurotransmitters to relay the signal to the next neuron's dendrites. The structure of a typical neuron is depicted in Figure 1.7.

The CNS tissues, including the brain and spinal cord, can be divided into grey and white matter due to the distinctive colouring (Figure 1.8). The cell bodies and dendrites of the neurons are mostly grouped together to primarily make up the grey matter, while the axons are tightly bundled together to compose the white matter. The white colouring of white matter is attributed to the presence of myelin (Figure 1.7), a fatty sheath that forms around most axons in the white matter. [29]

Myelin consists of approximately 30% proteins and 70% lipids produced by the oligodendrocyte cells. [183] Gaps that exist in myelin sheath along an axon are called nodes of Ranvier, and the myelin sheath between nodes of Ranvier are called internodes (Figure 1.7). The myelin sheath wraps around the axons in a concentric lamellar fashion. The cross-sectional view of a myelinated axon is shown in Figure

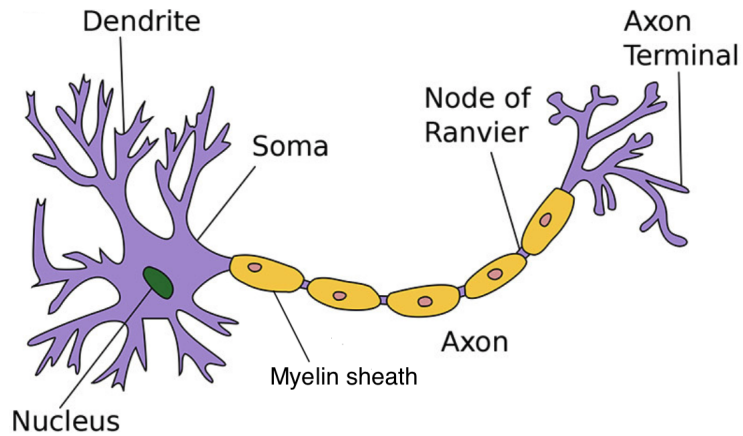


**Figure 1.7: Neuron anatomy.** The figure is attributed to Quasar Jarosz at English Wikipedia. [36] The length of an axon ranges from millimeters to meters.

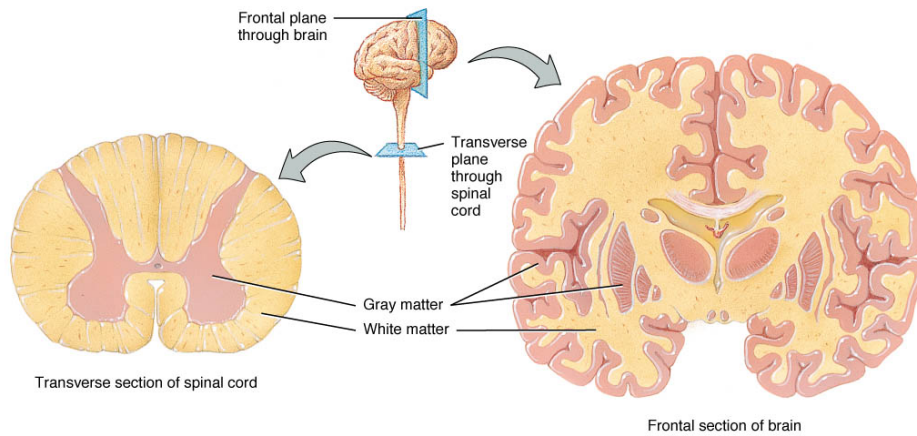


**Figure 1.8: Grey and white matter.** This figure is attributed to Mandira P. at Socratic Q&A. [150]

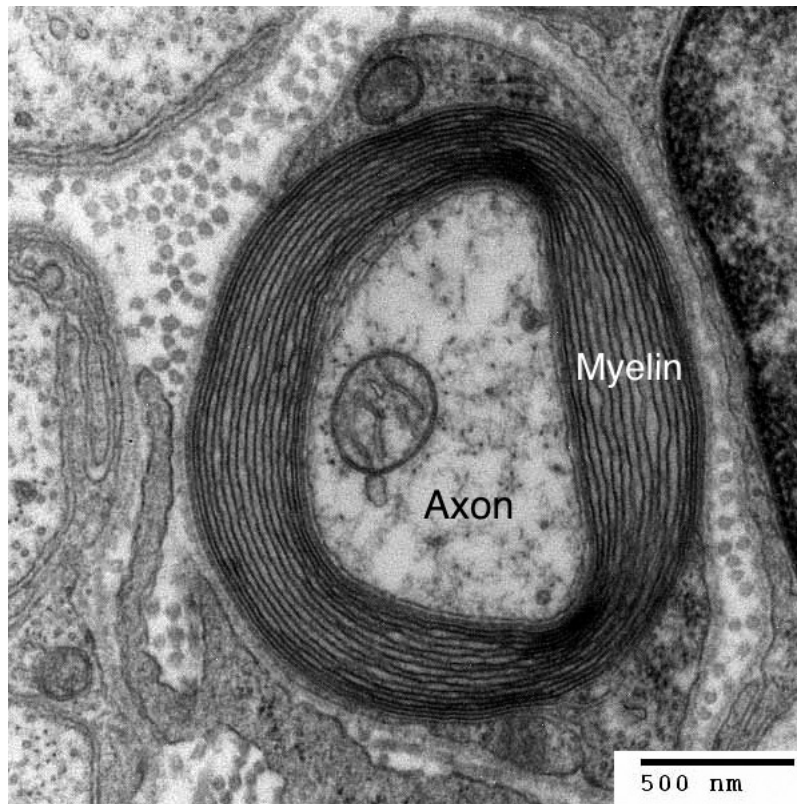


**Figure 1.9: Transmission electron micrograph of a myelinated axon.** This figure is attributed to Electron Microscopy Facility at Trinity College, Hartford, Connecticut. [188]

1.9 produced by transmission electron micrograph.

The primary function of myelin is to allow electrical impulses to transmit quickly and efficiently along the axons. In the CNS, the speed of impulse transmission along a myelinated axon can be increased by 10 to 100 times compared to that along an unmyelinated axon. [183] Myelin is of critical importance as high speed of conduction is essential in allowing complex motor, sensory, and behaviour of neuronal functions to occur. Besides, myelin acts as an axon insulator that prevents charge leakage due to its high electrical resistance and low capacitance. Also, myelin has been reported to play an important role in regulating axonal transport [57], maintaining axonal integrity [17, 22, 56, 97], altering pH [22], and regulating

fluid volume and ion composition. [55]

Disorders in the myelin sheath can be classified into two categories, demyelination and dysmyelination. [68] Demyelination is the condition in which pre-existing myelin sheaths are damaged and subsequently lost. It is one of the leading causes of neurological diseases such as multiple sclerosis, acute disseminated encephalomyelitis, transverse myelitis, chronic inflammatory demyelinating polyneuropathy, and central pontine myelinosis. [68] Dysmyelination refers to the malformed and defective myelin sheath. As opposed to the destruction of pre-existing healthy myelin that is seen in demyelination, dysmyelination is the defective formation of myelin during development, mainly due to genetic mutations. Dysmyelination disorders include leukodystrophies, phenylketonuria, and schizophrenia. [68]

### **1.2.2 Background of myelin water imaging**

Using MRI to examine myelin disorders has attracted much attention in recent years. Usually, information about myelin damage is not directly reflected in the MRI images because conventional MRI does not have the specificity. However, such information can be queried indirectly by thoroughly analyzing the  $T_2$  relaxation of the water molecules in the tissue that contains myelin.

As has been shown in Figure 1.9, the bilayer structure of the laminated myelin sheath (dense lines) can be obviously seen. Between the myelin bilayers, a pool of water, known as the myelin water (MW), is trapped. Since the MW is tightly bounded within the myelin bilayers, it experiences a faster decay rate that leads to a shorter  $T_2$  compared with other less restricted water pools such as the intra- and extra-cellular water (IEW) and the free water. Typically, a multi-echo spin-echo experiment is performed to characterize the  $T_2$  decay curve, from which the  $T_2$  relaxation time can be easily calculated according to equation 1.7, if there is only a single pool of water. However, the signals originated from MW, IEW, and free water are superimposed, making the obtained decay curve, in fact, a sum of multiple exponentials. The decomposition of such a multi-exponential decay curve is a nontrivial problem to solve, especially when the data is noisy such as the MR data.

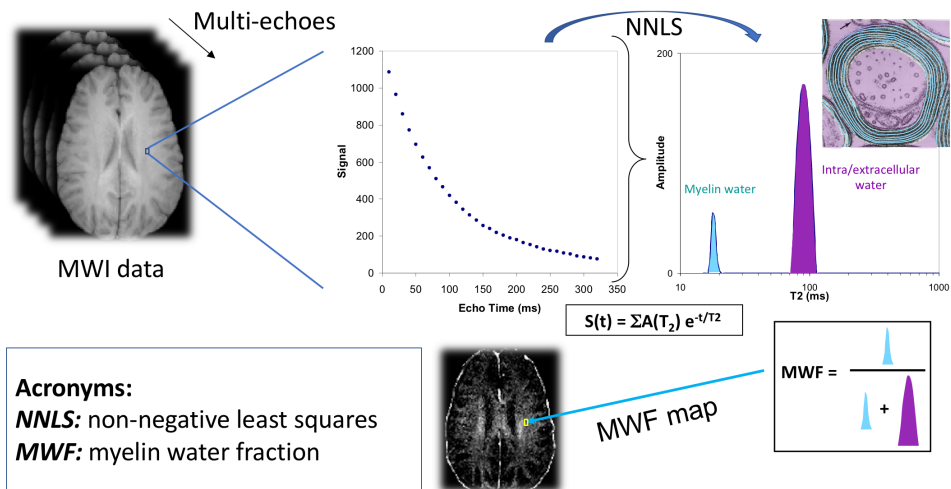


**Figure 1.10: The concept of myelin water imaging (MWI).** The  $T_2$  decay curve is analyzed by non-negative least squares (NNLS) to obtain the  $T_2$  distribution, from which the myelin water fraction (MWF) is calculated.

In the early 1990s, Ken Whittall and Alex MacKay [146, 224] proposed to use non-negative least squares (NNLS), which was a numerical fitting method, to decompose the decay curve into a distribution of  $T_2$  times. In the resulting distribution, the short  $T_2$  components (usually  $T_2 < 40$  ms) was attributed to the MW. Then, myelin water fraction (MWF), defined as the ratio of MW components to the total distribution, was calculated to indicate the myelin abundance in the tissue since myelin and MW always make their appearance together. The described method developed by Whittall and MacKay is so-called myelin water imaging (MWI). A schematic diagram is shown in Figure 1.10 to illustrate the general concept of MWI. The specificity of MWF as a surrogate biomarker for myelin has been histologically validated by different groups. [111, 112, 205]

### 1.2.3 Data acquisition

A commonly used pulse sequence for MWI is the multi-echo spin-echo (MSE) sequence (Figure 1.11), which is developed based on the famous CPMG that has been introduced earlier. [146, 175] In the MSE experiment, the single  $180_y^\circ$  refocusing

pulse in the conventional CPMG is replaced with a composite of three pulses:  $90^\circ_x$ ,  $180^\circ_y$ , and  $90^\circ_x$ , to minimize the accumulations of dephasing error generated by a series of imperfect RF pulses. Besides, due to the refocusing pulse imperfections, some of the magnetization is left in the longitudinal direction and can be flipped into the transverse plane by later imperfect pulses, generating the stimulated echo that corrupts the  $T_2$  decay measurement. The detrimental influence of stimulated echoes can be effectively reduced by applying the refocusing pulses bracketed with balanced slice selective gradients known as the crushers. For magnetization that remains in the transverse plane, the effects of the crusher before and after the refocusing pulse cancel each other because of the  $180^\circ$  refocusing pulse. On the other hand, the stimulated echo does not remain in the transverse plane either before or after the refocusing pulse so that it will be dephased by the crusher gradients. It has been shown that a sequence with alternating polarity and varying amplitude of the crushers is the most effective for the stimulated echo reduction [175].

Although a single slice MSE is still considered as the gold standard for MWI, it suffers from long acquisition time. Because a sequence with multiple echoes requires multiple k-spaces to be fully sampled, but only one line is filled in each of the k-spaces per excitation. To deal with the issue, a gradient and spin echo (GRASE) sequence (Figure 1.12) can be utilized for MWI. [174] Similarly, GRASE also uses a  $90^\circ$  excitation pulse followed by a number of  $180^\circ$  refocusing pulses to produce a train of spin echoes. In contrast to MSE, each spin echo of GRASE is now sandwiched with two gradient echoes that are produced by the frequency encoding gradients with alternating polarity and varying amplitude during readout. As a result, three k-space lines can be acquired simultaneously per excitation, achieving an acceleration factor of 3. The k-space sampling strategy of GRASE is to use the spin echoes ( $T_2$  weighting) to fill the central region of k-space, and the gradient echoes ( $T_2^*$  weighting) to fill the periphery of k-space, such that an overall of  $T_2$  weighting is maintained.

Recently, a 3D version of GRASE was introduced by Prasloski et al. [177] to further improve MWI's utility. In the 3D GRASE sequence, slab selective  $90^\circ$  excitation and  $180^\circ$  refocusing pulses are used, and a second phase encoding along the slice selection direction is applied for each refocusing pulse, to allow data acquisition in the 3D k-space. As a result, 3D GRASE realizes a whole cerebrum

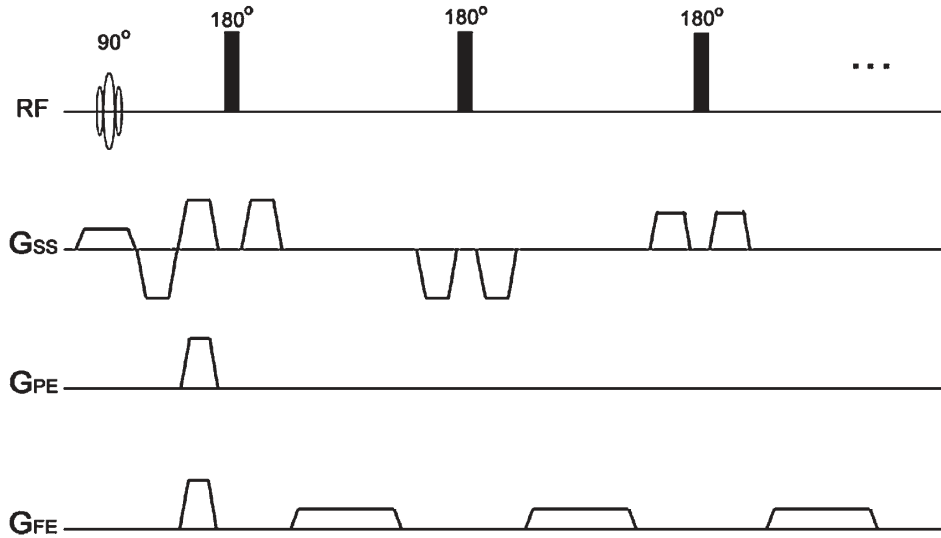


**Figure 1.11: Multi-echo spin echo (MSE) sequence.** A slice selective  $90^\circ$  excitation pulse is followed by a series of non-selective  $180^\circ$  refocusing pulses. Crushers with alternating polarity and varying amplitude are applied before and after the refocusing pulse.  $G_{SS}$ : slice selection gradient;  $G_{PE}$ : phase encoding gradient;  $G_{FE}$ : frequency encoding gradient. This figure is attributed to Alonso-Ortiz. [6]

MWI within 15 minutes at 3T. [177] Due to its high feasibility for in-vivo imaging studies, the 3D GRASE is used as the main MWI sequence in this thesis.

#### 1.2.4 Data analysis

The MWI data analysis is to decompose the multi-exponential  $T_2$  decay curve into its constituent  $T_2$  components. The backbone of the data analysis method used in this thesis is the non-negative least squares (NNLS) fitting algorithm, which is similar to the well-known least squares method but with a constraint of non-negative components. [121] The advantage of using NNLS for the MWI data analysis is that it does not require any initial assumptions about the number of  $T_2$  components and the convergence is always guaranteed for the solution.

Noise contamination is unavoidable, so a plain NNLS algorithm is often performed with a certain strength of regularization to improve its stability with regards

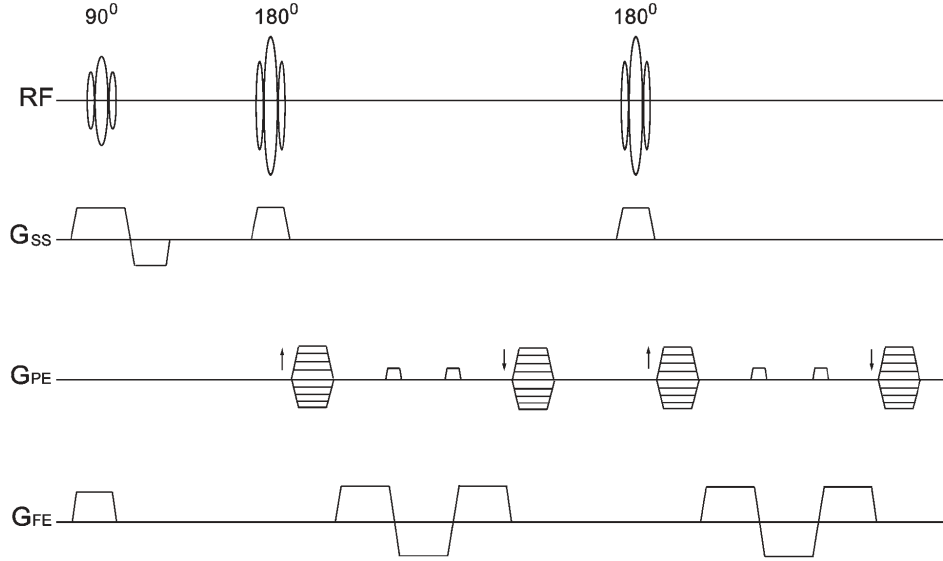


**Figure 1.12: Gradient and spin echo (GRASE) sequence.** A selective  $90^\circ$  is followed by a series of selective  $180^\circ$  refocusing pulses. Each spin echo is sandwiched by two gradient echoes.  $G_{SS}$ : slice selection gradient;  $G_{PE}$ : phase encoding gradient;  $G_{FE}$ : frequency encoding gradient. This figure is attributed to Alonso-Ortiz. [6]

to the noise level. [224] However, the MWI data in this thesis were collected by the 3D GRASE sequence at a field strength of 3T, where the stimulated echo generated by the refocusing FA error becomes another non-negligible source of data contamination and cannot be directly accounted for by the regularized NNLS. To deal with this problem, Prasloski et al. [176] integrated the regularized NNLS with the extended phase graph (EPG) algorithm [79] to correct the effect of stimulated echo by estimating the true FA. This approach significantly improves the accuracy of the  $T_2$  fitting result [176]. Thus it is adopted for the MWI data analysis in this thesis, and the default analysis steps are illustrated below.

1. For each imaging voxel, the decay data are extracted from each echo, with the  $i^{th}$  echo in the echo train denoted by  $y_i$  and the echo train length (ETL) denoted by  $M$ .
2. A number of  $N = 40$  basis  $T_2$  times logarithmically spaced between  $T_2^{min} =$

15 ms and  $T_2^{max} = 2000$  ms are generated with  $t_j$  indicating the  $j^{th}$  basis  $T_2$  time. The rationale of using logarithmic scale was that, the myelin water peak and the IE water peak are very close and the free water peak is too far away in a linear scale. And a number of  $N_\alpha = 8$  refocusing flip angles ( $\alpha$ ) are generated between  $FA_{min} = 50^\circ$  to  $FA_{max} = 180^\circ$  with equal spacing. The default values of these variables can be adjusted according to the needs of the analysis.

3. For each generated  $\alpha$  and  $t_j$ , the EPG algorithm is called to yield a set of synthetic decay data containing  $M$  data points:  $(a_1^{\alpha,t_j}, a_2^{\alpha,t_j}, \dots, a_M^{\alpha,t_j})$ . A default of  $T_1 = 1000$  ms is assumed.
4. For each  $\alpha$ , a kernel matrix  $A_{ij}^\alpha$  is constructed from the EPG-synthesized data and takes the form of

$$A_{ij}^\alpha = \begin{pmatrix} a_1^{\alpha,t_1} & a_1^{\alpha,t_2} & \dots & a_1^{\alpha,t_N} \\ a_2^{\alpha,t_1} & a_2^{\alpha,t_2} & \dots & a_2^{\alpha,t_N} \\ \vdots & \vdots & \ddots & \vdots \\ a_M^{\alpha,t_1} & a_M^{\alpha,t_2} & \dots & a_M^{\alpha,t_N} \end{pmatrix} \quad (1.23)$$

And the least squares misfit  $\chi_\alpha^2$  is expressed as

$$\chi_\alpha^2 = \sum_{i=1}^N \left| \sum_{j=1}^M A_{ij}^\alpha s_j - y_i \right|^2 \quad (1.24)$$

where  $s_j$  is the amplitude of the  $j^{th}$  basis  $T_2$  component. By minimizing the misfit,  $s_j$  is solved using the NNLS algorithm, and the minimum  $\chi_\alpha^2$  is subsequently calculated. This step is repeated for all  $\alpha$  to carry out their corresponding  $\chi_\alpha^2$ .

5. Spline interpolation of all  $\chi_\alpha^2$  is performed to obtain the optimal  $\alpha_{opt}$ , which gives the minimum  $\chi_\alpha^2$  in the interpolation curve. The resulting  $\alpha_{opt}$  is considered as the true refocusing FA.
6. New sets of synthetic decay data are yielded by EPG algorithm with the obtained  $\alpha_{opt}$  and a new kernel matrix  $A_{ij}^{\alpha_{opt}}$  is subsequently constructed. With

an additional term for the Tikhonov regularization [210], the least squares misfit becomes

$$\chi_{\alpha_{opt}}^2 = \sum_{i=1}^N \left| \sum_{j=1}^M A_{ij}^{\alpha_{opt}} s_j - y_i \right|^2 + \mu \sum_{i=1}^N |s_j|^2 \quad (1.25)$$

where  $\mu$  is the regularization parameter. Empirically,  $\mu$  is the largest value that allows the  $\chi_{\alpha_{opt}}^2 < 1.02\chi_{\alpha_{opt},min}^2$ , where  $\chi_{\alpha_{opt},min}^2$  is the minimum misfit for a non-regularized solution. By minimizing the misfit equation 1.25 with respect to the empirical regularization criterion,  $s_j$  is solved using the NNLS algorithm.

7. Finally, the amplitudes  $(s_1, s_2, \dots, s_M)$  of the basis  $T_2$  times depict a  $T_2$  distribution between  $T_2^{min}$  and  $T_2^{max}$  for this voxel. Useful metrics can be extracted from this distribution such as the myelin water fraction (MWF)

$$MWF = \frac{\sum s_{mw}}{\sum_{j=1}^M s_j} \quad (1.26)$$

where  $\sum s_{mw}$  is the sum of amplitudes in the predefined myelin water compartment, as shown in Figure 1.10.

This analysis pipeline is realized using MATLAB and the code can be requested at <https://mriresearch.med.ubc.ca/news-projects/myelin-water-fraction/>. It usually takes approximately two hours using a modern workstation computer for the analysis of a single brain.

### 1.2.5 MWI limitations

There are a few major limitations regarding the available in-vivo MWI technique. First of all, to achieve a reasonable scanning time, the TR (usually 1s) used in a MWI sequence is usually not long enough to completely eliminate the  $T_1$  effect, especially for those water compartments with long  $T_1$  times such as the CSF. Secondly, the current analysis model does not include a variable to account for the water exchange between the myelin water and the IE water compartments, which is a known effect leading to MWF underestimation. Thirdly, the NNLS analysis is

extremely susceptible to noise, even with a strong regularization and the resulting MWF map is still visually non-smooth. In particular, the user-defined initialization parameters (e.g.  $T_2$  range) may have an influence on the NNLS solutions. [223, 228] In addition, the MR signal with noise follows a Rician distribution but the implemented NNLS method is only capable to model Gaussian noise (details can be found in Chapter 6). Therefore, overfitting to noise is also a concern when using NNLS.

### 1.3 Neural networks

In more recent years, there is a rapidly increasing interest in utilizing machine learning and deep learning methods for tasks of high complexity because of their superior performance. An algorithm called neural networks (NN) [194], which is a supervised machine learning method, is used in the last two chapters of this thesis, for the development of faster and more accurate MWI data analysis. Hence the NN background is introduced in this section.

#### 1.3.1 Feedforward neural network architecture

The basic building blocks of NN are called nodes or neurons. A node takes inputs, performs some calculations with them, and produces one output (Figure 1.13). Specifically, the inputs  $(x_1, x_2, \dots, x_n)$  are multiplied by their corresponding weighting factors  $(w_1, w_2, \dots, w_n)$ , and added by a constant bias  $b$  to obtain a value  $z$ :

$$z = b + \sum_{i=1}^n x_i w_i \quad (1.27)$$

Then,  $z$  is passed to a certain activation function  $f$  to yield an activation output  $a$  written as

$$a = f(z) \quad (1.28)$$

$f$  is chosen from a wide range of nonlinear functions that introduce non-linearity to the system. Common choices of  $f$  are sigmoid function

$$\sigma(z) = \frac{1}{1 + e^{-z}} \quad (1.29)$$

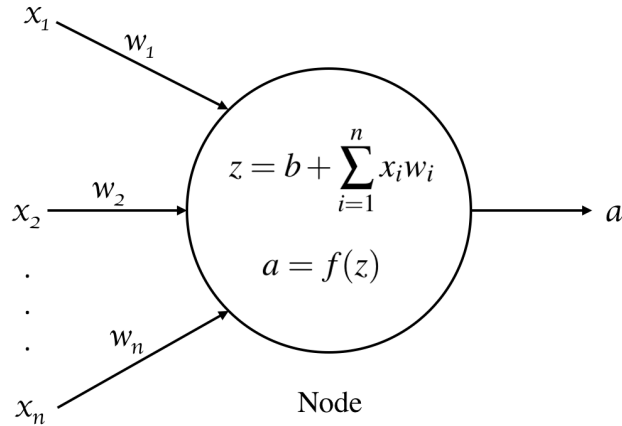


**Figure 1.13: Anatomy of a neural network node.** A node takes inputs  $(x_1, x_2, \dots, x_n)$ , performs some calculations with them, and produces one output  $a$ .

and tanh function

$$\tanh(z) = \frac{e^z - e^{-z}}{e^z + e^{-z}} \quad (1.30)$$

and rectified linear unit (ReLU)

$$\text{ReLU}(z) = \begin{cases} 0 & \text{for } z < 0 \\ z & \text{for } z \geq 0 \end{cases} \quad (1.31)$$

and so on. Two nodes can be connected by feeding the output of one node into the input of another node. A node can receive inputs from and send its processed result to multiple nodes so that a network can be formed.

A typical NN (Figure 1.14) has an architecture consisted of an input layer to take the input data, a number of so-called hidden layers to perform calculations, and an output layer to produce the calculated results. The specific NN architecture (e.g. numbers of nodes and layers) is usually selected according to the complexity of the task. A more complex task would require a deeper NN of more hidden layers. In a typical NN, nodes from adjacent layers are connected with each other, and the strength of each connection is determined by the associated weighting factors  $w$  and the bias  $b$  of each node. The input data propagate through the NN in a way that they are processed by every node in one layer, and then passed to the next layer,

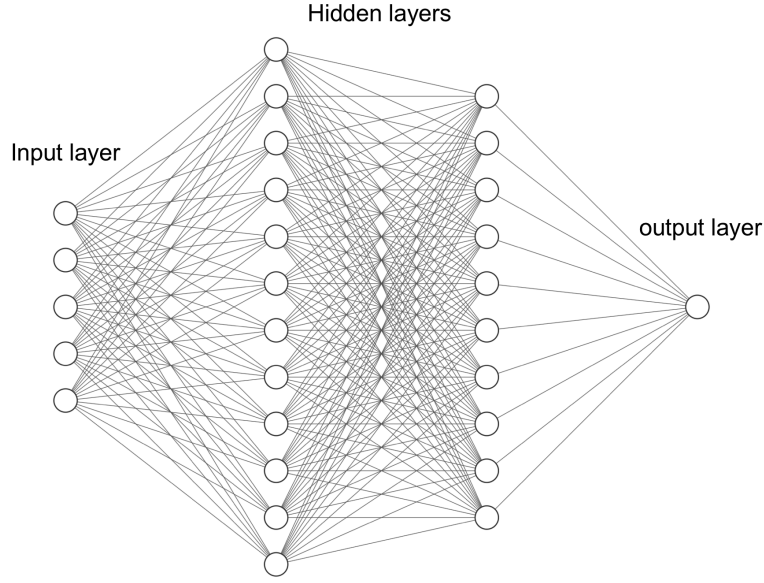


**Figure 1.14: A typical neural network architecture.** A NN consists of an input layer to take the input data, a number of hidden layers to perform calculations, and an output layer to yield the result.

and finally reach the output layer to yield a result. In a mathematical context, a forward propagation from the  $(l - 1)^{th}$  layer of  $m$  nodes to the  $l^{th}$  layer of  $n$  nodes can be expressed by the following:

$$\begin{bmatrix} z_0^{(l)} \\ z_1^{(l)} \\ \vdots \\ z_n^{(l)} \end{bmatrix} = \begin{bmatrix} w_{0,0}^{(l)} & w_{0,1}^{(l)} & \dots & w_{0,n}^{(l)} \\ w_{1,0}^{(l)} & w_{1,1}^{(l)} & \dots & w_{1,n}^{(l)} \\ \vdots & \vdots & \ddots & \vdots \\ w_{m,0}^{(l)} & w_{m,1}^{(l)} & \dots & w_{m,n}^{(l)} \end{bmatrix} \begin{bmatrix} a_0^{(l-1)} \\ a_1^{(l-1)} \\ \vdots \\ a_n^{(l-1)} \end{bmatrix} + \begin{bmatrix} b_0^{(l)} \\ b_1^{(l)} \\ \vdots \\ b_n^{(l)} \end{bmatrix} \quad (1.32)$$

where  $w_{m,n}^{(l)}$  denotes the weighting factor that associates the  $m^{th}$  node in  $(l - 1)^{th}$  layer to the  $n^{th}$  node in  $(l)^{th}$  layer,  $a_n^{(l-1)}$  denotes the activation of the  $n^{th}$  node in the  $(l - 1)^{th}$  layer, and  $b_n^{(l)}$  denotes the bias of the  $n^{th}$  node in the  $(l)^{th}$  layer. This matrix expression can be written in a simplified form:

$$z^{(l)} = W^{(l)} a^{(l-1)} + b^{(l)} \quad (1.33)$$

Then, the activation of  $l^{th}$  layer is expressed as

$$a^{(l)} = f(z^{(l)}) \quad (1.34)$$

### 1.3.2 Backward propagation training

A NN can be trained to carry out any desired results if enough training examples are provided. The training is an iterative process that the weighting factor  $w$  and the bias  $b$  of each node are optimized to make accurate NN predictions after many iterations. During each iteration, updates of parameters are governed by the gradient descent method, and take place in a fashion of backward propagation from the last layer back to the first layer. Details are discussed below.

For simplicity, assuming one training example is passed to a NN of  $L$  layers with a sigmoid activation function  $\sigma$  defined in equation 1.29, the NN prediction is the activation value of the last layer

$$a^{(L)} = \sigma(z^{(L)}) \quad (1.35)$$

where

$$z^{(L)} = W^{(L)}a^{(L-1)} + b^{(L)} \quad (1.36)$$

To evaluate how far the NN prediction of this particular training example is from its ground truth value  $y$ , a loss function  $\mathcal{L}$  is usually defined by the mean squared error (MSE) to take the form of

$$\mathcal{L} = (a^{(L)} - y)^2 \quad (1.37)$$

Starting from random weights  $W$  and biases  $b$  for the entire NN, a certain value of  $\mathcal{L}$  is obtained. Then, the task becomes to find the updated  $W$  and  $b$  values that can decrease  $\mathcal{L}$ . This is realized by gradient descending, which is taking the partial derivatives of  $\mathcal{L}$  with respect to  $W$  and  $b$ :

$$\begin{aligned} W_{new} &= W - \left(\alpha \times \frac{\partial \mathcal{L}}{\partial W}\right) \\ b_{new} &= b - \left(\alpha \times \frac{\partial \mathcal{L}}{\partial b}\right) \end{aligned} \quad (1.38)$$

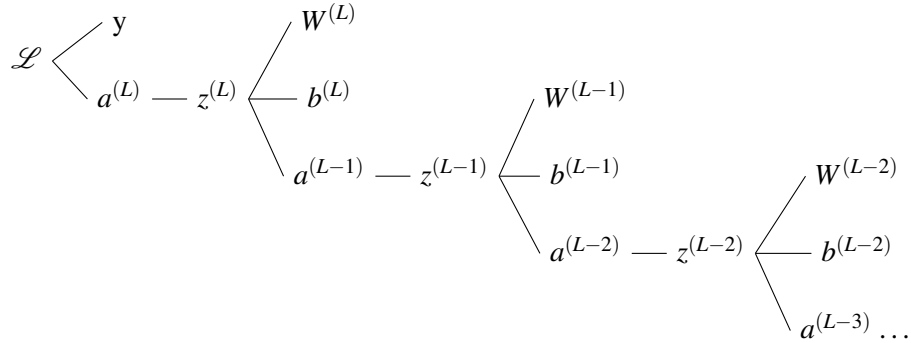


**Figure 1.15: Backward propagation.** A tree diagram depicts the backward propagation mechanism.

where  $\alpha$ , known as the learning rate, is the manually selected step size (usually small) of moving the  $W$  and  $b$  towards their gradient descending directions. Since the  $\mathcal{L}$  is not directly associated with most nodes of the NN except for those in the last layer, the update of parameters using equation 1.38 takes place in the last layer first and then propagates back to the previous layers. A schematic tree diagram is depicted in Figure 1.15 to illustrate the backward propagation mechanism, and the detailed calculations are discussed below.

First, only the last layer  $L$  is considered so that the partial derivative of  $\mathcal{L}$  with respect to  $w^{(L)}$  can be written using the chain rule

$$\frac{\partial \mathcal{L}}{\partial W^{(L)}} = \frac{\partial \mathcal{L}}{\partial a^{(L)}} \times \frac{\partial a^{(L)}}{\partial z^{(L)}} \times \frac{\partial z^{(L)}}{\partial W^{(L)}} \quad (1.39)$$

where the three terms on the right side can be solved, and their results are repre-

sented respectively by symbols ①, ②, and ③:

$$\frac{\partial \mathcal{L}}{\partial a^{(L)}} = \frac{\partial (a^{(L)} - y)^2}{\partial a^{(L)}} \quad (1.40)$$

$$= 2(a^{(L)} - y) = \textcircled{1} \quad (1.41)$$

$$\frac{\partial a^{(L)}}{\partial z^{(L)}} = \frac{\partial}{\partial z^{(L)}} \sigma(z^{(L)}) \quad (1.42)$$

$$= \frac{\partial}{\partial z^{(L)}} \left( \frac{1}{1 + e^{-z^{(L)}}} \right) \quad (1.43)$$

$$= \sigma(z^{(L)}) \times (1 - \sigma(z^{(L)})) = \textcircled{2} \quad (1.44)$$

$$\frac{\partial z^{(L)}}{\partial W^{(L)}} = \frac{\partial (W^{(L)} a^{(L-1)} + b^{(L)})}{\partial W^{(L)}} \quad (1.45)$$

$$= a^{(L-1)} = \textcircled{3} \quad (1.46)$$

so that

$$\frac{\partial \mathcal{L}}{\partial W^{(L)}} = \textcircled{1} \times \textcircled{2} \times \textcircled{3} \quad (1.47)$$

Similarly, the partial derivative of  $\mathcal{L}$  with respect to  $b^{(L)}$  can be written as

$$\frac{\partial \mathcal{L}}{\partial b^{(L)}} = \frac{\partial \mathcal{L}}{\partial a^{(L)}} \times \frac{\partial a^{(L)}}{\partial z^{(L)}} \times \frac{\partial z^{(L)}}{\partial b^{(L)}} = \textcircled{1} \times \textcircled{2} \times \frac{\partial z^{(L)}}{\partial b^{(L)}} \quad (1.48)$$

where the only unknown term can be easily solved:

$$\frac{\partial z^{(L)}}{\partial b^{(L)}} = \frac{\partial (W^{(L)} a^{(L-1)} + b^{(L)})}{\partial b^{(L)}} \quad (1.49)$$

$$= 1 \quad (1.50)$$

so that

$$\frac{\partial \mathcal{L}}{\partial b^{(L)}} = \textcircled{1} \times \textcircled{2} \quad (1.51)$$

Then, according to equation 1.38, the updated weights and biases of the last layer are calculated as

$$W_{new}^{(L)} = W^{(L)} - (\alpha \times \textcircled{1} \times \textcircled{2} \times \textcircled{3}) \quad (1.52)$$

$$b_{new}^{(L)} = b^{(L)} - (\alpha \times \textcircled{1} \times \textcircled{2})$$

Carrying out the updated weights and biases of the second last layer requires

the partial derivative of  $\mathcal{L}$  with respect to  $a^{(L-1)}$  to be calculated in advance:

$$\frac{\partial \mathcal{L}}{\partial a^{(L-1)}} = \frac{\partial \mathcal{L}}{\partial a^{(L)}} \times \frac{\partial a^{(L)}}{\partial z^{(L)}} \times \frac{\partial z^{(L)}}{\partial a^{(L-1)}} = \textcircled{1} \times \textcircled{2} \times \frac{\partial z^{(L)}}{\partial a^{(L-1)}} \quad (1.53)$$

where the only unknown term can be solved, and represented by symbol  $\textcircled{4}$ :

$$\frac{\partial z^{(L)}}{\partial a^{(L-1)}} = \frac{\partial (W^{(L)} a^{(L-1)} + b^{(L)})}{\partial b^{(L)}} \quad (1.54)$$

$$= W^{(L)} = \textcircled{4} \quad (1.55)$$

so that

$$\frac{\partial \mathcal{L}}{\partial a^{(L-1)}} = \textcircled{1} \times \textcircled{2} \times \textcircled{4} \quad (1.56)$$

Then, the partial derivative of  $\mathcal{L}$  with respect to  $W^{(L-1)}$  can be written as

$$\frac{\partial \mathcal{L}}{\partial W^{(L-1)}} = \frac{\partial \mathcal{L}}{\partial a^{(L-1)}} \times \frac{\partial a^{(L-1)}}{\partial z^{(L-1)}} \times \frac{\partial z^{(L-1)}}{\partial W^{(L-1)}} \quad (1.57)$$

where the second and the third terms on the right side are

$$\frac{\partial a^{(L-1)}}{\partial z^{(L-1)}} = \sigma(z^{(L-1)}) \times (1 - \sigma(z^{(L-1)})) = \textcircled{5} \quad (1.58)$$

$$\frac{\partial z^{(L-1)}}{\partial W^{(L-1)}} = \frac{\partial (W^{(L-1)} a^{(L-2)} + b^{(L-1)})}{\partial W^{(L-1)}} \quad (1.59)$$

$$= a^{(L-2)} = \textcircled{6} \quad (1.60)$$

so that

$$\frac{\partial \mathcal{L}}{\partial W^{(L-1)}} = \textcircled{1} \times \textcircled{2} \times \textcircled{4} \times \textcircled{5} \times \textcircled{6} \quad (1.61)$$

Note that  $\textcircled{5}$  and  $\textcircled{6}$  have similar forms as  $\textcircled{2}$  and  $\textcircled{3}$  respectively, but they have distinct values since they represent different layers. In a similar way, the partial derivative of  $\mathcal{L}$  with respect to  $b^{(L-1)}$  can be solved as

$$\frac{\partial \mathcal{L}}{\partial b^{(L-1)}} = \textcircled{1} \times \textcircled{2} \times \textcircled{4} \times \textcircled{5} \quad (1.62)$$

Again, according to equation 1.38, the updated weights and biases of the second

last layer are calculated as

$$\begin{aligned} W_{new}^{(L-1)} &= W^{(L-1)} - (\alpha \times \textcircled{1} \times \textcircled{2} \times \textcircled{4} \times \textcircled{5} \times \textcircled{6}) \\ b_{new}^{(L-1)} &= b^{(L-1)} - (\alpha \times \textcircled{1} \times \textcircled{2} \times \textcircled{4} \times \textcircled{5}) \end{aligned} \quad (1.63)$$

Recursively using the described mechanism above, the updated weights and biases of all layers can be subsequently worked out from the last layer to the first layer, as depicted in Figure 1.15. Then, one round of backward propagation is completed.

Although up to this point that only one training example is considered, extending the current formalism to  $n$  training examples is straightforward. The only extra work is that a cost function  $C$  is defined to sum up the losses (e.g. MSE) of all training examples

$$C = \frac{1}{n} \sum_{i=1}^n \mathcal{L}_i \quad (1.64)$$

$$= \frac{1}{n} \sum_{i=1}^n (a_i^{(L)} - y_i)^2 \quad (1.65)$$

where  $\mathcal{L}_i$ ,  $a_i^{(L)}$ , and  $y_i$  are the loss, the NN prediction, and the ground truth values of the  $i^{\text{th}}$  training example, respectively. Consequently,  $C$  is now used to evaluate the overall NN prediction error for  $n$  training examples, and it should be minimized using the gradient descending method. Thus, the updating rule for the weights and biases becomes to

$$\begin{aligned} W_{new} &= W - \left( \alpha \times \frac{\partial C}{\partial W} \right) \\ b_{new} &= b - \left( \alpha \times \frac{\partial C}{\partial b} \right) \end{aligned} \quad (1.66)$$

Similarly,  $W_{new}$  and  $b_{new}$  can be solved from the last layer to the first layer by recursively applying the chain rule illustrated above, with the loss function  $\mathcal{L}$  substituted with the cost function  $C$ . Once the backward propagation is completed, the entire NN is updated with new weights and biases, so that another round of forward propagation and backward propagation will take place repeatedly until the customized stopping criterion is met, and then the NN is trained.

### **1.3.3 Training strategy**

A common problem with a trained NN is overfitting, which means it performs well on the already-seen training data but not as well on the never-seen new data. Because of the huge number of parameters (weights and biases), a NN certainly has the ability to overfit the training data. Fortunately, the overfitting problem can be largely mitigated by using some strategies for training the NN, resulting in the trained NN a generalized model that performs somewhat equally well on either training data or new data.

First of all, the overfitting can be observed only when the NN is confronting new data. Therefore, the available data are randomly shuffled and partitioned into three groups: training set, validation set, and testing set, and let the NN learn by only seeing the training set. The validation set is used at the end of each training iteration to have the NN prediction accuracy on the validation set measured. The training process will be stopped when the accuracy on the validation set does not improve further. At last, the testing set is only used once, after the NN training is completed, to evaluate the NN performance as a generalized model. The common splits for the training, validation, and testing partitions are approximately 60%, 20%, and 20%. This described strategy is applied in this thesis.

Other training strategies [194] for preventing the overfitting problem, such as the regularization method that constraints the weights, and the drop-out method that shuts down random nodes, are not discussed here since they are not practiced in this thesis.

## **1.4 Thesis overview**

In general, the thesis work involves three aspects of MWI: application, atlases, and algorithms (Figure 1.16). The main body of the thesis starts with applying the available MWI technique in the spinal cord to examine the correlation of myelin structure and function (Chapter 2), followed by creating MWI atlases that map the myelin distribution in the healthy brain and spinal cord (Chapter 3 & 4), and finally developing novel methods to improve the MWI data analysis (Chapter 5 & 6). Each chapter from Chapter 2 to Chapter 6 is written in the fashion of an independent research report that consists of its own introduction, methods, results,

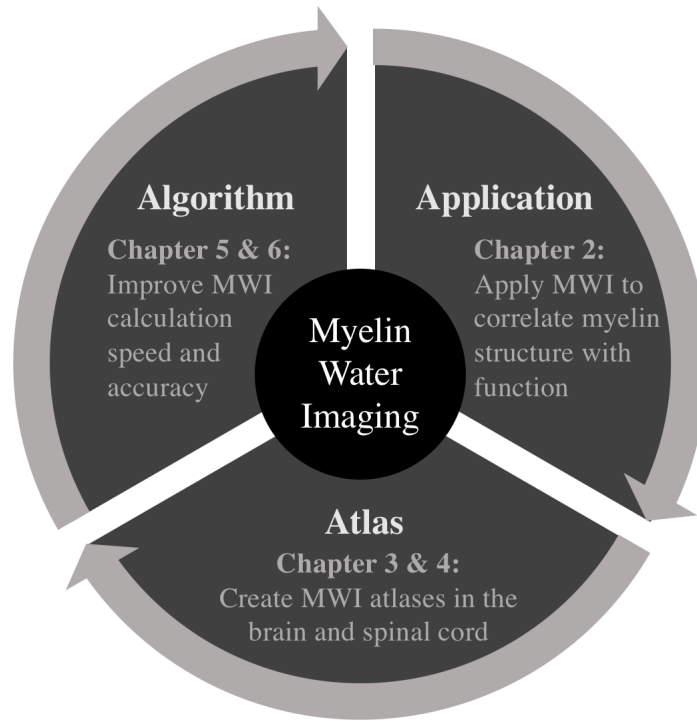


**Figure 1.16: Overview of the thesis.**

discussion, and conclusion. The scope of this thesis only became clear after an initial exploratory in one application of MWI and the recognition of MWI limitation in individual usage illustrated in Chapter 2. The latter chapters were subsequently developed to improve the feasibility of MWI for clinical use at an individual level.

Specifically, Chapter 2 illustrates the correlation of the deficits in function and the damages in myelin, which is measured by applying MWI in the cervical spinal cords from both healthy and pathological cohorts.

Chapter 3 & 4 demonstrate the creations and the utilities of MWI atlases of the spinal cord (Chapter 3) and the brain (Chapter 4). The atlases created by co-registering the MWI images from many healthy volunteers show distinct myelin abundances in different spinal cord pathways and brain regions.

Chapter 5 shows the performance and robustness of a NN model designed for a faster MWI data analysis. The trained NN model is able to calculate the whole

brain MWF map in approximately 30 seconds, achieving an acceleration factor of 150, compared with the conventional analysis pipeline illustrated in section 1.2.4.

Chapter 6 introduces a fundamentally different approach to carry out the MWI data analysis. In contrast to the NNLS-based method discussed in section 1.2.4, the proposed method is a simulation-derived solver that improves the accuracy and stability of the  $T_2$  decay decomposition.

Finally, Chapter 7 recaps each chapter and concludes the key results in this thesis, as well as unveils some of the future work.

## **Chapter 2**

# **Assessing structure and function of myelin in cervical spondylotic myelopathy: Evidence of demyelination\***

### **2.1 Introduction**

Cervical spondylotic myelopathy (CSM) is the leading cause of mobility deficits related to damage in the spinal cord for people over the age of 55. [122, 154, 185] CSM results from static or dynamic spinal cord compression and interrupts the normal flow of nerve impulses. If CSM symptoms persist or worsen, surgical intervention is the frontline strategy to relieve neurological symptoms. [62, 63, 167] The key to achieving good surgical outcomes is timely and accurate diagnosis (i.e., before the establishment of definite spinal cord damage that is non-responsive to surgical decompression). This relies on a combination of clinical symptoms and findings on magnetic resonance imaging (MRI). [105, 219, 234] However, rou-

---

\*A version of this chapter has been published. Liu H, MacMillian EL, Jutzeler CR, Ljungberg E, MacKay AL, Kolind SH, Mädler B, Li DK, Dvorak MF, Curt A, Laule C, and Kramer JL. Assessing structure and function of myelin in cervical spondylotic myelopathy: evidence of demyelination. *Neurology*. 2017 Aug 8;89(6):602-10.

tine outcomes from conventional MRI, such as maximal spinal cord compression (MSCC) and the presence of increased cord signal on T<sub>2</sub> weighted images, are not sensitive enough to identify clinically relevant pathologies that lead to symptoms and warrant surgical intervention. Moreover, single changes in the spinal cord may be a function of edema or myelomalacia, which are unrelated to pathology at the microstructure level (i.e., white and gray matter). [25, 83] This is a problem because an estimated 20-25% of otherwise healthy individuals will present with some form of cervical stenosis, not all of which requires treatment. [20, 153] To improve the diagnostic accuracy of MRI, conventional MRI outcomes have been paired with quantitative imaging techniques (e.g., diffusion tensor imaging (DTI)) and electrophysiological techniques. [26, 38, 42, 168, 186, 204, 211]

Myelination of nerve fibre tracts plays a critical role in the conduction of sensory and motor signals along the axon, allowing complex motor and sensory behaviors. Demyelination is commonly associated with a number of neurological conditions affecting the central nervous system, including the brain and spinal cord. [37, 109, 157] Evidence from post-mortem histological studies demonstrates that demyelination occurs at the lesion site in patients with CSM. [90, 230] In vivo morphological evidence of demyelination, however, are lacking. To date, a major limitation of studies applying advanced quantitative imaging in CSM patients has been that many outcomes are not specific for myelin. For example, fractional anisotropy (FA), an outcome from diffusion tensor imaging (DTI), can be dramatically affected by axonal loss or mechanical deformation without relevant demyelination. [4, 222]

Myelin water imaging (MWI) has been proposed as a specific measure of myelin. [146] MWI operates on the principle that the MR signal from myelin water, the water trapped between myelin bilayers, can be extracted from the total MR signal based on a characteristic short T<sub>2</sub> relaxation time. The ratio of myelin water signal relative to the total signal is termed myelin water fraction (MWF). Histological studies have validated MWF as an in vivo surrogate measure of myelin. [111, 112, 119] Since the introduction of MWI, MWF has been widely applied in the brain and spinal cord of various neurodegenerative diseases that involve demyelination, including multiple sclerosis [163, 196, 217], phenylketonuria [196], and schizophrenia [70].

We propose that MWI is well suited to be used as a diagnostic test of the clinical severity of CSM and would complement functional assessments of myelin integrity by providing spatially specific information about myelin damage. Thus, the goal of our study was to investigate, for the first time, the application of MWI to detect myelin damage in patients with CSM. We hypothesized that MWI would provide evidence of demyelination and correlate with physiological measurements of spinal cord conduction in CSM.

## **2.2 Methods**

### **2.2.1 Standard Protocol Approvals, Registrations, and Patient Consents**

All individuals provided written informed consent and all procedures described below were in accordance with the Declaration of Helsinki and approved by the local ethics board (UBC CREB #H06-00282).

### **2.2.2 Participants**

A total of 15 CSM individuals were recruited from the Vancouver Spine Program. CSM was determined based on typical clinical symptoms (e.g. clumsiness in the hands, pain, weakness, numbness, sensorimotor deficit) and evaluation of conventional MRI by the study neurologist (AC). All CSM individuals have not yet undergone decompressive surgery. Twenty age-matched healthy individuals from the community were enrolled as healthy controls.

### **2.2.3 Clinical assessments**

Prior to the MRI, all individuals were interviewed to assess their general health and well-being by using the SF-36 questionnaire. [92] In individuals with CSM, the modified Japanese Orthopaedic Association (JOA) score was used to assess the severity of clinical symptoms. [71, 231] The Nurick Score was used for stratifying the level of functional restriction in mobility (Grade 0 to 5: 0=No evidence of spinal cord disease, 5= chair- or bed-bound) caused by cervical myelopathy. [172] The neurological level of stenosis was determined using the International Standards

for Neurological Classification of Spinal Cord Injury published by the American Spinal Injury Association (ASIA). [98]

#### **2.2.4 Electrophysiology**

The spinal conduction is measured by somatosensory evoked potential (SSEP) technique, which records the signal latency at the cortical level after extremity stimulation. Standard tibial SSEPs were elicited through repetitive electrical stimulation (repetitive square wave impulse of 0.5-millisecond duration) of the posterior tibial nerves at the medial ankle. SSEPs were elicited using self-adhesive bipolar stimulation electrodes and the Keypoint recording device (Medtronic, Minneapolis, MN). Cortical responses (N40-P43) were recorded using silver-silver disc recording electrodes that were positioned according to the 10-20 system, with the active electrode at Cz and referenced to Fz. In addition to the cortical response, evoked responses were acquired at the popliteal fossa (N9, peripheral measure of the afferent volley) to assure appropriate stimulation and exclude impairment of peripheral nerve conduction. Stimulation frequency was set at 3.1 Hz and two traces of 200 stimulations were applied per site and eventually averaged for visual detection of N40-P43 waveform. Electrode impedance was kept below 5k $\Omega$ , which was verified prior to the initiation of each session and all signals were sampled at 10 kHz and bandpass filtered 2 Hz to 2 kHz. Averaged SSEPs were visually inspected for N40 and P43 latencies and N40-P43 amplitude. Accounting for study participant height, SSEP amplitude, latency and configuration were evaluated against standard laboratory control values. [39]

#### **2.2.5 MRI experiments**

All individuals were scanned on a 3.0T MRI system (Philips, Best, The Netherlands) with a phased array spine coil using only the first four channels for best localization of the cervical spinal cord. Localizer and sagittal T<sub>2</sub> weighted imaging sequences (TR = 3314ms, TE = 120ms) were applied first for the purposes of spinal cord localization and axial slices alignment. Myelin water imaging (MWI) was performed using a multi-echo T<sub>2</sub> relaxation experiment (3D 32-echo sequence, 1st echo = 10ms, echo spacing = 10ms, TR = 1300ms, eight 5mm thick axial slices

perpendicular to the spinal cord,  $256 \times 128$  matrix, FOV  $180\text{mm} \times 135\text{mm}$ , reconstructed in-plane resolution  $0.7\text{mm} \times 0.7\text{mm}$ ; acquisition time of 20.3 minutes). [148] Positioning of the 3D stack was centered at the level of stenosis in CSM participants. C5 was planned for all healthy controls based on the rationale that the majority of CSM participants would have stenosis at or within one spinal segment (i.e., C4-C6). A previous study indicates minimal variation in MWF between cervical spinal segments. [162] The MWI Scan-rescan repeatability was tested and reported by MacMillan et al. [147]

### **2.2.6 MWI Data Analysis**

Voxel-wise  $T_2$  decay curve analysis used a regularized non-negative least squares (NNLS) algorithm with in-house software (MATLAB, The MathWorks, Inc., Natick, Massachusetts, U.S.), which employed the extended phase graph algorithm to estimate the refocusing flip angle in each voxel as well as correcting the  $T_2$  decay curve for stimulated echo artifacts. This algorithm and its performance have been documented by Prasloski et al. [176] The MWF, which measures water trapped between myelin bilayers, was defined as the fractional signal with  $T_2$  less than 35ms. [147] MWF was calculated for each voxel to produce a MWF map. For each study participant, the average MWF in the whole cord and dorsal column were calculated in three steps using FMRIB's software library (FSL) [201] (Figure 2.1): (1) manually drawing regions of interest (ROI includes dorsal columns and whole cord), independently performed by two experienced researchers (HL, CL), on each slice of  $T_2$  weighted images ( $TE = 90 - 120\text{ms}$ ) from the 3D multi-echo  $T_2$  experiment for better anatomical contrast; (2) combining the ROIs over the 6 middle slices (the first and last slices are discarded due to phase wrapping in the through-plane direction) to yield a volume of interest; (3) calculating the average MWF within the volume of interest.

### **2.2.7 Compression Ratio, MSCC and MCC**

Axial and sagittal  $T_2$ -weighted images were examined for  $T_2$  intensity signal changes at the level of stenosis, compression ratio, maximum spinal cord compression (MSCC) and maximum canal compromise (MCC).  $T_2$  intensity changes were ex-

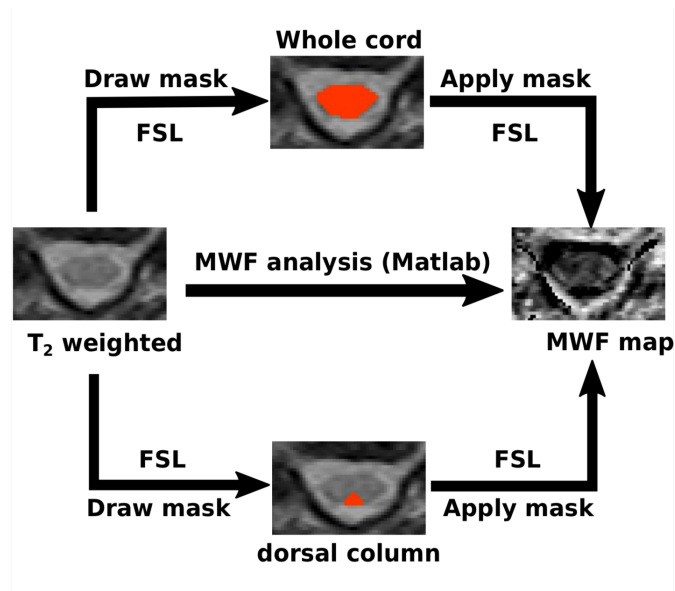


**Figure 2.1: Work flow chart.** One example is depicted here for calculating the average MWF in the whole cord and dorsal column.

amined by an experienced radiologist. Compression ratio was calculated by taking the anterior-posterior diameter of the spinal cord divided by the transverse diameter of the cord on the axial image. Lower compression ratio values indicate worse cord deformation. MSCC and MCC were assessed on the mid-sagittal slice of the T<sub>2</sub>-weighted spinal cord images using the method introduced by Nouri et al. [171] Unlike compression ratio, higher values of MSCC and MCC correspond to more severe cord deformation. Detailed calculation steps for compression ratio, MSCC and MCC are described in Figure 2.2A and 2.2B.

### 2.2.8 Statistical Analysis

Non-parametric tests (Mann-Whitney-U) were applied to determine significant differences in spinal cord compression, anterior-posterior width, transverse (left-right) and tibial SSEP latencies between control individuals and patients with CSM. Univariate general linear models (GLMs) were employed to assess the relationship between MWF, SSEPs, and CSM classification. In the initial models (Model 1), the main effect of CSM classification was examined. CSM was included as a fixed

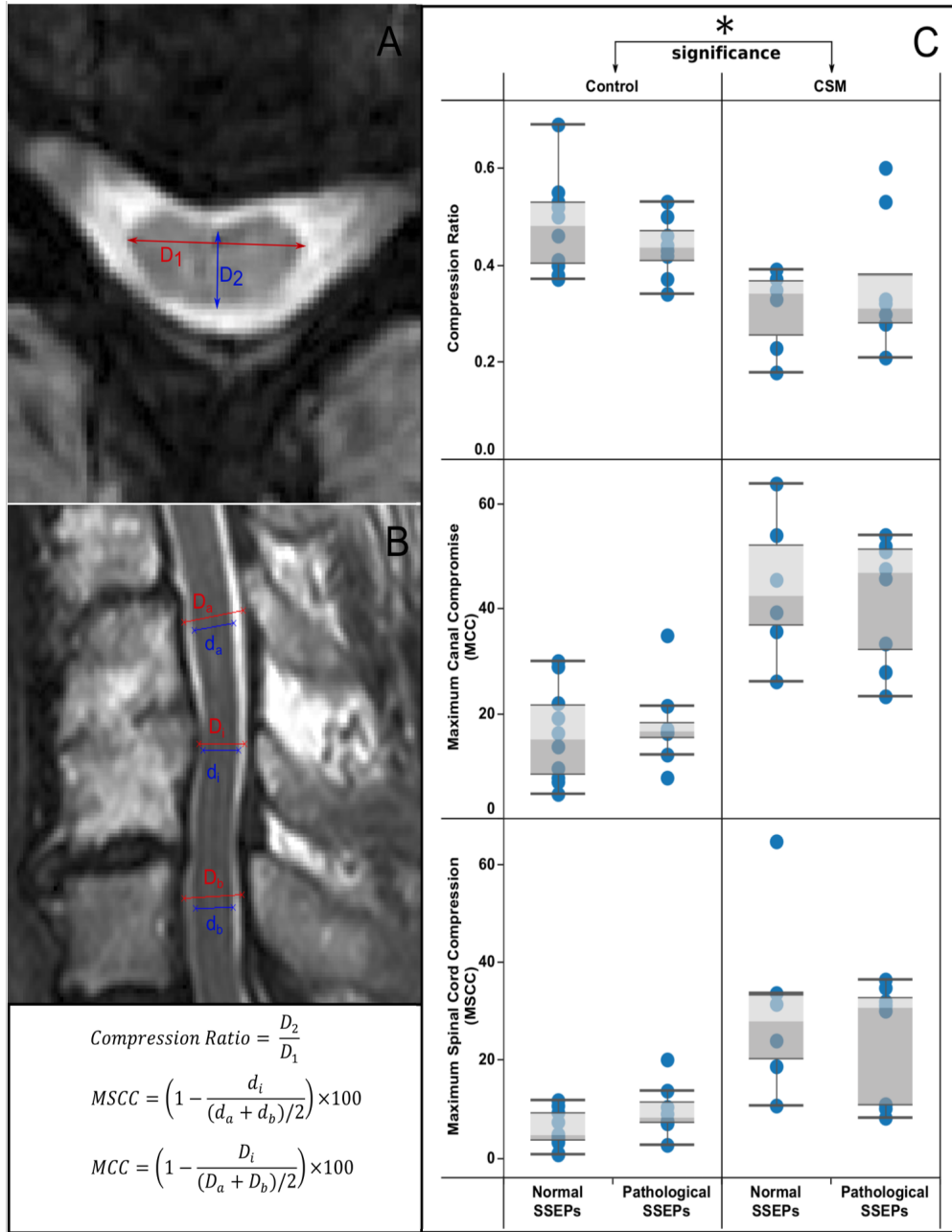


**Figure 2.2: Calculations of conventional MRI parameters and comparisons between healthy controls and CSM patients.** (A) & (B): The methods for calculating compression ratio, maximum spinal cord compression (MSCC) and maximum canal compromise (MCC).  $D_1$ : transverse diameter;  $D_2$ : anterior-posterior diameter;  $D_i$  ( $d_i$ ): canal (spinal cord) diameter at compression level;  $D_a$  ( $d_a$ ): canal (spinal cord) diameter of non-compressed level from above;  $D_b$  ( $d_b$ ): canal (spinal cord) diameter of non-compressed level from below. (C) Significant differences were observed in compression ratio, maximum spinal cord compression (MSCC) and maximum canal compromise (MCC) between healthy controls and CSM patients.

factor ('yes'/'no'). In a subsequent models (Model 2), SSEPs ('normal'/'pathological') and the interaction with CSM classification were examined. GLMs were run separately for dorsal column and whole cord and right and left SSEPs.  $P < 0.05$  was set as the threshold for significance.

## **2.3 RESULTS**

### **2.3.1 Participants**

Out of 15 patients with CSM enrolled in the study, one had to be excluded due to an incomplete data set (missing MR scan for MWI). The remaining 14 patients comprised of 11 males and 3 females with a mean age of  $61.0 \pm 9.3$  years (range from 46 to 77 years). According to established classification guidelines [67], CSM severity was as follows: 11 mild ( $JOA \geq 15$ ), 2 moderate ( $JOA = 12-14$ ), and 1 severe ( $JOA < 12$ ). Out of 20 healthy controls, two had to be excluded for missing data (i.e., could not perform MRI). The remaining 18 healthy controls were enrolled in the study (9 males, 9 females, mean age  $58.5 \pm 7.6$  years (range from 50 to 75 years)). The characteristics of the all study participants are summarized in Table 2.1.

### **2.3.2 Neuroimaging: Structural and signal changes at the spinal cord**

Overall, compression ratio was increased by 35.3% ( $p=0.002$ ) in the CSM patients at the level of stenosis compared to healthy controls at the level of C5. Compared to healthy controls, differences in anterior-posterior width were observed in patients with CSM ( $p=0.001$ ). No differences between control and CSM groups were detected regarding transverse (left-right) axis ( $p=0.244$ ). Compression ratio, MSCC, MCC and compression levels are shown in Table 2.1. Five healthy controls and all CSM patients were found to have spinal cord compression.  $T_2$  signal changes (hyper-intensity) were observed in 10 CSM participants but not in controls. Corresponding with diagnosis of CSM, there were large differences in compression ratio, MSCC, and MCC between controls and CSM patients (Table 2.1).

**Table 2.1: Demographic, neuroimaging, and neurophysiologic details of the study cohorts.** Abbreviations: CSM = cervical spondylotic myelopathy; JOA = Japanese Orthopaedic Association; SSEP = somatosensory evoked potential. Results are displayed as mean±SD.

Parameters	Controls	CSM	t-tests
<b>Demographics</b>			
Gender [male : female]	9:9	9:5	
Age [yrs]	58.5 ± 7.6	61.0 ± 9.3	p = 0.411
Height [cm]	171.1 ± 8.7	167.2 ± 10.5	p = 0.274
JOA Score	16.9 ± 0.4	14.9 ± 2.4	p = 0.002
<b>Neuroimaging parameters</b>			
T <sub>2</sub> signal changes [Yes : No]	0:18	10:04	
Spinal Cord Compression Ratio	0.46 ± 0.09	0.34 ± 0.1	p = 0.002
Anterior-posterior width [mm]	5.7 ± 0.9	4.1 ± 1.6	p = 0.001
Transverse width [mm]	12.6 ± 0.9	12.1 ± 1.6	p = 0.290
Maximum Spinal Cord Compression	7.5 ± 4.9	27.0 ± 15.0	p = 0.0001
Maximum Canal Compromise	16.8 ± 8.4	42.9 ± 12.1	p < 0.0001
Myelin Water Fraction Whole Cord	0.26 ± 0.03	0.24 ± 0.04	p = 0.166
Myelin Water Fraction Dorsal Column	0.28 ± 0.04	0.27 ± 0.04	p = 0.283
<b>Compression level (# of participants)</b>			
C4/C5	2	2	
C5/C6	3	11	
C6/C7		1	
<b>Neurophysiological parameters</b>			
Left tibial SEP N40 latency [ms]	44.0 ± 4.2	43.7 ± 3.8	p = 0.873
Right tibial SEP N40 latency [ms]	44.8 ± 7.1	43.4 ± 3.5	p = 0.514

### 2.3.3 Neurophysiological assessments: Changes in spinal conduction and associations with conventional MRI outcomes

Tibial SSEP latencies of both groups are summarized in Table 2.1. Mean latencies for tibial (left or right) were not different between CSM patients and healthy controls (tibial<sub>left</sub>: p=0.873; tibial<sub>right</sub>: p=0.514) (Figure 2.3). Eight healthy controls and eight CSM patients were classified as having pathological SSEPs.

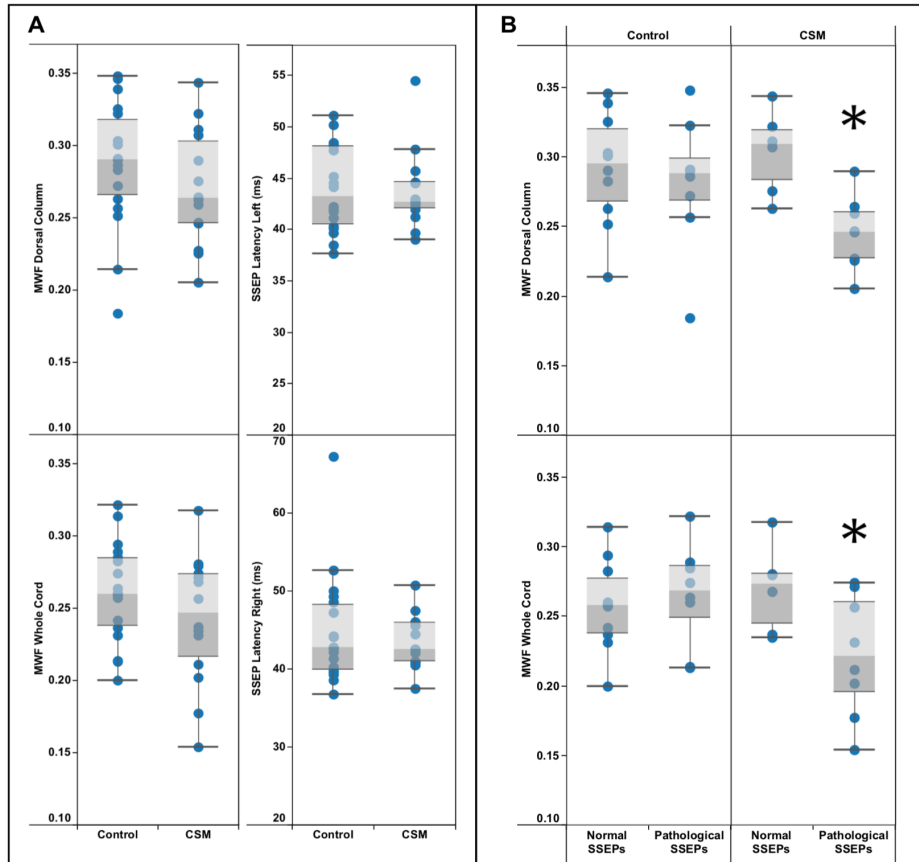


**Figure 2.3: MWF and SSEPs comparisons between healthy controls and CSM patients (A), and interaction effect (B).** A): Myelin water fraction (MWF) (whole cord and dorsal column) and tibial SSEP latencies (left and right) between healthy controls and CSM patients are compared. No differences were observed between groups. B) An interaction between the interpretation of tibial SSEPs ('pathology'/'normal') the diagnosis of CSM ('yes'/'no') was observed for MWF of the whole cord. Patients with CSM and pathological tibial SSEPs had reduced MWF (indicated by \*).

### 2.3.4 Myelin damage in CSM patients: Relationship between neurophysiological and neuroimaging parameters

According to our first GLM (Model 1), there were no differences in MWF of the whole cord ( $p=0.166$ ) or dorsal column ( $p=0.284$ ) between CSM and controls (Figure 2.3). Besides, there were no differences in MWF of the whole cord ( $p=0.488$ ) or dorsal column ( $p=0.622$ ) between the CSM subgroups of T<sub>2</sub> signal changes ('yes'/'no'). Model 2 revealed an interaction between CSM classification and SSEP interpretation in whole cord MWF (left SSEP:  $p=0.009$ ; right SSEP:  $p=0.049$ ). Overall, our observations indicate that patients with CSM and pathological tibial SSEPs had marked lower myelin content.

## 2.4 Discussion

Based on an *in vivo* measure specific to myelin, our findings demonstrate that CSM is associated with microstructural changes in spinal cord white matter. Microstructural changes in myelin were demonstrated using MWI and evidenced in a cohort of CSM patients with accompanying neurophysiological deficits. We have provided *in vivo* anatomical evidence of demyelination related to conduction deficits in patients with CSM.

MWF as a surrogate marker of myelin has previously been demonstrated in post-mortem combined MRI and histological studies. [111, 112, 119] Consistent with these *ex vivo* observations, MWF is sensitive to changes in patient populations commonly associated with demyelination in the CNS. However, the primary focus of *in vivo* MWF applications in patients has been almost exclusively in the brain.

Post-mortem histologic study of spinal cords suggests that myelinated long tracts are affected in patients with CSM. [90] This includes evidence of demyelination at the lesion site. Preclinical studies suggest CNS myelin is susceptible to ischemic injury resulting from spinal cord compression. [73] Corresponding *in vivo* evidence of white matter pathology has been largely elucidated based on DTI. [26, 32, 60] Results from DTI measurement showed strong sensitivity for detecting microstructural changes and correlations with clinical scores. However, DTI metrics are not specific to the type of damage, which may include a combination of inflammation, demyelination and/or axonal loss. [4] Thus, based solely on these

studies, it is difficult to conclude whether CSM is affecting myelin or, more generally, the composition of spinal cord axons due to mechanical deformation.

Few studies have applied both quantitative MRI and an electrophysiological approach to examine CSM. [59, 86] The advantage of combining both techniques is that they are unbiased by what an individual is functionally capable of performing (e.g. JOA). This combined approach is powerful for understanding the pathophysiology and anatomy of CSM. [60] An important outcome of our study was that conventional CSM diagnosis alone yielded no obvious differences in neurophysiological or MWI parameters (Figure 3A). Consistent with previous literature, approximately 60% of patients with CSM in our study presented with pathological SSEPs. [94] An equal number (n=8) and approximately half of healthy controls also demonstrated pathological SSEPs. MWF values in healthy controls was comparable to previous studies [118, 147, 162], and not different from CSM patients on a group level. In contrast to healthy controls, pathological SEP classification in individual CSM patients was associated with reduced MWF (Figure 2.3). In pragmatic terms, this means that microstructural changes in white matter become evident in clinically obvious CSM symptoms (e.g., clumsiness) that are also accompanied by objective measures of spinal cord pathology (e.g., impaired SSEPs). The linear correlations of SEP latency and MWF (dorsal column and whole cord) are also only observed in CSM patients (Figure 2.4). From pathophysiological considerations, decreases in MWF are not linearly related to pathological SSEPs as shown in healthy controls. Obviously changes in SSEPs in healthy aged controls respond also to other change in CNS and PNS microstructure, which are undetected by MWI of the cord. The age-matched CSM patients would be expected to undergo these same changes, however additionally accompanied by persistent compression of the spinal cord - the latter yielding a reduction in MWF.

Our study specifically examined the spinal cord MWF in patients with CSM. The application of MWI to the spinal cord has historically lagged behind that of brain studies due to the general technical challenges of imaging spinal cord microstructure using MRI. [81] By taking advantage of the development of a 3D multi-echo pulse sequence, it is now possible to achieve multi-slice coverage of the spinal cord with shorter acquisition time compared to previous single slice acquisitions. [118] Also, the in-plane resolution ( $0.7\text{mm}\times 0.7\text{mm}$ ) is sufficient to

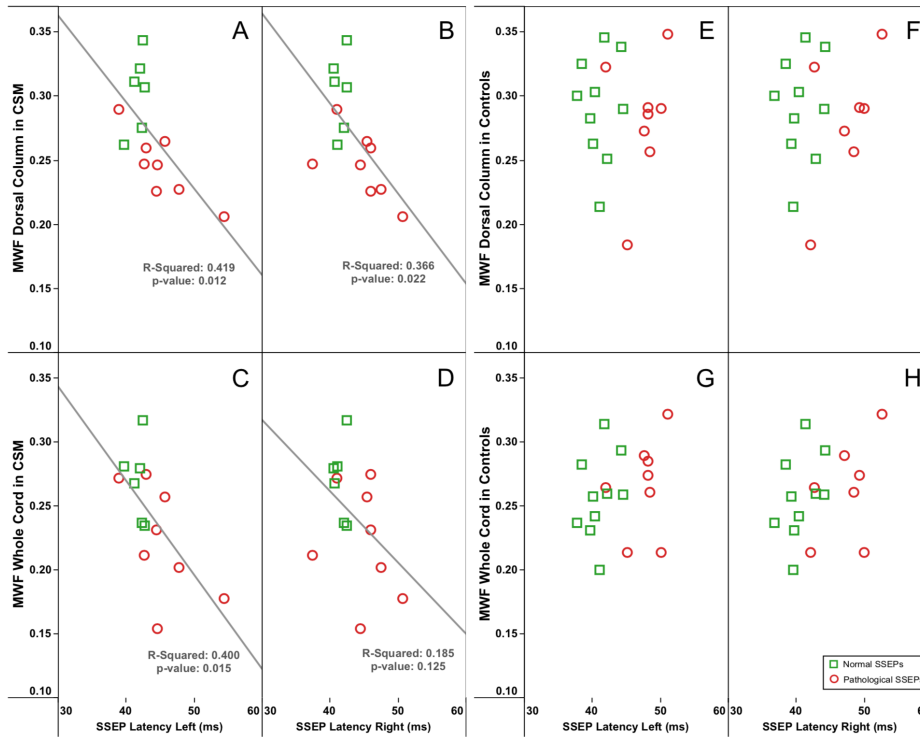


**Figure 2.4: Correlations between SSEPs and MWF in CSM patients and healthy controls.** Correlations of tibial SSEPs (left and right) with dorsal column and whole cord myelin water fraction (MWF) in CSM participants (A-D) and healthy controls (E-H). Significant correlations are only found in CSM group (trend lines are fitted R-Squared and p-value). No correlations are observed in healthy controls.

resolve detailed anatomical structures (e.g. the butterfly pattern of white and grey matter on the axial plane). Reliability and repeatability of applying MWI using the current 3D multi-echo sequence in cervical spinal cord are acceptable and have been examined elsewhere. [147] <sup>18</sup> In all participants, dorsal column MWF average ( $0.280 \pm 0.042$ ) was higher than that of the whole cord ( $0.253 \pm 0.040$ ). Lower whole cord MWF reflects the inclusion of unmyelinated grey matter in the ROI, leading to lower relative values, in comparison to the dorsal column ROIs which are white matter.

A number of limitations warrant consideration. First, the specificity and sen-

sitivity of MWI to accurately diagnosis CSM cannot be fully addressed due to the small number of patients. Also, the current MWI technique cannot distinguish between intact and pathological myelin. Second, manual ROIs may introduce bias to the analysis. Future investigations should consider automatic segmentation tools, which have only recently become available for the spinal cord. [129] Lastly, the 20-minute acquisition time for MWI is long and may be difficult for some patients. Towards improving clinical applicability, recent advances in MWI have dramatically reduced scanning time to approximately 8 minutes. [141]

## **2.5 Conclusion**

In conclusion, combining neurophysiological and neuroimaging outcomes revealed considerable changes in white matter integrity related to spinal cord compression. Microstructural changes in myelin were specifically observed in a cohort of patients with pathological spinal conduction. In the future, MWI may be a useful tool for prognosis related to interventions aimed at reducing the functional consequences of CSM.

As mentioned in the limitation, the available MWI technique would require a large number of study participants to detect the group difference if it exists. This limitation hindered the utility of MWI at the individual level but intrigued the work of the next two chapters.

## Chapter 3

# Myelin water atlas for the spinal cord at 3T MRI\*

### 3.1 Introduction

Myelin is an insulating sheath around central nervous system (CNS) axons which is crucial for rapid signal conduction. [68] Myelin damage or loss can occur in spinal cord injuries (SCI) or neurodegenerative diseases, leading to impaired function of the CNS. Quantitative in-vivo measurement of myelin is thus highly desirable to better assess the prognosis, severity and progression of spinal cord injury and disease, and may provide valuable guidance for treatment planning. However, reliably detecting the change of myelin content on an individual-level is still very challenging for a number of reasons.

The first challenge comes from technical difficulties in detecting in-vivo myelin in the spinal cord. Several advanced magnetic resonance imaging (MRI) techniques have been developed to quantify the myelin content in the CNS, such as diffusion tensor imaging (DTI) and magnetization transfer imaging (MTI). [189, 198, 202, 203] Applying these techniques in the spinal cord [10, 34, 61, 82, 199]

---

\*A version of this chapter has been published. Liu H, Ljungberg E, Dvorak AV, Lee LE, Yik JT, MacMillan EL, Barlow L, Li DK, Traboulsee A, Kolind SH, Kramer JL. Myelin Water Fraction and Intra/Extracellular Water Geometric Mean  $T_2$  Normative Atlases for the Cervical Spinal Cord from 3T MRI. *Journal of Neuroimaging*. 2019 Aug 13;30(1):50-57.

is intrinsically more difficult than in brain due to the possible artifacts from physiological motion and small cross-sectional dimensions of the cord, and inhomogeneous magnetic field in this region. [207] These factors make individual imaging results less reliable and more difficult to interpret. For this reason, group comparisons are often used in many studies to detect the differences between control and disease cohorts. In addition, while DTI and MTI are undoubtedly sensitive to pathological changes, they are affected not only by changes in myelin but also other factors including edema, inflammation, and gliosis. [135]

Another challenge is that normal myelin variability in the healthy population is not well characterized. Myelination has been reported to vary with age. [68] Other factors such as sex, laterality, and ethnicity may also have unknown effects on the formation and development of normal myelin. These possibly myelin-related factors make the interpretation of individual imaging results more difficult. In a clinical setting, it is not feasible to scan a perfectly matched healthy control for every individual patient. Furthermore, collecting control data for every clinical or research study is costly, diverting funds from acquiring more data on patients.

Unfortunately, the above challenges cannot be fully addressed on an individual-level with current technology. To mitigate these challenges we propose to create an in-vivo myelin atlas for the spinal cord. Since the atlas is essentially an average image of many healthy subjects, signal to noise ratio (SNR) of the atlas will be drastically improved, compared to a single individual, and the atlas is expected to show superior image quality and thus greater details about myelin distribution. In addition, atlas creation enables quantification of the variations (standard deviations) of myelin among a healthy population. Ultimately, the created atlas together with estimated variations in population can be used as a reference, for comparing individual patients.

For this work, we used multi-echo  $T_2$  myelin water imaging (MWI) [146, 224] to quantitatively and specifically examine the myelin content in the cervical spinal cord [141]. The MR signal from myelin water, the water trapped between myelin bilayers, can be extracted from the total MR signal based on a characteristic short  $T_2$  relaxation time. The ratio of myelin water signal relative to the total signal is termed myelin water fraction (MWF), which is used as a biomarker for myelin content. The myelin specificity of MWF has been histologically validated in human

brain and spinal cord as well as in animal models. [104, 111, 112, 155] The data collection and analysis required for MWF also provides the geometric mean  $T_2$ , which represents the geometric mean (amplitude-weighted mean on a logarithmic scale) [225] of the  $T_2$  times of the intra- and extra-cellular (IE) water (IEGMT<sub>2</sub>) and is often used as complementary information to the MWF results. It is believed that the IEGMT<sub>2</sub> is influenced by intra- and extra-axonal morphology and environment [49, 159, 216], and in pathology, IEGMT<sub>2</sub> is typically reported to increase, likely due to the presence of extra water from inflammation or edema. [5, 21, 114, 115, 227]

Besides multi-echo  $T_2$  based MWI, a number of other quantitative techniques use fundamentally different approaches to extract MWF and IEWT<sub>2</sub> values. For example, the multicomponent driven equilibrium single pulse observation of  $T_1$  and  $T_2$  (mcDESPOT) method makes use of  $T_1$  weighted and steady state gradient echo acquisitions to estimate  $T_1$  and  $T_2$  times of the tissue components. [44] And the multi-echo gradient echo (mGRE) technique collects  $T_2^*$  decay signals to carry out the MWF. [50] These approaches claim to offer a larger coverage within shorter scanning time, but the data analysis is usually performed under the restricted assumption of a two- or three-pool model and requires estimation of a large number of parameters from a limited amount of data points. Consequently, the accuracy of MWF derived from these techniques (e.g. mcDESPOT and mGRE) is presently an active area of research. [24, 221, 238] Although multi-echo  $T_2$  based MWI has a few limitations such as relatively small coverage, the imaging protocols and post-processing analysis of this method have been well-established over the years and are widely used in numerous studies of myelin quantification, making it an appropriate choice for our study.

The goal of our study was to create multi-echo  $T_2$  derived MWF and IEGMT<sub>2</sub> atlases, by co-registering and averaging MWF and IEGMT<sub>2</sub> maps of the cervical spinal cord from healthy subjects. These two quantitative atlases, with estimated population variations, can serve as normative references of the cervical spinal cord for future studies. We demonstrated the utility of these atlases by applying them to detect pathology in the spinal cords of individual multiple sclerosis patients.

## 3.2 Methods

### 3.2.1 Subject information

Twenty healthy controls (10 male / 10 female; mean age 36 years, range 21–70 years) and 3 participants with relapsing remitting multiple sclerosis (RRMS1: 39 year old male, disease duration: 5 years, Expanded Disability Status Scale, EDSS: 2.5; RRMS2: 42 year old female, disease duration: 4.5 years, EDSS: 0; RRMS3: 37 year old female, disease duration: 7 years, EDSS: 4.0) were recruited. All subjects provided written informed consent with approval from the local ethics board.

### 3.2.2 MRI experiments

Subjects were scanned on a 3.0T Achieva MRI system (Philips, Best, The Netherlands) with a 6 channel phased array spine coil. Cervical cord localizer and sagittal T<sub>2</sub> weighted sequences were followed by (1) axial high-resolution multi-echo fast field echo (mFFE, TE1/ΔTE/TR = 6.6/8.2/815ms, 5 echoes cumulated, field of view (FOV) = 150mm×150mm×44mm, resolution = 0.8mm×0.8mm×2.5mm) for anatomical white and gray matter contrast and (2) a 3D gradient and spin echo (GRASE) T<sub>2</sub> relaxation experiment (excitation flip angle = 90 degrees, 32-echo, TE1/ΔTE/TR = 10/10/1500ms, refocusing flip angle = 180 degrees, 8 axial slices, oversampling = 1.3, gradient mode = maximum, gradient performance = 40mT/m at 200mT/m/ms, fold-over direction = RL, EPI factor = 3, fat suppression = no, pre-saturation band = no, FOV = 180mm×150mm×40mm, acquired resolution = 0.75mm×0.75mm×5mm). The slab was centered at the C2/C3 cord level for all subjects. [141]

### 3.2.3 Myelin water fraction and geometric mean T<sub>2</sub>

Voxel-wise decay curve analysis was performed using regularized non-negative least squares (NNLS) with the extended phase graph algorithm to estimate the refocusing flip angle in each voxel and correcting the T<sub>2</sub> decay curve for stimulated echo artifacts. [176] The regularized NNLS analysis were initialized by using 40 T<sub>2</sub> exponentials logarithmically spaced from 15ms to 2s to fit the decay data.

The misfit  $\chi^2$  is minimized by the following formula:  $\sum_{i=1}^N \left| \sum_{j=1}^M A_{ij} s_j - y_i \right|^2 + \mu \sum_{i=1}^N |s_i|^2$ , where  $N$  represents the total number of data points;  $M$  represents the number of logarithmically spaced  $T_2$  decay times,  $s_i$  represents the amplitude of the  $T_2$  distribution that needs to be solved;  $A_{ij}$  is the kernel matrix for the  $T_2$  exponential decay;  $y_i$  is the measurement data;  $\mu$  is the regularization factor and was chosen to be the largest value that allows a misfit of less than  $1.02\chi^2$  in our analysis. [87, 130, 224] MWF was defined as the fractional signal with  $T_2$  less than 40ms, which was chosen in accordance with previous cervical spinal cord studies using GRASE MWI. [53, 141] IEGMT<sub>2</sub> was the amplitude-weighted mean  $T_2$  time of the intra- and extra- cellular water compartment and was calculated by the following formula:  $\frac{\sum_{i=1}^M s_i \times T_i}{\sum_{i=1}^M s_i}$ , where  $M$  is the total number of  $T_2$  components logarithmically spaced between 40 – 200ms;  $T_i$  is the  $T_2$  time of the  $i^{\text{th}}$  component; and  $s_i$  is the amplitude of the  $i^{\text{th}}$  component. Voxel-wise MWF and IEGMT<sub>2</sub> maps were used for subsequent analysis. The NNLS analysis code can be requested from: <https://mriresearch.med.ubc.ca/news-projects/myelin-water-fraction/>.

### 3.2.4 Myelin water fraction atlas and geometric mean $T_2$ atlases

For creation of  $T_2$  relaxation metric atlases, individual MWF and IEGMT<sub>2</sub> maps were co-registered to a common template space. We used the Spinal Cord Toolbox (SCT) [41] for image post-processing and the PAM50 template [128] as the common space for atlas creation. A registration framework based on individual’s white matter morphology was developed for atlas creation:

- (1) The anatomical mFFE image was registered to GRASE space by an affine transformation;
- (2) A gray matter mask was manually drawn on each slice of the registered mFFE image;
- (3) A white matter mask was calculated by subtracting the manual grey matter segmentation from the whole cord mask (obtained using the SCT propseg tool);
- (4) The white matter mask was registered to the PAM50 white matter template using a nonlinear transformation (a combination of center of mass rotation,

affine, symmetric normalization, and bsplinesyn algorithms) to obtain the warping function which transforms individual GRASE images to the template space;

- (5) The acquired warping function was applied to individual MWF and IEGMT<sub>2</sub> maps to obtain the registered MWF and IEGMT<sub>2</sub> maps in template space. Registered images were visually inspected.

The atlases were then created by averaging the co-registered MWF and IEGMT<sub>2</sub> maps from all individual subjects in the template space. The voxel-wise standard deviation (SD) of each atlas was subsequently calculated to assess the variations of MWF and IEGMT<sub>2</sub> in this healthy population.

### **3.2.5 Z-score maps for RRMS subjects**

To illustrate the utility of the created atlases in disease, voxel-wise z-score map of 3 RRMS subjects were calculated as  $z = \frac{x-\mu}{\sigma}$ , where  $x$  is the individual measurements of MWF or IEGMT<sub>2</sub> maps registered in the template space,  $\mu$  is MWF or IEGMT<sub>2</sub> atlas (the mean), and  $\sigma$  is the standard deviation (SD) of the atlas. Regions with coefficient of variation (COV: SD divided by mean) larger than 0.75 were excluded. [101] Z-score map images were visually inspected to mimic typical clinical review for abnormalities, to illustrate how the atlases can be used to detect abnormalities in individual patients. In addition, significant differences were defined as  $z < -1.96$  or  $z > 1.96$ .

## **3.3 Results**

### **3.3.1 Myelin water fraction atlas and geometric mean T<sub>2</sub> atlas**

Figure 3.1 shows representative slices of the resulting MWF atlas and IEGMT<sub>2</sub> atlas as well as their SD maps at C2, C2/C3, and C3 levels. Visual inspection of the atlas maps demonstrates that distinct regions are easily identifiable, especially in the MWF atlas. More dramatic variations along the cord from C2 to C3 were observed in the MWF atlas compared to the IEGMT<sub>2</sub> atlas. The SD of the MWF atlas was homogenous (Figure 3.1) over the cross-sectional area of the whole cord,

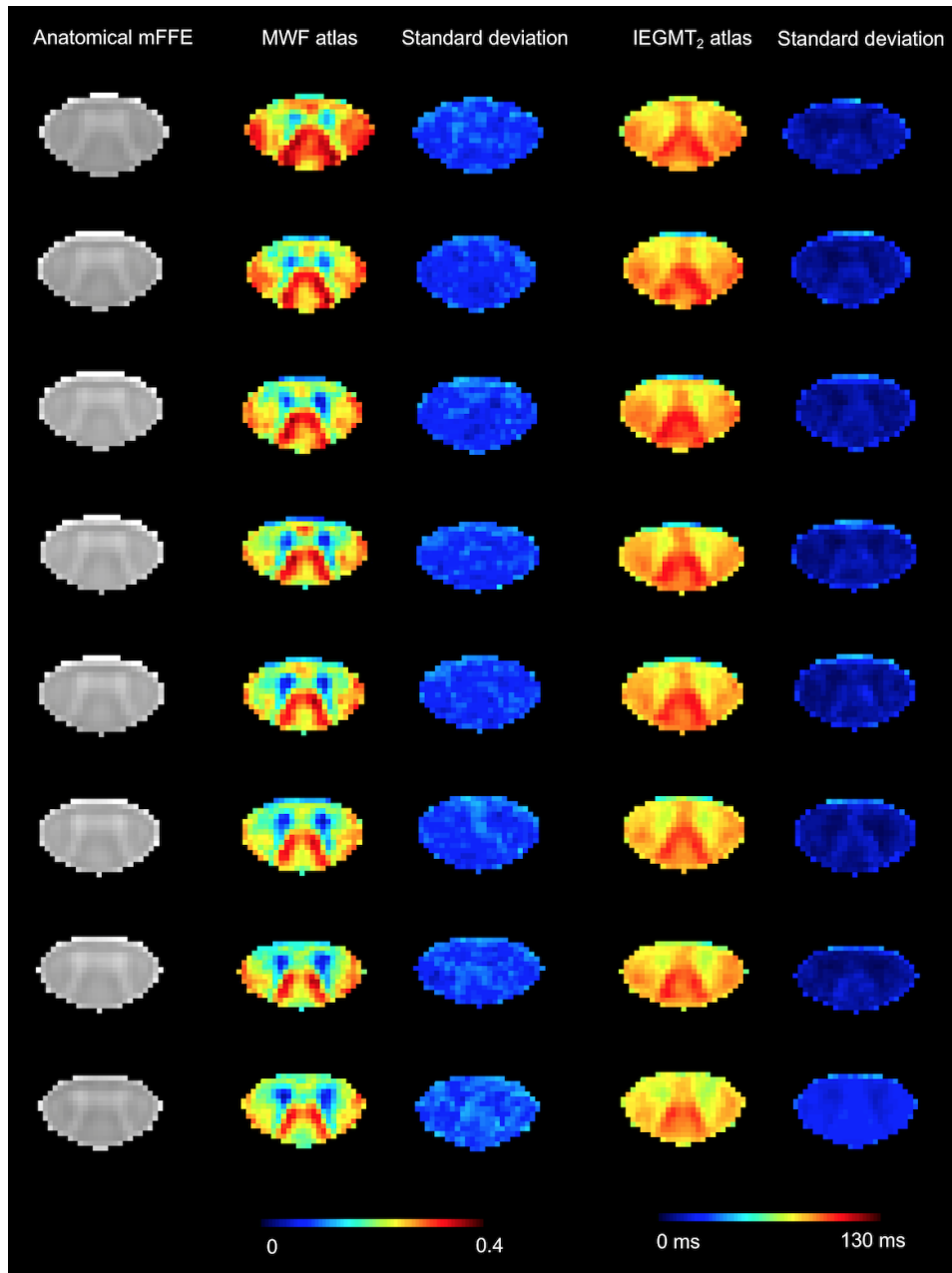


**Figure 3.1: MWF atlas and IEGMT<sub>2</sub> atlas.** The resulting myelin water fraction (MWF) atlas and geometric mean T<sub>2</sub> (IEGMT<sub>2</sub>) atlas of all 8 slices from C2 to C3. Averaged anatomical images (mFFE) are also displayed.

whilst the SD of IEGMT<sub>2</sub> atlas showed slight gray and white matter contrast.

### 3.3.2 Z-score maps for RRMS participants

To demonstrate the utility of the atlases, anatomical mFFE, MWF and IEGMT<sub>2</sub> z-score maps from 3 RRMS participants are presented in sagittal, coronal and axial view (Figure 3.2). Noisy individual MWF and IEGMT<sub>2</sub> maps may introduce false positive points so thresholded maps ( $z < -1.96$  or  $z > 1.96$ ) are also displayed to show regions with significant differences compared to the atlases. In the MWF z-score maps (Figure 3.2A), three subjects showed distinct characteristics in MWF z-scores. Significant myelin water signal reductions ( $z < -1.96$ ) were found in the lesions of RRMS subject 1 and 2. Particularly for RRMS subject 1, low MWF z-scores within the dorsal column regions across the entire C2 and C3 segment were also observed on the averaged axial slice. Subject 2 and 3 showed a lower degree of abnormalities in the axial averaged MWF z-score map. IEGMT<sub>2</sub> z-score maps (Figure 3.2B) showed no evidence of large changes in the averaged IEGMT<sub>2</sub> for any subject. Interestingly, IEGMT<sub>2</sub> was increased slightly in the lesion of RRMS subject 1 but not in the lesion of RRMS subject 2.

## 3.4 Discussion

Although MWI is a robust method for myelin content quantification, and a good scan-rescan reproducibility has previously been reported [141], MWF values of healthy individuals can vary due to many factors (e.g. normal population variation, factors affecting data quality and complexity of post-processing analysis), making the image quality of individual spinal cord MWF maps less than ideal. The idea of creating a MWF atlas takes advantage of the fact that averaging a large number of samples can minimize random noise and improve signal to noise ratio. Indeed, the resulting MWF and IEGMT<sub>2</sub> atlases demonstrated much improved image quality compared to individual metric maps (Figure 3.3). However, we have to point out that MWF and IEGMT<sub>2</sub> values are also dependent on factors regarding experiment protocol and data analysis. Following the same experimental and post-processing parameters aforementioned in the Methods is thus important when utilizing our atlases.

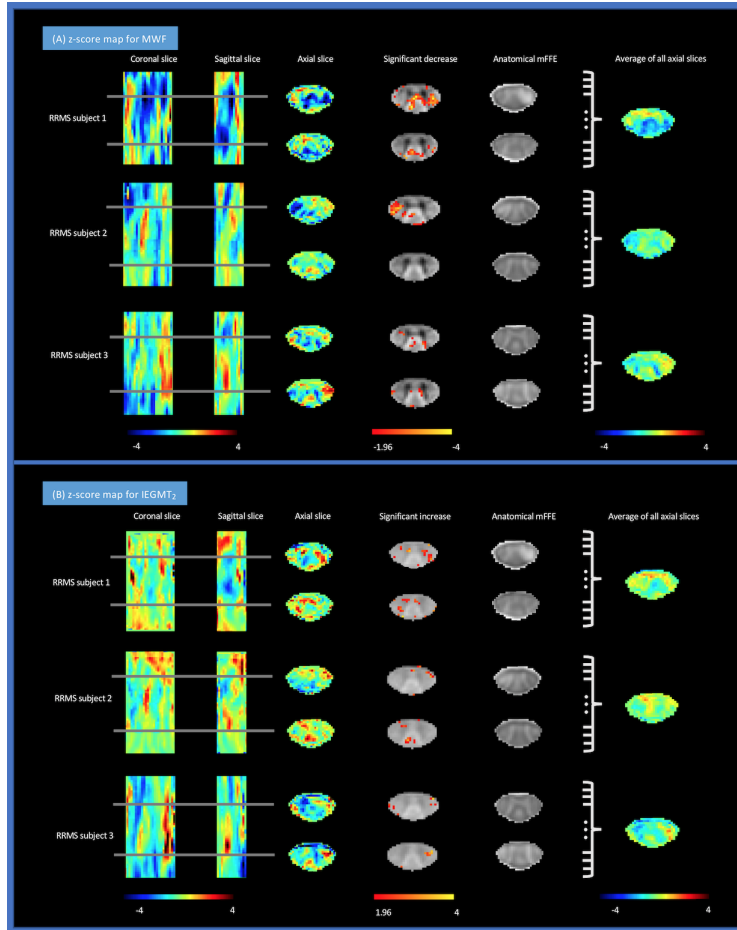


**Figure 3.2: Comparison of z-score maps from 3 relapsing remitting multiple sclerosis (RRMS) subjects.** Z-score maps were calculated based on myelin water fraction (MWF) and  $T_2$  times of the intra- and extracellular (IE) water (IEGMT<sub>2</sub>) atlases and their standard deviation for C2 to C3 cord and representative slices are presented in sagittal, coronal, and axial view. Sagittal and coronal views are showing at the middle of the cord, and axial view are showing at C2 and C3 levels. Axial slices are also thresholded for regions of significance ( $z < -1.96$  or  $z > 1.96$ ) and displayed on MWF and IEGMT<sub>2</sub> atlases respectively. An average of all 50 axial z-score maps is also shown for each participant. Axial anatomical multi-echo fast field echo (mFFE) images are shown to compare with the z score maps at different levels.

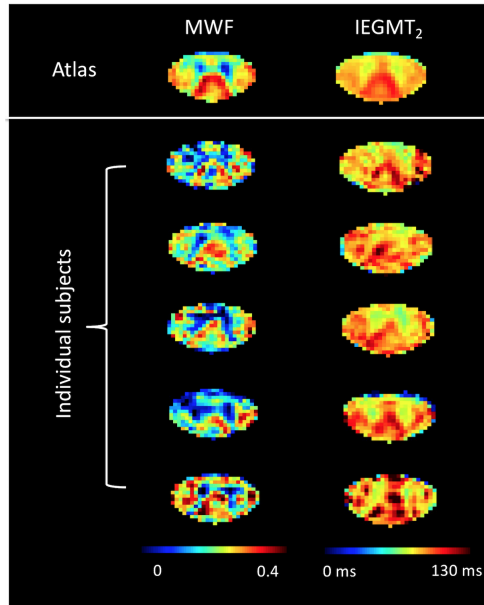


**Figure 3.3: Compare MWF and IEGMT<sub>2</sub> atlases with individual metric maps.** In this illustrative example, the created atlases showed much better image quality and contrast between structures compared to individual myelin water fraction (MWF) and geometric mean T<sub>2</sub> (IEGMT<sub>2</sub>) maps of 5 subjects. All slices are shown at the same level.

The MWF atlas accurately represents well-known myelin anatomical characteristics. [51, 75, 191] Anatomical features of the cord such as the butterfly shaped gray matter, dorsal columns, and several lateral and ventral pathways are clearly depicted on the atlas ((Figure 3.1)), supporting the usefulness of the atlas as an in-vivo myelin reference in the spinal cord. Recent studies [52, 132] using proton density imaging to estimate the macromolecular tissue volume (MTV) found similar variations between different spinal cord regions. Also from those studies, average maps based on diffusion and MT metrics exhibited different regional variations in the cord, indicating that enriched tissue properties (such as axon diameter, myelin thickness, and water mobility etc.) can be probed and monitored differently. It seems that using any single quantitative imaging method alone may only provide one aspect of tissue properties and a combination of different techniques may offer a better understanding of axonal morphology and myelin integrity. It is also inter-

esting to observe that, within only two vertebral levels of the cervical cord that we imaged, the atlas shows distinct regional variation patterns (Figure 3.1) from C2 to C3, revealing how much the myelin may change through the cord even over a small distance. The changes of myelin along the cord is supported by Minty *et al.* who, using a single slice sagittal acquisition at 1.5T, observed variation from C2 to C3, as well as along the rest of the spinal cord. [162]

In contrast, the IEGMT<sub>2</sub> atlas shows minimal variation along the cord from C2 to C3, indicating that IEGMT<sub>2</sub> offers additional and different information about the cord tissue morphology. Although it is more homogeneous compared with the MWF atlas, the IEGMT<sub>2</sub> atlas still shows good contrast and many spinal cord regions can still be differentiated. Histological validation for axonal diameter and density will be needed for further interpretations of IEGMT<sub>2</sub> results.

Z-score map (Figure 3.2) of an individual subject provides a useful statistical parameter and is one of the potential applications of the MWF and IEGMT<sub>2</sub> atlases. Z-score maps can detect true abnormalities by accounting for normal tissue variations within healthy populations, and have been successful in brain imaging applications. [102] Our representative examples from 3 RRMS subjects show that the severity and location of demyelination and alterations in intra/extracellular water mobility in the cord can be clearly visualized in the resulting z-score maps. One may also notice that a few small highlighted regions in the z-score map do not correspond to lesions, which confounds the interpretation of the z-score maps. Such discrepancy is probably resulting from the high variations in individual MWF and IEGMT<sub>2</sub> values due to noise and NNLS instability. A potential solution is to incorporate nonlocal regularization filters [23, 233] into the current analysis pipeline to denoise the GRASE images. However, these nonlocal regularization methods have only been validated for the brain imaging data so the feasibility in the spinal cord needs further investigation. In summary, the z-score map is a straightforward way to make use of T<sub>2</sub> metric atlases as a reference to visualize the pathology in individual subjects.

A number of limitations warrant consideration. First, at the moment, only the cervical cord is accessible for good quality data acquisition using MWI. But for many diseases and injuries, spinal cord pathology can occur also as well as only in thoracic regions. However, more artefacts are generated due to technical difficulties

regarding more cord motion near the lungs and heart, larger imaging volume, and more main field inhomogeneity, making investigations at the thoracic level very challenging. Particularly, the reduction of MWI accessibility below C7 is largely due to the fact that the imaging field of view has to be substantially increased to prevent any phase wrapping from the shoulder, leading to an impractical scanning time if the same resolution is preserved. The challenges are common issues for all quantitative MR techniques in the spinal cord. Second, although automatic registration and segmentation by SCT can exclude human bias, the quality of these image processing steps still needs further validation, given the fact that the spinal cord is so small that any misalignment in cord registration may alter the results of small regions within the cord. Thirdly, the atlas is generated from a limited number of healthy subjects. As age has been reported as a significant factor in spinal cord MWF measurement (lower MWF in older adults) in a previous study [147], it would be important to follow-up the present study by recruiting a much larger number of healthy subjects spanning all ages to enable creation of a more extensive atlas for specific age and sex groups. Finally, a few other conditions such as edema or inflammation could also lead to a decrease in MWF values and complicate the interpretation of MWF reduction. Although ex-vivo imaging and histological validation [111] suggests a linear relationship between MWF and myelin specific stains such as Luxol Fast Blue (LFB), the total water content is still a confounding factor for in-vivo imaging. Previously, a model created to interpret experimental studies in MS brains [116] found that the increase in water content needed to yield the substantial reductions in MWF observed would require a volume of water that would lead to physiologically unrealistic tissue swelling. Nevertheless, a measurement of the total water content [160, 218] in addition to MWI would be certainly helpful to discriminate myelin loss from other influencing conditions.

### **3.5 Conclusion**

In conclusion, we have created an in-vivo normative atlas of quantitative  $T_2$  relaxation metrics for the spinal cord. The MWF atlas characterizes myelin content in distinct regions while the IEGMT<sub>2</sub> atlas provides information about intra and extracellular water mobility. Both atlases can be used as a reference for other in vivo

spinal cord studies that assess demyelination and other pathologies like inflammation which may impact IEGMT<sub>2</sub> of individual patients (URL: <https://sourceforge.net/projects/mwi-spinal-cord-atlases/>), an important step towards the ultimate goal of clinical implementation and use of quantitative T<sub>2</sub> relaxation imaging.

## Chapter 4

# Myelin water atlas for the brain at 3T MRI\*

### 4.1 Introduction

Myelin, the protective sheath around axons, enables saltatory conduction in the central nervous system. It is posited that myelin damage over time drives the severity and progression of many brain and spinal cord neurodegenerative diseases [69]. In-vivo information about myelin content is highly desirable to personalize monitoring of individual patients, and could offer valuable clinical insight regarding illness stage and treatment efficacy. Several quantitative magnetic resonance imaging (MRI) techniques have been developed based on the physics of diffusion [202, 203], magnetization transfer (MT) [189, 198] and  $T_2$  relaxation [146, 224], to monitor changes in myelination [113]. Clinical use of these techniques on an individual patient level remains challenging for several reasons. Beyond multi-vendor sequence standardization and implementation hurdles, interpreting individual patient imaging outcomes is difficult as myelin content varies with age [69], years of education [70] and possibly sex. In addition, while group comparisons between

---

\*A version of this chapter has been published. Liu H, Rubino C, Dvorak AV, Jarrett M, Ljungberg E, Vavasour IM, Lee LE, Kolind SH, MacMillan EL, Traboulsee A, Lang DJ, Rauscher A, Li DKB, MacKay AL, Boyd LA, Kramer JL, Laule C. Myelin Water Atlas: A Template for Myelin Distribution in the Brain. *Journal of Neuroimaging*. 2019 Nov;29(6):699-706.

disease and control cohorts often detect differences in myelin [116, 196], interpretations on an individual level of these quantitative myelin imaging methods are not as common. [35, 131, 149] Both the measurement noise and the natural population variability present challenges. The former can be assessed by the inter-/intra-session reproducibility [127, 161] but the latter is seldom investigated. Finally, collecting healthy volunteer data for every study is costly, diverting funds from acquiring more data from patients, and in the clinical setting, it would be procedurally difficult and prohibitively expensive to obtain matched healthy volunteer data for individual patients. In summary, normative data is key for determining abnormalities in myelin in neurological disease. Development of a normative myelin imaging atlas, to which individual patients can be compared, can address these challenges. Atlas-based approaches for MR methods influenced by myelin have been implemented for a number of different quantitative imaging techniques, including diffusion,  $T_1$ ,  $T_2$ , magnetization transfer and mcDESPOT-derived myelin water assessment. [8, 14, 65, 101, 192, 213]

In our study, we used myelin water imaging (MWI) [112], which measures the fraction of the signal from water trapped in myelin bilayers using quantitative multi-echo assessment of  $T_2$  relaxation. The fraction of the myelin water signal relative to total signal, defined as the myelin water fraction (MWF), is an in-vivo marker of myelin. The specificity of MWF as a myelin biomarker has been validated histologically [111, 112] and MWI has been extensively studied in many diseases involving myelin deficits, (e.g. multiple sclerosis (MS), neuromyelitis optica spectrum disorder, schizophrenia, phenylketonuria, autism, Niemann-Pick disease, amyotrophic and primary lateral sclerosis, Krabbe disease, cervical spondylotic myelopathy, stroke, concussion). [21, 40, 45, 66, 91, 110, 116–118, 138, 151, 196, 215, 217, 229] Our objective was to make an atlas specific to normal myelin content in the brain to serve as a myelin reference for healthy adults by co-registering and averaging MWF maps from a large number of healthy participants. The resulting atlas and its standard deviation depict the population mean and variability of myelin content throughout the brain.

## 4.2 Methods

### 4.2.1 Participants and MR Experiments

50 healthy individuals (25 males / 25 females, mean age 25 years, range: 17-42 years) and 3 women with relapsing remitting MS (MS1: 25 years old, disease duration: 4 months, Expanded Disability Status Scale (EDSS): 0; MS2: 26 years old, disease duration: 7 years; EDSS: 2.0; MS3: 26 years old, disease duration: 8 years, EDSS: 2.0) were scanned at 3T using an 8-channel phased-array head coil (Achieva, Philips, Best, The Netherlands). MR data included myelin water imaging (3D gradient and spin echo (GRASE) [177], 32 echoes, TE/TR = 10/1000ms,  $\Delta TE = 10$ ms, axial matrix size =  $232 \times 192$ , slice oversampling factor = 1.3, SENSE = 2, 20 acquired slices at  $0.99 \times 0.99 \times 5$ mm<sup>3</sup>, reconstructed to 40 slices at  $1 \times 1 \times 2.5$ mm<sup>3</sup>, acquisition time = 14.4 min) and a 3DT<sub>1</sub> whole brain volumetric anatomical sequence (fast gradient echo, flip angle = 6°, TE/TR = 3.7/7.4ms, slices = 160, acquisition and reconstruction resolution =  $1 \times 1 \times 1$ mm<sup>3</sup>).

### 4.2.2 Data Analysis

Data analysis of voxel-wise 32-echo T<sub>2</sub> decay curves acquired with the GRASE sequence was performed by regularized non-negative least squares (NNLS, in-house MATLAB software, can be requested from: <https://mriresearch.med.ubc.ca/news-projects/myelin-water-fraction/>) algorithm to generate MWF maps. [176] This analysis employed the extended phase graph algorithm to estimate the refocusing flip angle in each voxel and accounted for stimulated echo artifact when fitting the T<sub>2</sub> decay curves. [176] MWF was defined as the fractional signal with T<sub>2</sub> < 40ms.

To create the myelin water atlas, individual 3DT<sub>1</sub> brain extracted images were first registered to the standard 1mm MNI152 space (nonlinear, >12 degrees of freedom (DOF)) using FSL [201] to obtain the warping fields from individual space to standard space. Then, individual MWF maps were registered to 3DT<sub>1</sub> images (rigid, 6 DOF, warp function acquired from registering GRASE to 3DT<sub>1</sub>) and subsequently registered to the standard space by applying the previously obtained warping fields with linear interpolation. Registration accuracy was visually

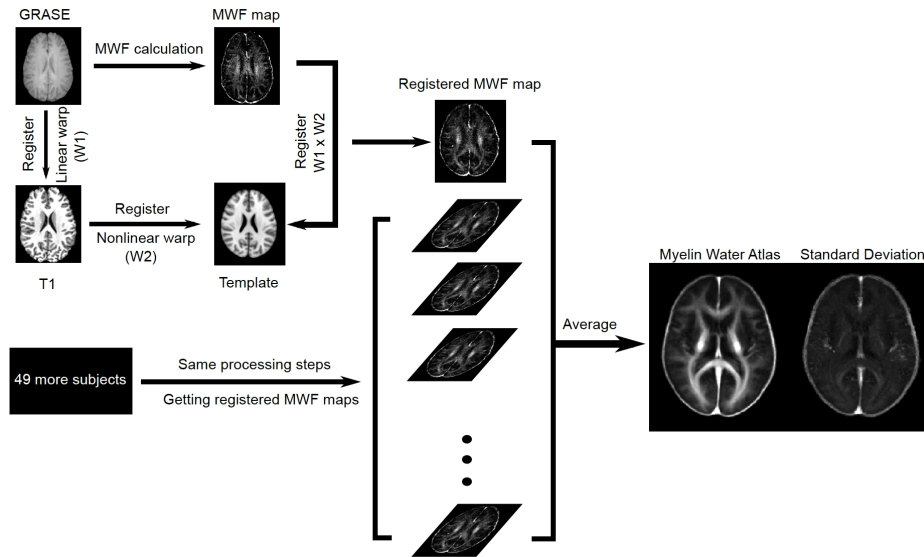


**Figure 4.1: Workflow chart.** Myelin water fraction (MWF) map of each individual subject was registered to standard space of MNI152 T<sub>1</sub> 1 mm brain. A myelin water atlas was created by averaging all registered MWF maps from the 50 healthy participants.

confirmed at each step. If the registration failed the visual inspection, FNIRT initialization parameters would be adjusted to allow more registration deformation. This process went on until the registration results passed visual inspection (e.g. matching the ventricles). The myelin water atlas was created by averaging the aligned MWF maps in the standard MNI space from all healthy participants and voxel-wise standard deviation was also derived (Figure 4.1). In addition, voxel-wise normality test (Shapiro-Wilks) was performed for all registered MWF maps in the standard MNI space.

For all healthy participants, average MWF was extracted from 8 commonly reported regions of interest (ROIs) in previous MWI studies [136, 146]: internal capsule anterior and posterior limbs (left-right combined), splenium, genu and body of corpus callosum, forceps major, forceps minor, and total white matter. All ROIs were taken from the JHU (Johns Hopkins University) DTI-based white matter atlas. [58] Paired t-tests were performed on mean MWF values between ROIs, and

independent t-tests compared MWF between males and females (voxel-wise and ROI). Bonferroni correction was applied for multiple comparisons. Normality test (Shapiro-Wilk) was also performed for all ROIs.

Voxel-wise z-score maps were calculated for the three MS participants using  $z = \frac{x-\mu}{\sigma}$ , where  $x$  is the individual measurements of MWF registered in the template space,  $\mu$  is myelin water atlas (the mean), and  $\sigma$  is the standard deviation (SD) of the atlas. Significant reduction in MWF was defined as  $z < -1.96$ . Regions with coefficient of variation (COV: SD divided by mean) larger than 0.75 were excluded because high COV is more likely produced by registration misalignment.

### 4.3 Results

Four representative axial slices from the resulting myelin water atlas (in greyscale and colour schemes), the corresponding SD maps, the voxel-wise normality test (p-value), and the voxel-wise t-test (p-value) between males and females are shown in Figure 4.2. The map of normality test demonstrates most white matter voxels (88%) in the standard MNI space have a normal distribution (W-stats:  $p > 0.05$ ) of MWF values from all 50 study participants. The map of t-test illustrates almost all white matter voxels (94%) have no significant sex differences ( $p > 0.05$ ) in MWF for a voxel-wise comparison. Table 4.1 summarizes the MWF atlas average and SD values from each ROI, highlighting the regional variation of MWF. For example, mean MWF was 63% higher in the posterior vs. anterior limb of internal capsule, 42% higher in the splenium than the genu, and 54% higher in the forceps major than the forceps minor. No significant differences ( $p > 0.05$ ) were found between male and female MWF for all ROIs and no significant correlations ( $p > 0.05$ ) between MWF and age were observed for any ROI. Results of Shapiro-Wilk normality test for mean MWF in all ROIs are also presented in Table 4.1 (all  $W > 0.97$ ,  $p > 0.05$ ).

Figure 4.3 shows box plots of individual MWF values from different ROIs from each healthy participant. Each line connects the MWF data points of the same participant to trace MWF variations in different regions in an individual. Most participants followed a similar pattern. MWF between ROIs significantly varied (one-way ANOVA, between groups:  $F(6,343)=185.94$ ,  $p < 10^{-20}$ ). Table 4.2

**Table 4.1: Summary of myelin water fraction (MWF) in different regions of interest in white matter for all subjects, and males and females separately.** P-value indicates comparison between male and female participants. All regions of interest (ROI) from 50 participants are tested for normality (Shapiro-Wilk W statistics).

ROI (# of voxels)	MWF			Male vs. Female: p-value	Shapiro- Wilk test: W (p-value)
	All subjects (n=50)	Males (n=25)	Females (n=25)		
Total white matter (129495)	0.101×0.014	0.101×0.014	0.100×0.013	0.781	0.98 (0.71)
Internal capsule posterior limb (4413)	0.178×0.021	0.179×0.022	0.178×0.019	0.857	0.99 (0.94)
Internal capsule anterior limb (2548)	0.109×0.020	0.107×0.020	0.111×0.019	0.492	0.98 (0.44)
Corpus callosum splenium (5286)	0.141×0.017	0.137×0.017	0.144×0.017	0.171	0.98 (0.48)
Corpus callosum genu (3835)	0.099×0.017	0.098×0.019	0.099×0.015	0.832	0.97 (0.33)
Corpus callosum body (13711)	0.084×0.015	0.084×0.017	0.085×0.013	0.669	0.98 (0.78)
Forceps major (4546)	0.144×0.017	0.143×0.014	0.144×0.019	0.943	0.97 (0.33)
Forceps minor (1285)	0.093×0.017	0.092×0.019	0.095×0.015	0.599	0.99 (0.89)

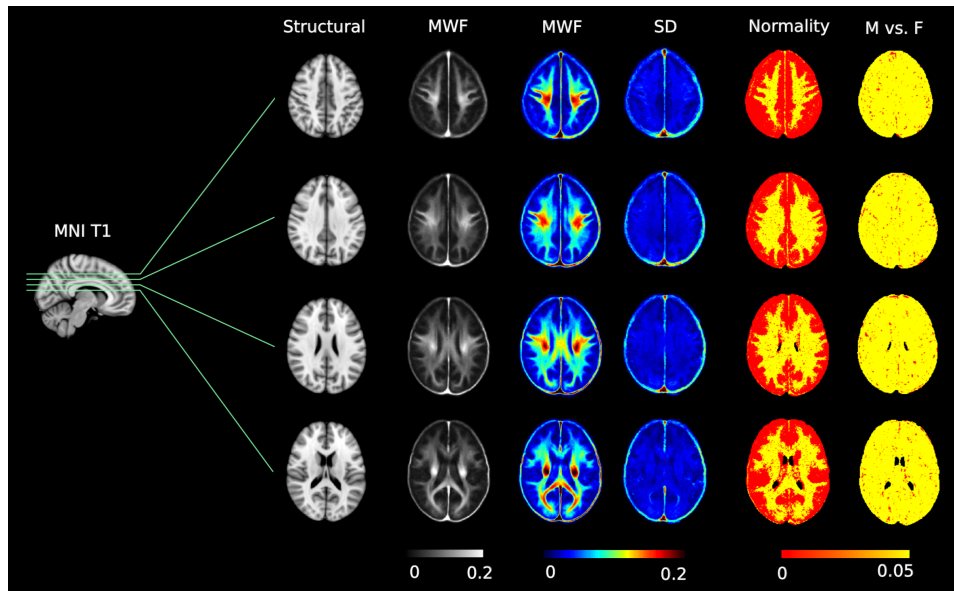


**Figure 4.2: Myelin water atlas.** Four representative axial slices of myelin water fraction (MWF) from the resulting myelin water atlas (in grayscale and colormap [color scale: 0 – 0.2]), the corresponding SD maps, the voxel-wise normality test P-value (color scale: 0 – 0.05), and the voxel-wise P-value (color scale: 0 – 0.05) of t-test between males and females MWF are shown and compared to a  $T_1$  structural 1 mm brain (MNI152).

summarizes pairwise comparisons of MWF values between different ROIs.

Figure 4.4 illustrates examples of using the myelin water atlas to create voxel-wise z-score maps to visualize demyelination. All 3 MS participants had lesions on conventional  $T_2$ -weighted imaging. MS1 did not demonstrate any myelin abnormalities. MS2 and MS3 show myelin loss in focal lesions, as well as significant myelin reductions in normal appearing white matter, mainly around the forceps major.

## 4.4 Discussion

The creation of a myelin water atlas takes advantage of averaging a large number of samples to minimize random noise and improve signal to noise ratio. As a result, our myelin water atlas (Figure 4.2) constructed from 50 healthy adults ex-

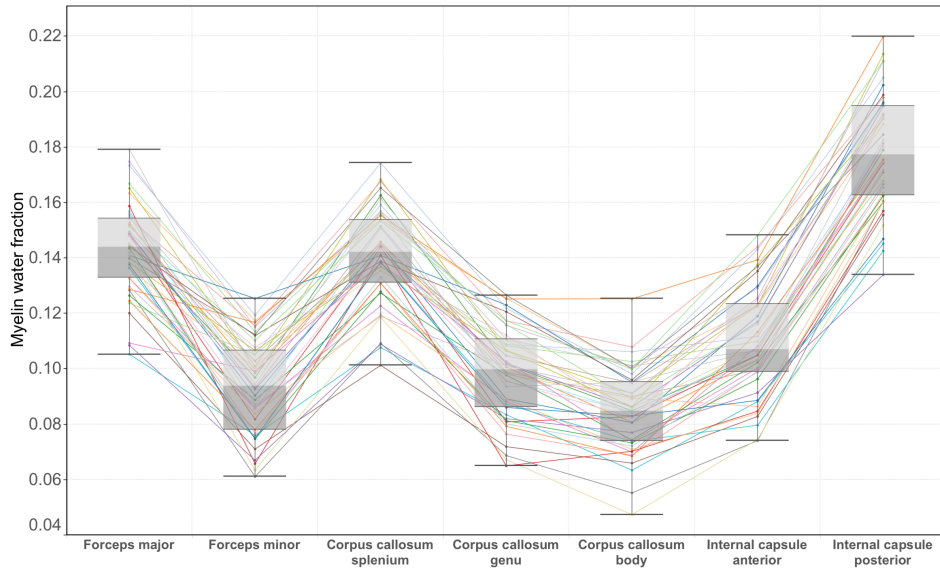


**Figure 4.3: Myelin water fraction of different regions of interest (ROIs) in white matter in healthy participants.** The box plot shows the myelin water fraction (MWF) in forceps major, forceps minor, corpus callosum splenium, corpus callosum genu, corpus callosum body, anterior limb of internal capsule, and posterior limb of internal capsule for 50 healthy adults. Each line is connecting the data points from the same participant to trace the MWF variations in different ROIs across an individual. Similar patterns of variation between regions were present for all participants.

hibited high contrast between white and grey matter as well as regional variations within white matter. Regional MWF variability is a visually observable feature portrayed in the atlas, likely due to the varying myelin composition in different brain regions. The atlas confirmed well-known microstructure features of the brain [2, 187, 206], such as the corpus callosum being highly myelinated compared to frontal white matter, and with regional differences observed within the corpus callosum itself like the splenium having more myelin than the genu. Further evidence of differences in regional myelin concentrations is provided by biochemical and histological analysis of myelin specific proteins proteolipid protein (PLP), myelin basic protein (MBP) and 2',3'-cyclic 3' phosphohydroxylase (CNP) in human tissue

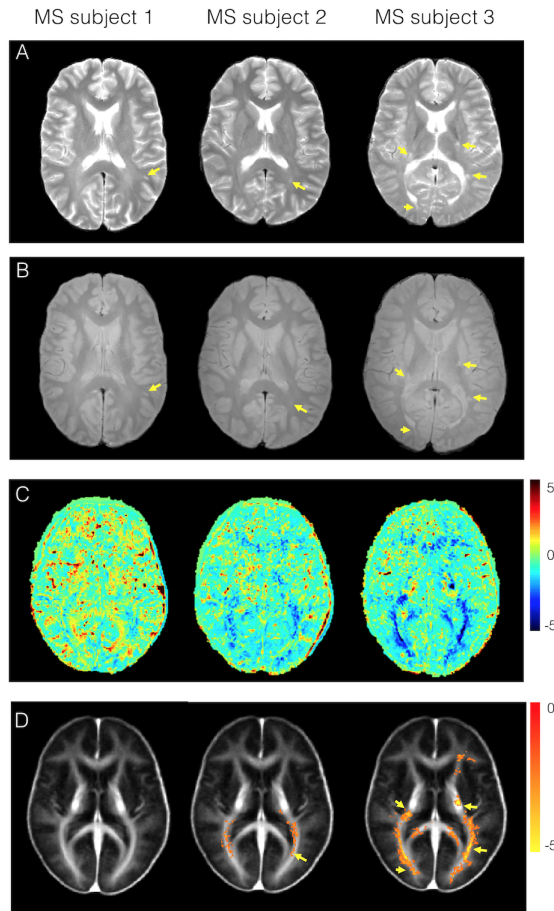


**Figure 4.4: Z-score maps for three individuals with multiple sclerosis.** (A) T<sub>2</sub>-weighted images in individual space of three relapsing remitting multiple sclerosis (MS) participants with lesions indicated by arrows; (B) proton density weighted images in individual space; (C) corresponding z-score maps (color scale: -5 to 5); and (D) z-score maps thresholded for significant reduction ( $z < -1.96$ , uncorrelated, color scale: -5 to 0). Regions with coefficient of variation (mean divided by standard deviation) larger than 0.75 were excluded. MS subject 1 was a 25-year-old female with expanded disability status score (EDSS) = 0. MS subjects 2 and 3 were 26-year-old females with EDSS = 2.0. MS subject 3 demonstrates the most extensive global demyelination.

**Table 4.2: Pairwise comparisons (paired t-test) of myelin water fraction (MWF) between 7 white matter regions in healthy subjects.** Bonferroni correction (significant level:  $p < 0.002$ ) was used to corrected for multiple comparisons.

MWF Paired t-test	Forceps minor	Corpus callosum splenium	Corpus callosum genu	Corpus callosum body	Internal capsule anterior	Internal capsule posterior
Forceps major	$< 10^{-22}$	0.172	$< 10^{-19}$	$< 10^{-26}$	$< 10^{-14}$	$< 10^{-14}$
Forceps minor	x	$< 10^{-27}$	$< 10^{-8}$	$< 10^{-6}$	$< 10^{-11}$	$< 10^{-36}$
Corpus callosum splenium	x	x	$< 10^{-24}$	$< 10^{-32}$	$< 10^{-16}$	$< 10^{-18}$
Corpus callosum genu	x	x	x	$< 10^{-13}$	$< 10^{-6}$	$< 10^{-35}$
Corpus callosum body	x	x	x	x	$< 10^{-6}$	$< 10^{-37}$
Internal capsule anterior	x	x	x	x	x	$< 10^{-38}$

[11, 77, 96, 212], which support our observations with the created myelin water atlas, for example higher levels of PLP and CNP in areas akin to forceps major compared to forceps minor. In addition, the SD maps of the atlas provide an estimation of myelin variation among people. Although the SD maps appear mostly homogenous, features of some brain structure still emerge, which may imply that, in the healthy population, some brain regions may exhibit more variance in myelin content than others. Taking regional differences and variation into consideration is important when assessing neurological conditions that affect myelin.

To demonstrate the generality of our 50 healthy study participants, Shapiro-Wilk normality tests were performed and no deviations from a normal distribution of MWF were found for all ROIs. In addition, no obvious patterns within white matter were observed in the normality map (Figure 4.2), revealing our data repre-

sent a good sampling of the population even in a voxel-wise standard. We observed similar patterns of MWF variability across different ROIs in almost all participants (Figure 4.3). The highly significant paired t-tests (Table 4.2) and the consistent patterns of myelin variation between structures (Figure 4.3) illustrate that MWF can assess subtle differences of myelin microstructure at an individual level, expanding upon previous work which reported group averages from smaller cohorts. [14, 65, 116, 161] Although other quantitative metrics (i.e. magnetization transfer ratio [166, 197] derived from MT experiments and fractional anisotropy [164, 235] by diffusion techniques) also detect differences within different white matter ROIs, those observed differences may be influenced by non-myelin related factors such as extracellular water, fiber orientation and axonal diameter. In contrast, MWI, a histologically validated marker for myelin [103, 111, 112, 119], is proposed to be more specific than other techniques. [113] However, water exchange between myelin water and intra-/extra- cellular water may affect MWI measurements and is currently an active area of research. [214]

One potential usage of the myelin water atlas is voxel-wise z-score mapping. The z-score describes how many SDs a measurement is above or below the mean, and is a valuable statistical parameter to test occurring probability of an abnormality within a normal distribution. Based on the atlas that represents a population mean and its SD map that evaluates natural variations in that population, voxel-wise z-score maps for individual participants can be carried out to detect true abnormalities while accounting for myelin variation in nature. Although voxel-wise calculations can be sometimes affected by registration errors as well as random noise, thresholding for COV can be applied to help mitigate these effects. In our illustrative example (Figure 4.4), the 3 female participants with relapsing remitting MS displayed unique intensity and spatial characteristic in their z-score maps, revealing different severities and distributions of myelin reduction in their brains.

Several limitations exist for the current study and future use of the myelin water atlas: (1) The current myelin water atlas is only suitable for comparing MWI data from young adults. Myelination in adults may correlate with factors such as age [69], and may be influenced by factors like body mass index (BMI) [72, 107, 108] and years of education [70]. However, most of our current study participants (~75%) are in a narrow age range of 20-30 years, making it difficult to reliably

examine the MWF correlation with age. BMI and years of education were also not controlled for as this data was not available. (2) Data from the exact GRASE sequence used in this study is optimal to utilize the myelin water atlas. Comparing MWF acquired by different sequence parameters (e.g. 48-echo GRASE with shorter inter-echo spacing) or other sequences is possible in a qualitative way but not recommended for quantitative purposes. There is evidence that not all myelin water imaging sequences produce the same results. [237, 238] The impact on the MWF values acquired by different sequence parameters remains an active area of investigation. (3) The NNLS algorithm for MWF calculation is susceptible to noise, resulting in large variability within all ROIs. Strong regularization and spatial smoothing is often employed to enhance the output image. MWF values extracted from small regions should be interpreted with caution. (4) The cutoff time of 40 ms for myelin water in the brain may not be ideal for all white matter structures as the  $T_2$  times of myelin water and IE water might be region dependent, as suggested by a previous study. [190] (5) The accuracy of image registration is critical for successful atlas creation. While all data registration was visually inspected in our study, data extrapolation from individual space to the template space by the current FSL-based registration technique may be not ideal, especially when an individual's brain morphology is very different from the template, such as someone with larger ventricles. Outlines of brain features in the SD map could also potentially be an indication of registration error. (6) Finally, a larger number of participants would also improve atlas accuracy. To address these challenges, future studies should focus on collecting data from all age groups as well as controlling for years of education, developing a more stable algorithm for MWF calculation, and applying more sophisticated software for image registration post-processing.

## 4.5 Conclusion

In conclusion, MWI detects subtle differences of myelin content in key regions in individual white matter. Our myelin water atlas created in the current study depicts the normative information of healthy myelin in the human brain and evaluates myelin variations in the population. The atlas ([url:https://sourceforge.net/projects/myelin-water-atlas/](https://sourceforge.net/projects/myelin-water-atlas/)) can be used as a reference for other in-vivo studies of

myelin, and to visually demonstrate areas of demyelination in the individual subject, an important step in the ultimate goal of clinical implementation of myelin water imaging.

However, the atlas approach for the individual use of MWI illustrated in this chapter and Chapter 3 is still limited since the MWI data analysis algorithm NNLS has apparent defects, including the lengthy processing time and the reliability issues of the calculation results. In the next two chapters, these remaining challenges will be subsequently addressed.

## Chapter 5

# Acceleration of myelin water imaging data analysis via neural network algorithm\*

### 5.1 Introduction

Myelin water, the water trapped in myelin bilayers, can be used as a myelin biomarker. [224] Myelin water imaging (MWI) [146, 224] is a quantitative magnetic resonance (MR) method that measures myelin water and has been used extensively to study many myelin-related diseases in both brain and spinal cord, including multiple sclerosis (MS) [118, 215], neuromyelitis optica spectrum disorder [151], schizophrenia [110], phenylketonuria [196], Niemann-Pick disease [40], Krabbe disease [117], neurofibromatosis-1 [13], progressive solitary sclerosis [126], stroke [21], Parkinson's disease [9], concussion [229], and cervical spondylotic myelopathy [138]. Typically, MWI acquires multi-echo data to characterize the multi-exponential  $T_2$  decay signals generated from different water compartments within each imaging voxel. Image post-processing is then performed to separate the signal of the myelin water compartment, which exhibits shorter  $T_2$  re-

---

\*A version of this chapter has been published. Liu H, Xiang QS, Tam R, Dvorak AV, MacKay AL, Kolind SH, Traboulsee A, Vavasour IM, Li DK, Kramer JK, Laule C. Myelin water imaging data analysis in less than one minute. *NeuroImage*. 2020 Apr 15;210:116551.

laxation times from that of the intra- and extra- (IE) cellular water, from the total water signal. Over the years, various sequences have been used in MWI, including Carr-Purcell-Meiboom-Gill (CPMG) [224], 3D gradient and spin echo (GRASE) [177],  $T_2$  preparation ( $T_2$  prep) [173], and multi-gradient echo (MGRE) [88]. For MWI data analysis, many fitting algorithms [3, 50, 170, 184, 224] have been developed to decompose the voxel-wise multi-exponential decay data into a spectrum of  $T_2$  components, from which the myelin water fraction (MWF, the ratio of myelin water signal to total signal), is of the most interest and can be extracted.

Non-negative least squares (NNLS)  $T_2$  fitting algorithm [106, 121, 178], first introduced to MWI by Whittall and Mackay [224], is a commonly used analysis method. NNLS makes no prior assumptions about the total number of distinguishable water compartments and their corresponding  $T_2$  values, which is a highly desirable feature especially when studying a complex biological system such as pathological lesions with heterogenous composition. However, having very few initial assumptions leads to an underdetermined problem with non-unique solutions, making the NNLS MWF calculation results unstable. Alternatively, many other fitting algorithms have subsequently been developed such as the spatially constrained multi-Gaussian model by Raj et al. [184], the Wald distribution by Akhondi-Asl et al. [3], and the quasi-Newton algorithm by Du et al. [50]. These methods usually offer a more stable MWF estimation but at the expense of presuming only two or three water compartments (myelin water, IE water and free water) as a necessary initial assumption. The stability of NNLS was improved by using regularization to constrain the data misfit [210, 225], and further improvements have been made in recent years by applying spatial regularization [87] as well as non-local spatial regularization [233]. The latest NNLS analysis also incorporates the extended phase graph algorithm to estimate the refocusing flip angle of each voxel to correct for the effect of stimulated echoes. [176] Overall, there is no single perfect fitting algorithm to the ill-posed  $T_2$  decomposition problem and each method has its own strengths and weaknesses. For this proof of concept paper, we focused on the NNLS-based analysis method due to its high popularity [137, 139] and good reproducibility [127], as well as the fact of it being histologically validated [111, 112], and used  $T_2$  data from a common acquisition approach, the 3D GRASE sequence [177].

Despite reductions in the whole brain scan time of 3D GRASE to under 8 minutes [237], clinical use of MWI for MS and other demyelinating diseases has not yet been possible for a number of reasons, one of which is related to the speed and complexity of MWI data analysis. Fitting noisy MR data with a simple NNLS algorithm is typically not good enough because NNLS is very susceptible to noise, leading to unstable MWF results and unsmooth appearance of the resulting MWF map. Regularized NNLS fitting with stimulated echo correction [176] is, for the most part, required by today's standards. But the mathematical complexity of such integration makes it very difficult to implement for new users. More importantly, the computational time required for whole brain data analysis using NNLS typically takes several hours for a modern workstation PC, which is unacceptable in clinical settings. Recent effort made by Yoo et al. [232] using multicore CPU and graphics card parallelization can accelerate the NNLS analysis by approximately 4 times, and produce similar MWF values with small and explainable differences. However, a successful implementation of this method requires high-end hardware integration and relevant expertise in computing, which is also not always clinically feasible.

Another approach to shorten MWF analysis time is to use a neural network (NN) [194] algorithm, which is a supervised deep learning method that has attracted much attention in various fields including MR. A typical NN consists of an input layer to take the numerical input data, an output layer to yield the NN calculation results, and in between, there are hidden layers which are optimized by labelled training data to acquire the ability of mapping from the input data space to the desired output space. The basic building blocks for each layer are called nodes, which are connected between adjacent layers. The strength of the connection is governed by weights and biases which need to be optimized during training. The number of nodes and layers in a NN can be varied depending on the complexity of the problem. Before training, the activation function of each layer is defined to produce the output of each layer and introduce nonlinear properties to the NN. The loss function is defined to measure the error between the NN predicted values and the ground truth labels. During training, an iterative process is taken to minimize the loss function, and the step size of each iteration towards the global minimum of the loss function is determined by the learning rate. The data of a typical deep-

learning study is partitioned into 3 groups, namely the training set, validation set, and testing set. The training set is used during the iterative training process of the NN. If the training set has a very large size and is fed into the NN all at once, the training may become difficult and time-consuming. To solve this problem, the training set can be split into many data blocks (also known as mini batches), each of which usually contains 128, 256 or 512 training examples. Training on the mini batches is a commonly used approach when it comes to large-sized training sets. The validation set is used during training, to assess the prediction accuracy of the NN during each training iteration; during validation the loss, or error rate, is determined at each step which prevents overfitting. The training continues until the accuracy on validation data stops improving. Finally, the testing set is only used once, after NN training is completed. Such data partitioning ensures the testing data is obscured from the whole training process so that the one-time testing result is a true measurement of the actual predictive power of the trained NN. For additional background on machine learning and NN the reader is pointed to several comprehensive references. [125, 194]

In recent years, NN has been successfully implemented in many MRI applications from image acquisition to data analysis [143], most of which outperformed conventional methods in terms of faster speed and better accuracy. In our study, we proposed to train a deep learning NN to calculate MWF to overcome the aforementioned limitations of MWI. We will use the latest NNLS algorithm [176] to produce the ground truth labelled training data, so that the trained NN can (1) produce faster voxel-wise MWF calculations on new data and (2) be easier to implement with common computer compatibility. In this paper, we examined the accuracy of the proposed NN as a faster and computationally compact representation of the commonly used NNLS method. [84] We also explored the feasibility of applying our NN trained by healthy brain data to calculate MWF for other central nervous system tissues including MS lesions and spinal cord, as well as data collected from a different scanner.

## 5.2 Methods

### 5.2.1 MWI data acquisition and pre-processing

#### Training data:

MRI data for NN training were collected at 3T using an 8-channel SENSE head coil (Philips Achieva), including 4 healthy volunteers (4 males, age range 29 – 50 years) and 1 MS volunteer (female, age 39). MWI was performed using a 3D GRASE sequence (32 echoes,  $TE1/\Delta TE/TR = 10/10/1000\text{ms}$ , axial matrix size =  $232 \times 186$ , acquired resolution =  $1 \times 1 \times 5 \text{ mm}^3$  for 20 slices, reconstructed resolution =  $1 \times 1 \times 2.5 \text{ mm}^3$  for 40 slices, EPI factor 3, slice oversampling factor 1.3, SENSE factor 2, acquisition time = 14.4min). [177]The five brains were extracted by using the ‘bet’ tool in FSL software [200] on the first echo image to remove the skull and extract the brain tissue. This mask was then propagated to the rest of the echoes in the train. 32-echo decay data from all voxels in each brain were subsequently extracted using in-house software created with Python. In total, there were 2,952,684 voxels for training.

#### Testing data:

To illustrate the generality of the trained NN, we collected testing data from two additional healthy brains (2 males, 55 and 68 years old, total 1,182,365 voxels), one brain with MS lesions (female, 26 years old, lesion regions: 7838 voxels), and one healthy cervical spinal cord (male, 29 years old, C2 to C3 segment: 1433 voxels) from the same scanner (Philips Achieva). The testing brain data was acquired using the same 3D GRASE sequence and the same data extraction steps described above. The spinal cord MWI data were acquired with a modified 3D GRASE sequence (32-echo,  $TE1/\Delta TE/TR = 10/10/1500\text{ms}$ , 8 axial slices,  $FOV = 180\text{mm} \times 150\text{mm} \times 40\text{mm}$ , acquired resolution =  $0.75 \times 0.75 \times 5 \text{ mm}^3$ , reconstructed resolution =  $0.63 \times 0.63 \times 5 \text{ mm}^3$ , slice oversampling factor 1.3, SENSE factor 2, acquisition time = 8.5 min). [141]The MS lesions were first manually segmented on the proton density image of the testing MS brain, and the spinal cord was segmented using Spinal Cord Toolbox [129]. Segmented tissue was then transformed

into the GRASE space via rigid registration. Voxel-wise 32-echo decay data within the registered lesion mask (7838 voxels) and spinal cord mask (1433 voxels) were subsequently extracted.

### Multi-site data:

To demonstrate the feasibility of multi-site usage of the trained NN, MWI brain data from another healthy volunteer (female, 31 years old, 528,229 brain voxels) were collected using a different MRI scanner. Ideally, an MRI scanner manufactured by a different vendor would be best for illustrating this point. However, we only had access to another MR system from the same manufacturer but with a different generation (3T Philips Ingenia Elition X) and a different receive coil (32-channel SENSE head coil) to illustrate the concept of multi-site usage. The identical brain GRASE sequence and data processing were used as described above.

### 5.2.2 Ground truth

Voxel-wise 32-echo decay data were analyzed by regularized NNLS (MatLab) with stimulated echo correction [176] (analysis program can be request from this URL: <https://mrresearch.med.ubc.ca/news-projects/myelin-water-fraction/>) to compute MWF as the ground truth label for each voxel. One should be aware the MWF value generated by NNLS is just an estimation. It is the established convention in the deep learning field for training labels to be called the ‘ground truth’, and so we will refer to the NNLS calculated MWF values as ground truth as these are the values the NN is being trained to replicate. Using the phrase ‘ground truth’ is only because NNLS was our reference method, which a trained NN was trying to replicate. The NNLS algorithm works in a way that the misfit of  $\chi^2$  is minimized by the following equation:

$$\chi^2 = \sum_{i=1}^N \left| \sum_{j=1}^M A_{ij} s_j - y_i \right|^2 + \mu \sum_{i=1}^N |s_i|^2 \quad (5.1)$$

where  $N$  represents the total number of data points;  $M$  represents the number of logarithmically spaced  $T_2$  decay times,  $s_i$  represents the amplitude of the  $T_2$  distribution that needs to be solved;  $A_{ij}$  is the kernel matrix for the  $T_2$  exponential decay;

$y_i$  is the measurement data; and  $\mu$  is the regularization factor which was chosen to be the largest value that allows a misfit of less than  $1.02\chi^2$  [146] in our analysis. [87, 130, 224] To initialize the analysis program, 40 logarithmically spaced  $T_2$  times in the range from 15ms to 2s were defined as the set of basis  $T_2$ s in equation 5.1. Detailed calculation steps have been described in a previous paper by Prasloski et al. [176] The output of the fitting program was a voxel-wise  $T_2$  distribution and the MWF was defined as the area under the  $T_2$  distribution between 15ms to 40ms relative to the total area under the entire distribution. All analysis parameters were selected using the most commonly used values in accordance with many previous studies. [53, 127, 130, 137, 139, 141]

### 5.2.3 Neural network model and model training

There were 7 candidate NN models with different architectures constructed using Tensorflow [1], which is a commonly used open-source software library for deep learning. The design of all NN models was to take the 32-echo data as input and predict MWF at the output layer, but varied in the size and the number of hidden layers (Figure 5.1). All NN models were optimized by adaptive moment estimation (Adam) [95] and each layer of each NN was activated by rectified linear unit (ReLU) [169]. The loss function was using mean squared error (MSE) and defined by the following formula:

$$Loss = \frac{1}{n} \sum_{i=1}^n (y_i - \hat{y}_i)^2 \quad (5.2)$$

where  $n$  is the total number of training examples,  $y_i$  is the NN calculation result for the  $i^{th}$  training example, and  $\hat{y}_i$  is the NNLS ground truth label for the  $i^{th}$  training example. All NN models were initialized with Xavier uniform initializer<sup>50</sup> and the learning rate was set to 0.0005. The training data were randomly shuffled to break the data similarities of adjacent voxels and split into mini batches, each with a size of 512 training examples. Approximately 20% of total training data (600,000 voxels) were randomly selected and used as a validation set to determine the stopping criterion for training and to compare the performance of different NN architecture candidates. The training and validation set split ratio was determined empirically.

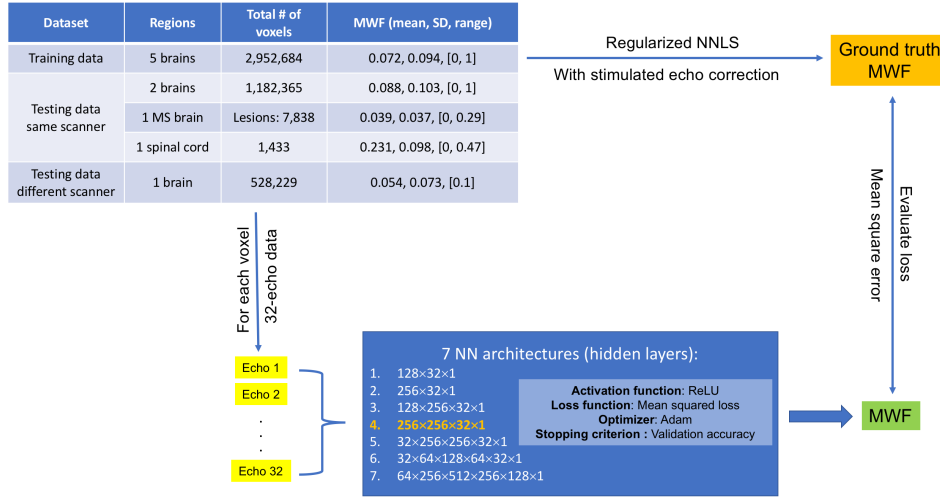


**Figure 5.1: Schematic of workflow.** 32-echo data from 5 brains (4 healthy, 1 multiple sclerosis (MS)) were used for training. Two healthy brains, 1 MS brain with segmented lesions, and 1 spinal cord acquired by the same scanner were used as testing data. One healthy brain acquired by a different scanner were also used for testing. The ground truth was calculated by regularized non-negative least squares (NNLS) with stimulated echo correction. The neural network was constructed with fully connected layers (activation function: ReLU, optimizer: Adam, loss: mean square error).

Training of each NN candidate was stopped when the accuracy on the validation set did not improve further for at least 100 epochs, where improvement was defined as a decrease in MSE. The validation MSE of the 7 trained models are displayed in **Table 5.1**. The optimal NN model architecture (hidden layers: 256×256×32) was empirically chosen to achieve the balance between the validation accuracy and the risk of overfitting for deeper networks; this architecture had one of the lowest validation losses while still having a simple structure. The workflow is depicted in **Figure 5.1**. For simplicity, we use NN\_opt to denote the selected trained model of three hidden layers (256×256×32) from this point below in this paper.

Model	Validation loss
128×32	$8.35 \times 10^{-5}$
256×32	$7.26 \times 10^{-5}$
128×256×32	$5.04 \times 10^{-5}$
<b>256×256×32</b>	<b><math>4.53 \times 10^{-5}</math></b>
32×256×256×32	$5.39 \times 10^{-5}$
32×64×128×256×32	$4.29 \times 10^{-5}$
64×256×512×256×32	$4.16 \times 10^{-5}$

**Table 5.1: Validation loss of 7 NN models.** 7 candidate NN models with different hidden layers were constructed and trained respectively. The training stopped when the validation loss (mean squared error) did not decrease for 100 epochs.

#### 5.2.4 Trained model evaluation

The trained NN\_opt model was applied to the testing data (2 healthy brains, 1 MS brain with segmented lesions, and 1 healthy cervical spinal cord) to produce MWF. Processing times of the trained NN\_opt model and NNLS calculation of whole brain and spinal cord MWF were recorded respectively for comparison (CPU: Intel(R) Core(TM) i7-5930K @ 3.5GHz, 32GB RAM). For the two healthy brains, average MWFs from 6 regions of interest (ROI) (all gray matter, all white matter, corpus callosum, corticospinal tract, forceps major, forceps minor) were also extracted and compared with the NNLS ground truth. All ROIs were chosen from Johns Hopkins University (JHU) atlas [220] and registered to GRASE-space using FSL nonlinear registration tool ‘FNIRT’. The predicted MWF values by NN\_opt were compared voxel-wise with the NNLS ground truth. In particular, absolute and relative differences, correlations (R-square, t-test) between NN\_opt predictions and NNLS ground truth, and mean absolute error (MAE) of all voxels were assessed. To demonstrate the robustness of the trained model, we evaluated the correlations between the NN\_opt MWF errors and the actual flip angles estimated by extended phase graph simulation [176]. We then tested NN\_opt at different SNR levels, by adding additional noise (SNR = 50 and 100) to the original multi-echo MWI data.

### 5.2.5 Normalized data training

Using the absolute voxel intensity for NN training raises the concern for generality because some scanner-specific factors such as amplifier gain may affect the absolute voxel intensity, especially when comparing data from different scanners so a second model (hidden layers:  $256 \times 256 \times 32$ ) was trained by the 1<sup>st</sup> echo normalized data to show the effect of using 1<sup>st</sup> echo normalization. This second trained model using normalized data was thus denoted as NN\_norm. As an illustrative example to compare its performance with NN, we only applied NN\_norm to calculate the MWF maps for two healthy brains collected by Philips Achieva and Elition respectively.

## 5.3 Results

### 5.3.1 MWF calculation time

The total training of the NN\_opt required 46 minutes and 55 seconds at 231 epochs when the validation loss (MSE) did not decrease after 100 epochs. The trained NN\_opt model was actually saved at 131 epochs (~27 minutes) to prevent overfitting. The processing times for the trained NN\_opt model to make MWF maps were 33 seconds for the whole brain and 4 seconds for the cervical spinal cord. In contrast, NNLS analysis took 1 hour and 33 minutes for the whole brain and 15 mins for the cervical spinal cord. The data processing speed of the trained NN\_opt model was more than 150-fold faster than that of the NNLS algorithm.

### 5.3.2 Healthy brains

**Figure 5.2** shows excellent visual correspondence between MWF maps from the NN\_opt model, NN\_norm model and NNLS analysis. No visual differences were observed for all slices in the MWF maps for both trained NN\_opt and NN\_norm models. Slight regional biases were only noticeable in the frontal regions in the error maps which were viewed with rescaling the colormap. It's also observed that the error of NN\_opt (MAE=0.004) was lower than that of NN\_norm (MAE=0.008). The NN\_opt model MWF predictions and the NNLS ground truth from 6 ROIs of the two testing healthy brains are summarized in **Table 5.2**. Using one of the

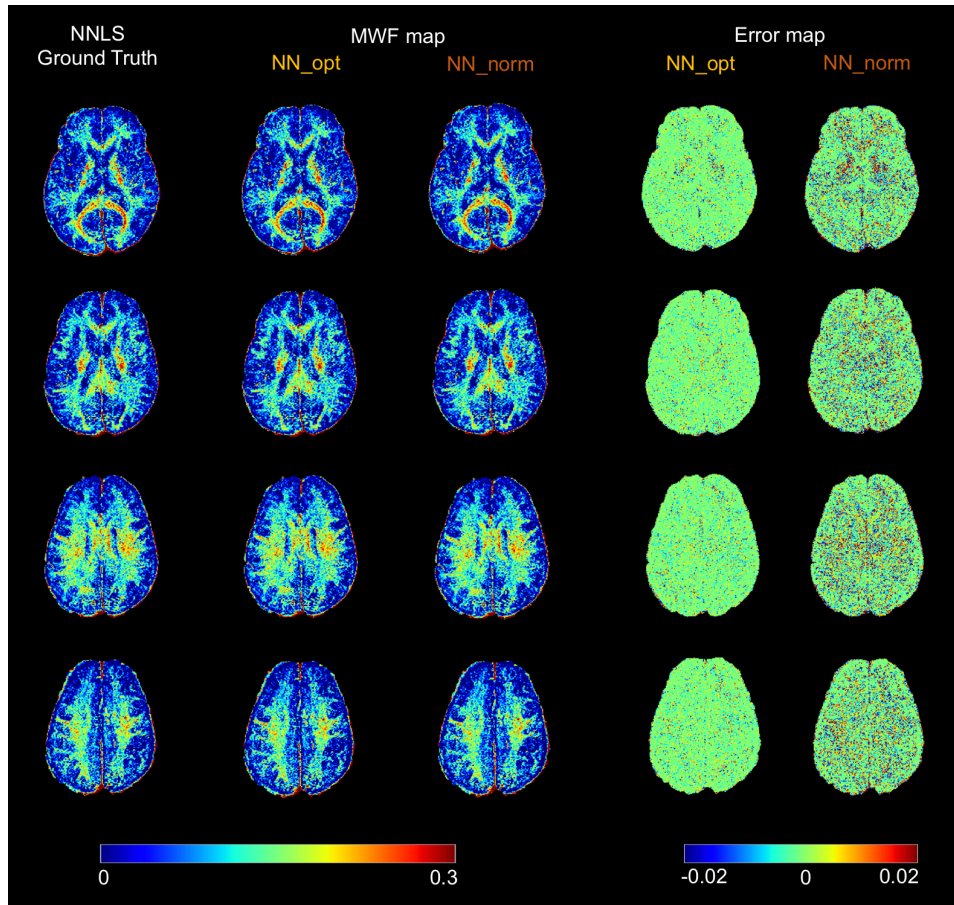


**Figure 5.2: Visual comparison of brain MWF maps.** The brain MWF maps carried out by the neural network models (NN\_opt and NN\_norm) and the NNLS ground truth, as well as the error map between the two are shown side by side for 4 representative axial slices from healthy brain #1. Note that NN\_opt was trained by non-normalized data while NN\_norm was trained by normalized data.

**Table 5.2: Summary of results for the two testing healthy brains.** Absolute and relative differences were evaluated.

<b>Healthy brain 1</b>	<b># of voxels</b>	<b>NNLS ground truth</b>	<b>Absolute MWF differences: NN_opt vs. NNLS</b>	<b>Relative MWF differences: NN_opt vs. NNLS</b>
All gray matter	299,298	0.07±0.09	0.00009	0.13%
All white matter	168,675	0.11±0.06	0.00004	0.04%
Corpus callosum	19,778	0.13±0.06	0.00005	0.04%
Corticospinal tract	8,898	0.17±0.07	0.00016	0.09%
Forceps major	3,245	0.16±0.06	0.00012	0.08%
Forceps minor	3,285	0.11±0.06	0.00028	0.24%
<b>Healthy brain 2</b>	<b># of voxels</b>	<b>NNLS ground truth</b>	<b>Absolute MWF differences: NN_opt vs. NNLS</b>	<b>Relative MWF differences: NN_opt vs. NNLS</b>
All Gray matter	337,140	0.06±0.09	0.00008	0.14%
All White matter	199,637	0.10±0.07	0.00007	0.07%
Corpus callosum	18,709	0.13±0.06	<0.00001	<0.01%
Corticospinal tract	11,851	0.16±0.08	0.00015	0.09%
Forceps major	3,356	0.18±0.06	0.0004	0.22%
Forceps minor	3,414	0.10±0.05	0.00001	0.01%

healthy brains as an illustrative example, voxel-wise NN\_opt MWF correlated almost perfectly with NNLS MWF in the 6 different ROIs (average  $R^2 = 0.994$ ,  $p < 0.0001$ , MAE = 0.003, **Figure 5.3**).

### 5.3.3 MS lesions

The absolute and relative differences in the average MWF of the lesions (trained NN\_opt: (0.04±0.04); NNLS ground truth: (0.04±0.04)) were 0.0003 and 0.76% respectively, and strong voxel-wise correlation between the two calculation methods were observed ( $R^2 = 0.987$ ,  $p < 0.001$ , MAE = 0.003, **Figure 5.4**).

### 5.3.4 Spinal cord

Average MWF (0.23±0.10) for the cervical spinal cord C2-C3 segment calculated by the trained NN\_opt were very similar to NNLS ground truth (0.23 ± 0.10). The absolute and relative differences in whole cord MWF average were 0.0013

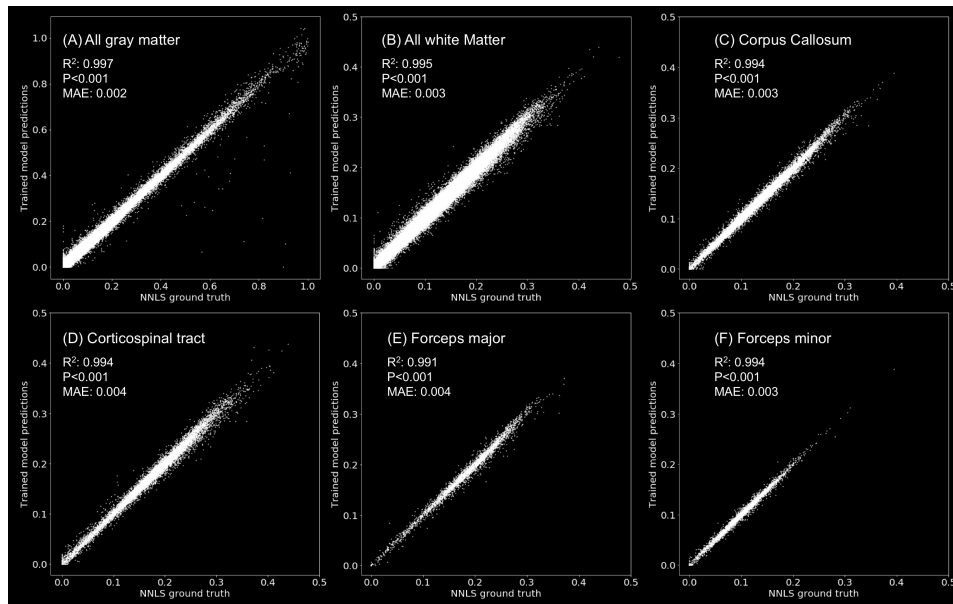


**Figure 5.3: Voxel-wise comparison of MWF within six different brain ROIs.** ROIs include all gray matter, all white matter, corpus callosum, corticospinal tract, forceps major, and forceps minor from healthy brain #2. R-square, p values from paired t-test, and mean absolute errors (MAE) were evaluated.

and 0.56% respectively. Excellent voxel-wise correlation between the two MWF calculation methods were found ( $R^2 = 0.987$ ,  $p < 0.000001$ ,  $MAE = 0.0076$ , **Figure 5.5**).

### 5.3.5 Data from a different scanner

In this illustrative example, the MWF maps of one healthy brain collected by a different scanner (Philips Elition) were carried out by NN\_opt, NN\_norm and NNLS ground truth respectively, and presented in **Figure 5.6** alongside with the error maps. Although the voxel-wise MAE were increased to 0.0048 for NN\_opt and 0.0108 for NN\_norm and errors occurred primarily in white matter, both models were still capable of producing visually very similar MWF maps as NNLS, with only subtle differences visible if examined closely.

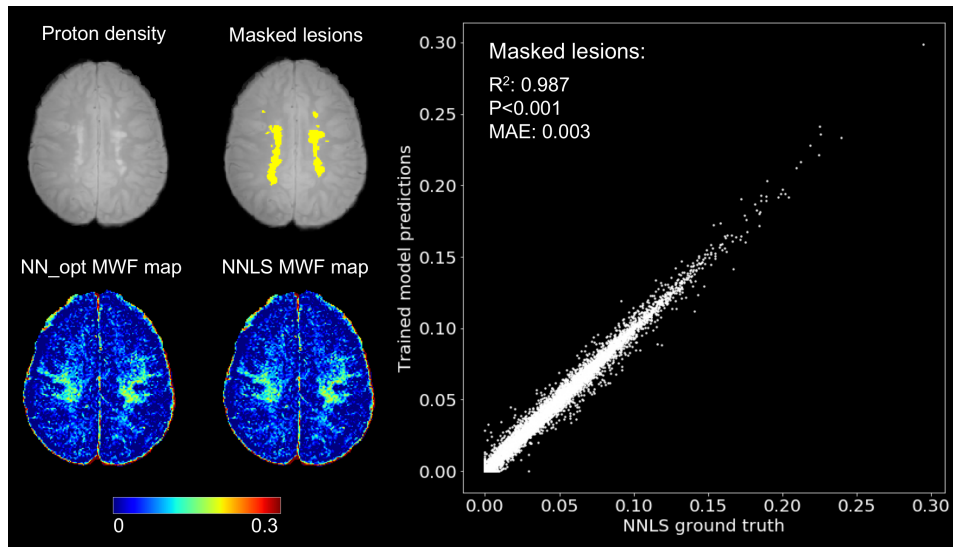


**Figure 5.4: MWF comparison for lesions.** The lesion mask was first manually drawn on the proton density image of a MS brain and then registered to the GRASE space. MWF maps carried out by the trained neural network model (NN\_opt) and the NNLS ground truth are visually the same. Highly significant voxel-wise MWF correlation between NN\_opt and NNLS is shown for the lesions.

### 5.3.6 Robustness of the trained model

Using one brain (collected by a Philips Achieva system) as an example, we plotted the prediction error of MWF made by the NN\_opt against the flip angle in each brain voxel and found no apparent correlation ( $R^2 < 0.001$ ,  $p < 0.001$ ) between the two (**Figure 5.7**). The same behaviour was observed with the other testing examples, including data collected using a different scanner (Philips Elition). Injecting noise at different SNR levels (SNR = 50 and 100) to the original brain data, we found NN\_opt was able to produce virtually the same MWF maps as NNLS, even at low SNR levels (SNR = 50) (**Figure 5.8**).

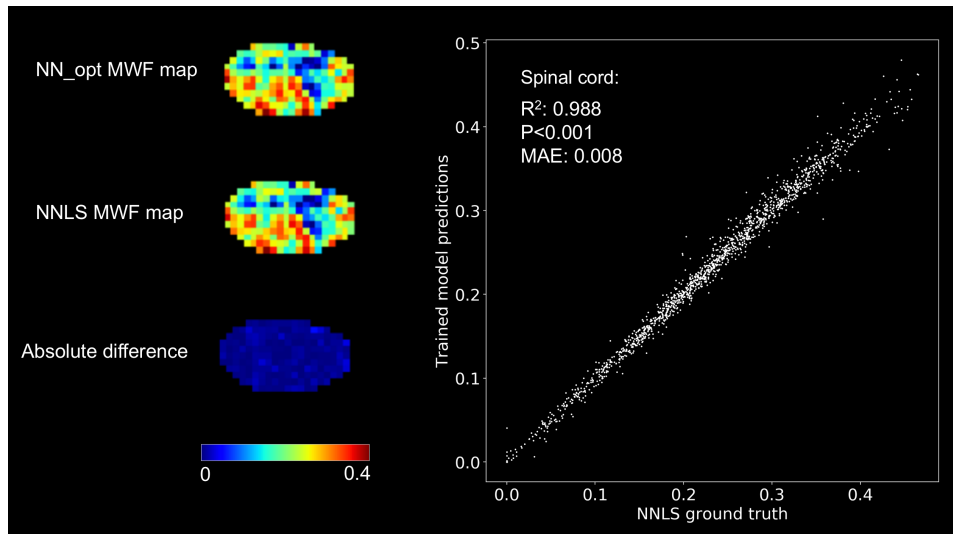


**Figure 5.5: Comparison of spinal cord MWF.** The MWF maps of a healthy spinal cord were carried out by the neural network model (NN\_opt) and the NNLS ground truth. No visual differences or regional biases were found. Excellent voxel-wise MWF correlation between NN\_opt and NNLS was observed in the spinal cord.

## 5.4 Discussion

### 5.4.1 Prediction accuracy

For all the regions that were tested, including healthy brains (from both scanners), MS lesions, and cervical spinal cord, MWF maps calculated by the trained NN\_opt model exhibit no qualitative differences compared with the NNLS ground truth MWF maps (**Figure 5.2, 5.4, 5.5, and 5.6**). Quantitatively, almost all voxels within each ROI exhibited excellent agreement (all  $R^2 > 0.98$ ,  $p < 0.00001$ ) between NN\_opt and NNLS (**Figure 5.3, 5.4, and 5.5**). For the healthy brains, absolute differences of mean MWF can only be found after four decimal places and the relative differences were  $< 0.25\%$  for white matter regions (Table 5.2), much smaller than the actual uncertainty of NNLS in estimating the true MWF. For the MS lesions, where low MWF values are expected due to demyelination and greater tissue heterogeneity exists compared to unaffected white matter [93, 116], the trained

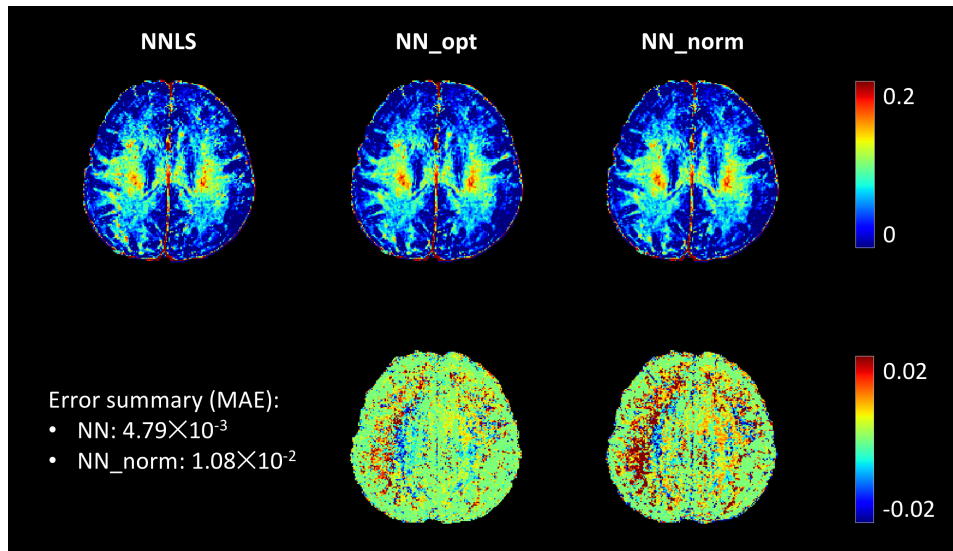


**Figure 5.6: Analysis of brain data acquired by a different scanner.** The brain MWF maps carried out by the neural network models (NN\_opt and NN\_norm) and the NNLS ground truth, as well as the error maps are shown side by side for one representative axial slice from a healthy brain data collected by a different scanner (Philips Elition). Note that NN\_opt was trained by non-normalized data while NN\_norm was trained by normalized data.

NN\_opt model still performed accurate MWF calculations with a relative difference of less than 1%. For the cervical spinal cord, we observed a slightly higher absolute difference (approximately 0.001) of NN\_opt MWF compared to NNLS ground truth, but the relative difference was low (<1%). Similarly, in our illustrative example where brain data were collected by a different scanner, the trained NN\_opt could still produce accurate MWF maps with slightly increased errors. Although training data only included brain data from one scanner, the trained NN\_opt was still able to overcome the challenge of these inherent differences in both the spinal cord and the different scanner data, and performed well in calculating the MWF without any data normalization. To summarize, the extremely low error of the trained NN\_opt model demonstrates that it is capable of producing virtually the same MWF maps as NNLS for the brain, pathological lesions, spinal cord, and data collected from a different scanner.

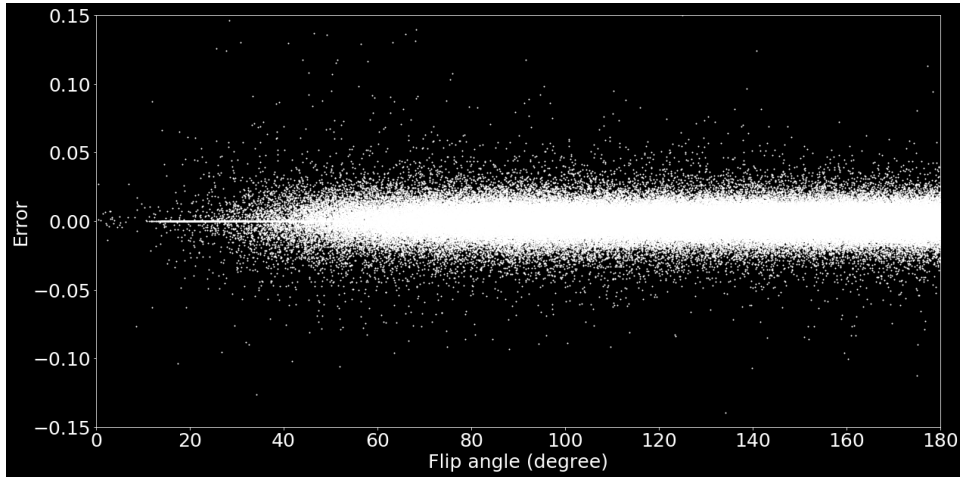


**Figure 5.7: Neural network prediction error vs. flip angle.** The actual refocusing flip angle deviates from the prescribed 180 degrees due to B1 inhomogeneity. The voxel-wise flip angle was estimated using extended phase graph algorithm. The neural network (NN\_opt) prediction error is plotted against the actual flip angle.

#### 5.4.2 NN\_opt vs. NN\_norm

It is observed that the MWF values calculated by the NN\_norm model have larger errors than that of the NN\_opt model (**Figure 5.2 and 5.6**), raising a concern about the 1<sup>st</sup> echo normalization method used in NN\_norm. Normalization to a proton density weighted image may be an alternative, assuming the within-subject image registration can be done successfully. Note that the first echo image acquired at 10ms in our study cannot be regarded as an ideal proton density weighted image because the TR used in our sequence was 1 second, which is not long enough to fully eliminate the T1 weighting. Moreover, the excellent performance of NN\_opt on data collected from a different scanner with a different coil (**Figure 5.6**) demonstrates the robustness of the trained NN\_opt. However, slightly enlarged MAE ( $4.79 \times 10^{-3}$ ) of the NN\_opt model on the different scanner data indicates the trained NN\_opt may have some biases towards different scanners, but not to the extent of corrupting accurate MWF predictions. This finding also raises the question to what extent the trained NN\_opt can tolerate variations of the absolute intensity in the data collected from different scanners. It is unlikely that NN\_opt would be

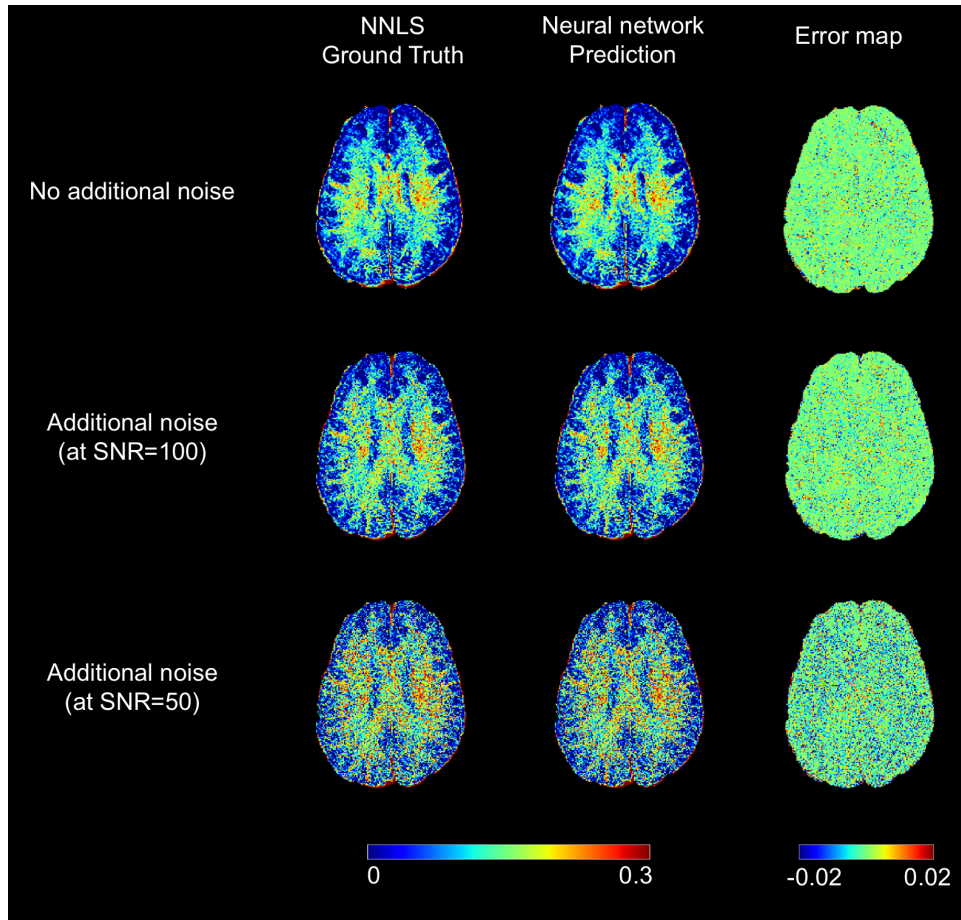


**Figure 5.8: Neural network prediction at different SNR levels.** Additional noise is injected at SNR = 100 and SNR = 50. Neural network (NN\_opt) predictions are compared with NNLS ground truth. MWF and its error maps of one representative axial slice are shown.

completely reliable on all systems due to the somewhat random effects of receiver gains on overall signal intensity. One may propose to multiply the different scanner data by a constant scaling factor to match the intensity level of the training data, and then apply the NN\_opt for a more accurate MWF calculation. Our post-hoc consideration of such an approach found such data scaling did not work well and generated unreasonable MWF maps, revealing that the data scaling step may likely worsen the performance of NN\_opt. From this perspective, NN\_norm has an intrinsic advantage for being truly scale invariant and is thus safer to use when it comes to data from a different scanner. Collectively, when a different scanner is used, fine-tuning or further training of the existing NN\_opt and NN\_norm models by including training data from that particular scanner is certainly encouraged. Our illustrative example demonstrates the feasibility of this approach, but a multi-vendor study with more participants is warranted to explore this further.

#### **5.4.3 Trained NN\_opt sensitivity to flip angle and SNR**

Although the NNLS ground truth was produced with B1 inhomogeneity correction, how resilient the trained NN\_opt is to the actual flip angle was a reasonable concern. We addressed this concern by showing that the prediction accuracy of the trained NN\_opt has no dependency on the actual flip angle (**Figure 5.7**). Another possible concern was the robustness of the NN\_opt to decreased SNR. Thus, we tested the trained model by adding additional noise to the original data. It was observed that the NN\_opt model is still capable of producing visually the same MWF maps as NNLS even when SNR is poor (additional noise at SNR=50) and the NNLS ground truth algorithm starts to fail (**Figure 5.8**). Overall, interrogations on the flip angle and decreased SNR demonstrate the proposed NN\_opt model is a robust representation of the NNLS algorithm with stimulated echo correction and regularization.

#### **5.4.4 Implementation: NN vs. NNLS**

The NNLS algorithm has been extensively applied in many fields and the code for NNLS is mostly open source accessible. However, in most scenarios with MWI, simply applying the exact open source code of NNLS will likely produce unsatis-

factory results. In recent advancement of MWI analysis, the NNLS algorithm has been incorporated with stimulated echo correction [176] for more accurate MWF estimations, and regularization is usually applied [50, 225, 233] for smoother appearing maps. These integrations make the modern NNLS analysis mathematically complex and computationally expensive. Customization of open source code by users is almost always required to include stimulated echo correction and regularization, making the modern NNLS implementation nontrivial. Therefore, in addition to its lengthy data processing time, the implementation complexity also prevents NNLS analysis from being widely used. To overcome this hurdle, our proposed NN\_opt was trained with regularized NNLS ground truth labels that have been corrected for stimulated echoes. As a result, the trained NN\_opt model is inherently embedded with features of regularization and stimulated echo correction, thus no further customization is needed. Besides, from a mathematical point of view, what the trained NN model does to the imaging data is essentially a few simple steps of multiplication and addition. Compared with the optimization process of conventional fitting algorithms, it is computationally inexpensive and can be easily implemented on various platforms (matlab, python etc.) with common hardware compatibility. Finally, the trained NN\_opt model is super lightweight (file size for our NN\_opt model: 80 KB) so it can be easily stored and distributed either online or locally.

#### **5.4.5 Limitations of current model**

A few limitations need to be considered. (1) The trained NN\_opt model inherits all of the NNLS algorithm's defects. For example, the current NNLS analysis is susceptible to noise so high-quality data is required in order to obtain a reliable MWF estimation. The trained NN\_opt model suffers the same problem since we used NNLS results as the ground truth for training. (2) For this proof of concept study, we only trained the NN\_opt with one set of initialization parameters for NNLS analysis (number of  $T_2s = 40$ ,  $T_2$  range = [15, 2000] ms, and MWF window = [15, 40] ms), on data collected using one version of the GRASE sequence. Although NNLS initialization parameters were set to the most commonly used values, there are still occasions, such as applying MWI to spinal cord [147] and post-mortem

tissue samples [119], when adjustments to these initialization parameters may be needed. Nevertheless, this problem can be fixed by training multiple NN models using different sets of initialization parameters since the one-time training time is acceptable. Training of new NN models can be accelerated by transfer learning, where our existing NN<sub>opt</sub> and NN<sub>norm</sub> models are used as the starting point for training the new model, due to the similarities between these two tasks. The transfer learning approach also applies when data acquisition sequence parameters are modified. (3) NNLS analysis is able to output a  $T_2$  distribution instead of just MWF. Many other valuable quantities such as total water content [116] or geometric mean  $T_2$  of IE water [147] can also be extracted from the voxel-wise  $T_2$  distribution. An important next step will be constructing and training a multi-output NN model that can make calculations of all of these other important quantities. (4) The multi-center usage was demonstrated using a different scanner but it was from the same manufacturer. It is important to investigate the performance of the proposed NN in analyzing data acquired by scanners of different manufacturers in the future.

#### **5.4.6 Other quantitative MRI techniques**

Similar to MWI data analysis, many other quantitative MRI (qMRI) techniques, such as neurite orientation dispersion and density imaging (NODDI) [236] and multicomponent driven equilibrium single pulse observation of  $T_1$  and  $T_2$  (mcDESPOT) [44], are also mathematically complex and computationally expensive for their image post-analysis. Besides the reliability issues of these qMRI techniques for individual use, lengthy data processing time is another common problem. In our opinion, the methodology of using a NN to create a fast and compact representation of a complex mathematical function can also be easily adopted by other qMRI data analysis to significantly shorten the image post-processing time.

#### **5.4.7 Comparison to kernel regression**

Kernel regression (KR) [193] is a classical machine learning method that also has the ability to map any qMRI data to the desired output in theory similar to NN. Due to the non-iterative nature of the training process, a conventional KR model can be trained in seconds, which seems to be a huge advantage over the NN method. An-

other advantage of KR is that it is mathematically explainable, unlike NN which is a black box operation. However, the conventional KR method is only suitable for a small or moderate dataset and has problems with scaling up. A large dataset like the one used in this study can cause memory and storage problems, leading to an unrealistic training time. [182] To overcome this hurdle, modern kernel approximation techniques such as random fourier [182] can be applied to effectively accelerate KR training. Based on KR method equipped with random fourier kernel approximation, Nataraj et al. proposed a framework, namely parameters estimation via regression with kernels (PERK), to calculate qMRI parameters such as steady state MWF. [170] The reported KR model training time for calculating steady state MWF was 3.6 seconds on 100,000 training examples with a dimensionality of 4. Assuming the same KR model were used, and scalability were linear (at best in theory, usually worse in practice), then the estimated training time on our GRASE data, which has 3 million training examples with a dimensionality of 32, would be at least 14.4 minutes (linearly scaled up by 240 times). However, the accuracy of MWF predictions cannot be compared here because the KR model was not trained on NNLS labels. In terms of the ease of implementation, code for the KR method can be found in many open-source libraries, but the code for implementation of modern kernel approximation methods for handling large datasets is not generally open-sourced [170] and usage instructions are often less detailed. Nevertheless, NN is able to intrinsically handle massive datasets with high dimensionalities. It can be constructed, trained and distributed by commonly used platforms such as Tensorflow, which only requires a minimum level of coding skills to use. On the other hand, how much training data is adequate for training NN and KR models remains an open question. A comprehensive comparison between NN and KR methods is beyond the scope of this study and we would leave the choice of method to the readers.

## 5.5 Conclusion

We have demonstrated that MWI data processing time can be dramatically reduced from hours to less than one minute (over  $150\times$  acceleration) without degrading the analysis results by using a trained NN model, which has been tested for healthy

brain and spinal cord, pathological lesions, as well as data acquired from a different scanner. Compared to conventional NNLS analysis incorporated with stimulated echo correction and regularization, our trained NN models (NN\_opt and NN\_norm) are considerably easier to implement. Finally, the proposed method of using a NN model to shorten the processing time can be used as a universal methodology for many other qMRI data analyses.

## Chapter 6

# Novel $T_2$ data analysis method: SAME-ECOS\*

### 6.1 Introduction

$T_2$  relaxation in biological tissues measured with a multi-echo experiment is typically characterized by multi-exponential decays because multiple water pools may exist within a single image voxel. [226] The  $T_2$  times of different water pools are governed by the microenvironment of water molecules. For example, myelin water, the water trapped in myelin bilayers, exhibits a shorter  $T_2$  relaxation time than that of intra/extra-cellular water (IE) and free water. [146] However, accurately depicting the spectrum of constituent  $T_2$  components for each image voxel from MR relaxation data is nontrivial. Because the decay process of multiple water pools takes place simultaneously, the MR receiver coil can only record a signal that is the sum of multiple exponential decay components. Consequently, one has to solve a mathematical problem of fitting a superimposed relaxation signal into its constituent components. This mathematically complex problem is commonly seen in many other quantitative sciences and is often considered as an ill-posed

---

\*A version of this chapter has been submitted to Magnetic Resonance in Medicine. A preprint version has been uploaded to arXiv: Liu H, Xiang QS, Tam R, Kozlowski P, Li DK, MacKay AL, Kramer JK, Laule C. Introduction to a novel  $T_2$  relaxation analysis method SAME-ECOS: Spectrum Analysis for Multiple Exponentials via Experimental Condition Oriented Simulation, arXiv preprint arXiv:2009.06761.

problem. [89] The analytical and numerical solutions to this problem have been comprehensively reviewed by Istratov et al. from a mathematical perspective. [89]

To provide a suitable solution specific to MR data, Whittall and Mackay [224] introduced the non-negative least squares (NNLS) [106, 121, 178] method that decomposes the multi-echo decay data into a spectrum of positive  $T_2$  times. The NNLS method makes no prior assumptions about the total number of  $T_2$  components, which is a desirable feature for modeling complex biological tissues with heterogeneous compositions. However, without constraining the number of components, the  $T_2$  fitting problem becomes underdetermined with non-unique solutions, making NNLS unstable and highly susceptible to noise even with strong regularization. In contrast, other fitting methods such as the quasi-Newton algorithm by Du et al. [50] and the Wald distribution by Akhondi-Asl et al. [3] usually provide more stable results and better noise resistance, but at the expense of modelling only two or three water pools, which limits their usage on unknown pathological tissues.

Simultaneously increasing the complexity and stability of a model is a paradox, seemingly impossible to improve one without diminishing the other in the game of multi-exponential decomposition. Our quest now was to find the line of best balance between these two factors. According to studies of information theory, the decay components can only be resolved to a certain resolution limit at a given signal to noise ratio (SNR). [12, 156] That is to say, due to noise contamination, there is always a limit in how closely the two neighboring components can be resolved, regardless of how sophisticated the analysis method is. This fundamental restriction on the resolution limit leads to a correlation between the SNR and the maximum number of components that can be reliably resolved in a particular analysis range. [134] The exact expression of this correlation is presented in the Methods, and plays a crucial role in our proposed approach.

On the other hand, machine learning algorithms, in particular supervised neural network methods [194], have been successfully implemented in many MR applications [143], especially for tasks involving parameter estimation. [33, 140] In short, a neural network can be trained to discover hidden patterns in data and to learn the mapping between two vector spaces. A trained neural network usually outperforms most conventional methods in terms of better accuracy and faster speed,

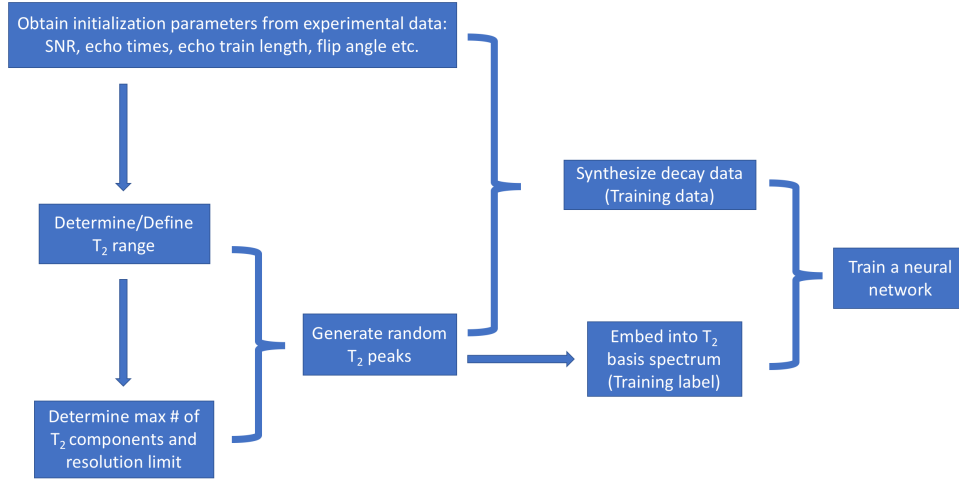


**Figure 6.1:** SAME-ECOS workflow.

particularly if the mapping is highly nonlinear. Additional background on the approximation properties of neural networks can be found elsewhere. [85]

Based on information theory and neural network algorithm approaches, we propose a novel method which we have called **Spectrum Analysis for Multi-Exponentials via Experimental Condition Oriented Simulation (SAME-ECOS)** for the analysis of multi-echo  $T_2$  relaxation data. The general concept of SAME-ECOS (**Figure 6.1**) can be briefly described by a series of calculation, simulation and model training operations: (1) determine the  $T_2$  range and resolution limit based on the experimental conditions such as SNR and echo times; (2) generate sufficient examples of random  $T_2$  spectra within the  $T_2$  range obeying the resolution limit; (3) compute multi-echo decay data using the randomly generated  $T_2$  spectra; (4) train a neural network model to learn the mapping between the simulated multi-echo decay data and the ground truth spectrum labels; (5) apply the trained neural network model to experimental data. In general, SAME-ECOS is a simulation-derived solver, powered by information theory and machine learning, to the problem of fitting multi-exponential decay data into a  $T_2$  spectrum. It is worth highlighting that SAME-ECOS has high flexibility of tailoring itself to different experimental conditions attributed to its unique simulation workflow. The detailed SAME-ECOS

algorithm is demonstrated in the Methods part by presenting an example with in-depth explanations.

## 6.2 Methods

Because the SAME-ECOS analysis method is tailored to different MR experimental conditions, we use one specific example here as a paradigm to demonstrate its simulation workflow, trained model evaluation, and experimental data application. Therefore, the Methods part of this introductory paper to SAME-ECOS is presented in the following sections as a particular experiment.

### 6.2.1 In-vivo MRI experiment

32-echo brain data (gradient and spin echo (GRASE),  $TE/\Delta TE/TR=10/10/1000\text{ms}$ , refocusing flip angle (FA)= $180^\circ$ , axial matrix size =  $232 \times 186$ , acquired resolution =  $1 \times 1 \times 5 \text{ mm}^3$  for 20 slices, reconstructed resolution =  $1 \times 1 \times 2.5 \text{ mm}^3$  for 40 slices, acquisition time = 14.4 minutes) [177] from one healthy volunteer (male, 57 years old) was collected at a 3T scanner (Philips Achieva) using an 8-channel head coil.

### 6.2.2 SAME-ECOS workflow

**(1) Choose the SNR range to be 70-300.** To initialize the simulation workflow, the SNR of the experimental data needs to be determined first, as calculations of the  $T_2$  range, the resolution limit, and especially the noise simulation, all depend on the SNR. The SNR was initially estimated to be approximately 167 by examining the noise variance of the air voxels proximate to the skull on the 1<sup>st</sup> echo image. However, most of today's MRI images acquired by multi-channel coils are reconstructed using parallel imaging [46], which complicates the estimation of SNR. Other factors, such as B1 inhomogeneity, may lead to regional variations in SNR. Therefore, the SNR of experimental data cannot be simply assessed by a single definitive number. To accommodate these hurdles, we empirically assigned the SNR a wide range of 70 to 300, instead of using a single value. This approach allows us to randomly select any SNR within the designated range at each simulation realization, making the resulting simulated data 'all-inclusive' after many

realizations.

**(2) Define the  $T_2$  range to be 7-2000ms.** Intuitively, the shortest detectable  $T_2$  decay component should have its residual signal greater than the noise level at the first measurement. Because the first echo is used later as a normalization factor, the second echo is actually regarded as the first measurement in our analysis. In theory, a minimum of two measurement points would be needed for the purpose of  $T_2$  fitting. That means the residual signal of the shortest  $T_2$  component in our analysis should be higher than the noise level at the third echo. Thus, the lower bound of the  $T_2$  range can thus be obtained using equation 6.1.

$$T_2^{\min} = -\frac{3rd\ echo\ time}{\ln\left(\frac{1}{SNR}\right)} \quad (6.1)$$

Given the SNR range of 70 to 300, the lower boundary is calculated to be approximately 7ms. On the other hand, an ideal experimental condition would be monitoring the decay as long as possible until the longest  $T_2$  component decays completely. [47, 195, 209] Then the upper bound for the analyzable  $T_2$  range can be determined using equation 6.2. [89]

$$T_2^{\max} = -\frac{last\ echo\ time}{\ln\left(\frac{1}{SNR}\right)} \quad (6.2)$$

However, the ideal experimental condition rarely happens as the decay monitoring time is often compromised to achieve a shorter scanning time for most in-vivo MR experiments including our own (last TE = 320ms). If equation 6.2 were used with our SNR range of 70 to 300, the longest analyzable  $T_2$  component would be less than 80ms, which is considered to be too short for the analysis of in-vivo brain imaging. Therefore, the upper boundary is manually extended to 2000ms based on the literature  $T_2$  ranges for brain. [106, 146, 226]

**(3). Determine the maximum number of resolvable  $T_2$  components to be  $M = 5$  and the resolution limit  $\delta = 3.098$ .** For a given SNR and  $T_2$  range, the decay components can only be resolved to a certain resolution limit. Link et al. [134] derived an expression (equation 6.3) relating  $T_2^{\min}$ ,  $T_2^{\max}$  and SNR, to the M

resolvable exponentials.

$$\frac{M}{\ln\left(\frac{T_2^{\max}}{T_2^{\min}}\right)} \times \sinh\left(\frac{\pi^2 \times M}{\ln\left(\frac{T_2^{\max}}{T_2^{\min}}\right)}\right) = \left(\frac{SNR}{M}\right)^2 \quad (6.3)$$

Derivations and justifications of equation 6.3 can be found in several publications. [89, 134, 156] Based on these previous theoretical studies, the maximum number of resolvable  $T_2$  components  $M = 5$  was obtained by numerically solving equation 6.3 to the nearest integer for the given SNR and  $T_2$  range. Note that  $M = 5$  is the universal integer solution to most SNRs in the range of 70-300 in our case. Then, the  $T_2$  resolution limit  $\delta=3.098$  was determined by equation 6.4. [89]

$$\delta = \left(\frac{T_2^{\max}}{T_2^{\min}}\right)^{\frac{1}{M}} \quad (6.4)$$

**(4). For each simulation realization:**

**a. generate random integers  $n < M$ ,  $FA \in [90^\circ, 180^\circ]$ , and  $SNR \in [70,300]$ .**

Note that the simulation did not include the case of  $n = M$  because when  $n = M$ , there is only one possible configuration for the  $M$   $T_2$  locations within the  $T_2$  range obeying the resolution limit, which would introduce an unwanted bias into the simulated dataset. Also note that the actual FA can deviate substantially from the prescribed FA due to B1 inhomogeneity, so we gave a  $90^\circ$  tolerance to account for the FA variations.

**b. generate  $n$  randomly located  $T_2$  components within the  $T_2$  range obeying the resolution limit  $\delta$ .** The locations and amplitudes of the  $n$   $T_2$  components were randomly assigned and normalized to one.

**c. synthesize 32-echo decay data.** The pure decay signal without noise of the  $n$   $T_2$  components (denoted as  $S_{\text{pure}}$ ) were synthesized (equation 6.5) using the extended phase graph (EPG) algorithm [79, 176] with  $T_1 = 2000\text{ms}$  as a default.

$$S_{\text{pure}} = \sum_{i=1}^{i=n} \text{Amplitude}_i \times \text{EPG}(T_{2,i}, \text{selected FA}) \quad (6.5)$$

To mimic the noise profile of a real MRI image [27], the  $S_{\text{pure}}$  was first projected

into the real and imaginary axes by a random phase factor  $\theta \in [0^\circ, 90^\circ]$ , followed by adding noises on both axes, and finally producing the magnitude of the noisy signal (equation 6.6).

$$S_{\text{noisy}} = \sqrt{(S_{\text{pure}} \times \sin \theta + \text{noise}_1)^2 + (S_{\text{pure}} \times \cos \theta + \text{noise}_2)^2} \quad (6.6)$$

where  $\text{noise}_1$  and  $\text{noise}_2$  were independently sampled from a Gaussian distribution with its mean = 0 and its variance was determined by equation 6.7

$$\text{Gaussian noise variance} = \frac{1}{\text{selected SNR} \times \sqrt{\pi/2}} \quad (6.7)$$

such that the noisy signal  $S_{\text{noisy}}$  would follow a Rician distribution at the selected SNR level. The synthesized noisy decay data were subsequently normalized to the 1<sup>st</sup> echo and saved for model training.

**d. Embed n  $T_2$  components into a spectrum representation depicted by 40 basis  $T_2$ s.** The 40 basis  $T_2$ s ( $t_1, t_2, t_3 \dots t_{40}$ ) were equally spaced within the  $T_2$  range on a logarithmic scale. The 40 weighting factors of the basis  $T_2$ s were used to represent the spectrum of n  $T_2$  components ( $T_{2,1}, T_{2,2}, \dots T_{2,n}$ ). Explicitly, each  $T_2$  component was depicted as a Gaussian-shaped peak by the basis  $T_2$ s, with the weighting factor  $w_i$  of the  $i^{\text{th}}$  basis  $T_2$  ( $t_i$ ) being calculated as

$$w_i = \sum_{j=1}^n \frac{1}{\sqrt{2\pi}} e^{-\frac{1}{2}(t_i - T_{2,j})^2} \quad (6.8)$$

The embedded  $T_2$  basis representation was normalized to one and recorded as the ground truth spectra for model training.

**(5) Train a neural network to map the decay data to its  $T_2$  spectrum.** A neural network (hidden layers:  $100 \times 500 \times 1000 \times 1000 \times 500$ , activation: SeLU [100] (hidden layers) and softmax [15] (output layer), optimizer: Adamax [95], loss: categorical cross-entropy [123]) was constructed using TensorFlow [1] to take 32-echo decay data as input and predict the weighting factors of the 40 basis  $T_2$ s at the output layer. The constructed neural network was trained to map the decay data to its  $T_2$  spectrum. We yielded 3,000,000 simulation realizations (step 4), 90% of which were used for the neural network training. The remaining 10%

simulation realizations were used for the validation that determined the stopping criterion for the training process. The training was stopped when the accuracy on the validation set did not improve further. This particular trained neural network is denoted as the SAME-ECOS model hereafter and can be applied to new 32-echo decay data to obtain  $T_2$  spectrum.

### 6.2.3 SAME-ECOS model performance evaluation

The performance of the SAME-ECOS model was evaluated using three designed tests and compared respectively with the results determined by a regularized NNLS solver equipped with stimulated echo correction [176] (analysis program can be requested here: <https://mriresearch.med.ubc.ca/news-projects/myelin-water-fraction/>). The kernel matrix for the NNLS analysis was adjusted accordingly to match our experimental and simulation parameters. The regularization parameter was chosen to be the largest value that allows a misfit of less than 1.02 times of the minimum misfit, which is commonly used in many studies. [53, 127, 137, 139, 141]

**Test 1:** 300,000 ground truth  $T_2$  spectra and their noisy 32-echo decay data were randomly generated following the workflow described in section 6.2.2. The decay data were analyzed by the SAME-ECOS model and NNLS respectively to produce the  $T_2$  spectra. The processing time was recorded. The ‘goodness’ of each spectrum fitting by both methods was quantitatively assessed using cosine similarity scores [76], which report values between 0 to 1, with 0 being the least similar and 1 being the most similar to the ground truth labels. The cosine similarity score is a commonly used metric that measures the similarities between two vectors, especially when the vectors are high dimensional. It is a suitable metric for our task since each  $T_2$  spectrum can be treated as a vector of 40 dimensions. The calculation of the cosine similarity score is defined explicitly in the following formula

$$\text{cosine similarity score} = \frac{X \bullet Y}{\|X\| \times \|Y\|} \quad (6.9)$$

Where  $X$  and  $Y$  are the vector representations of the predicted and the ground truth spectra;  $\|X\|$  and  $\|Y\|$  are their Euclidean norms respectively. Paired t-test was performed to determine whether there was a significant difference ( $P < 0.05$ ) in the cosine similarity scores calculated by SAME-ECOS and NNLS.

Pre-defined spectra	T <sub>2</sub> locations (ms)	T <sub>2</sub> amplitudes (normalized)
Spectrum 1	100	1
Spectrum 2	25, 120	0.3, 0.7
Spectrum 3	15, 80, 50	0.3, 0.5, 0.2
Spectrum 4	10, 60, 300, 1200	0.2, 0.4, 0.3, 0.1

**Table 6.1: Four pre-defined ground truth spectra.** The T<sub>2</sub> locations of each spectrum are selected obeying the resolution limit. Amplitudes are normalized to one.

**Test 2:** To examine the model robustness to noise, simulated decay data of 4 pre-defined ground truth T<sub>2</sub> spectra (**Table 6.1**) at SNR = 100 and FA = 180°, each with 100 different noise realizations, were passed to the SAME-ECOS model and NNLS for spectrum predictions. The location and amplitude of each ground truth spectrum were manually chosen to provide a visual-friendly data presentation. The spectrum analysis results of both SAME-ECOS and NNLS were normalized (sum to unity) prior to comparison. The similarity between each predicted and ground truth spectrum was assessed by cosine similarity scores defined above. The mean and standard deviation of the cosine similarity scores were also calculated.

**Test 3:** 10,000 ground truth T<sub>2</sub> spectra and their 32-echo decay data with noise realizations were randomly generated according to steps described in section 6.2.2. The decay data were analyzed by the SAME-ECOS model and NNLS respectively to produce the T<sub>2</sub> spectra. The myelin water fraction (MWF, a fraction of signal with T<sub>2S</sub> < 40ms)<sup>2</sup> was extracted from each predicted spectrum and compared with the ground truth MWF. Mean absolute error (MAE) in the MWF estimation was computed. The correlation between the errors of MWF estimation and the FA was evaluated using Pearson correlation analysis.

#### 6.2.4 Apply SAME-ECOS to experimental data

The SAME-ECOS model was applied to the experimental in-vivo GRASE data, which were pre-processed by normalizing to the first echo image. The processing time for the whole brain data analysis was recorded. From the resulting T<sub>2</sub> spectra, the MWF (T<sub>2S</sub> < 40ms) was extracted for each voxel. The masks of regions of interest (ROI) including whole brain, whole white matter, corpus callosum, corti-

cospinal tract, forceps major, and forceps minor were produced using the first echo image via the FSL segmentation tool. [239] The  $T_2$  spectra and MWF map was also produced using NNLS in the  $T_2$  range of 7-2000ms as a reference for comparison.

## 6.3 Results

### 6.3.1 Performance evaluation via simulation tests

#### Test 1: general performance

The processing time to make 300,000 spectra predictions was 22 seconds for the SAME-ECOS model and 1,620 seconds for NNLS (CPU: Intel(R) Core(TM) i7-5930K @ 3.5 GHz, 32 GB RAM). The mean cosine similarity score of the 300,000 spectra predicted by the SAME-ECOS model ( $0.838 \pm 0.189$ ) was significantly higher ( $p < 0.05$ ) than that of the NNLS ( $0.741 \pm 0.160$ ).

#### Test 2: robustness to noise

The resulting SAME-ECOS and NNLS spectra from each individual noise realization (grey) were plotted in **Figure 6.2** to compare against the ground truth spectrum (green). The average spectrum from 100 different noise realizations was also calculated for all SAME-ECOS and NNLS scenarios (blue: SAME-ECOS, red: NNLS). SAME-ECOS produced visually better results than NNLS for all scenarios. For spectra consisting of one or two  $T_2$  components, the SAME-ECOS model was able to make almost perfect predictions (cosine similarity score:  $0.998 \pm 0.002$  and  $0.951 \pm 0.05649$ , respectively); NNLS could also make accurate predictions but with more substantial variability (cosine similarity score:  $0.913 \pm 0.028$  and  $0.802 \pm 0.093$ , respectively). For spectra consisting of three or four  $T_2$  components, the performances of both methods started to degrade. However, SAME-ECOS (cosine similarity score:  $0.681 \pm 0.154$ ,  $0.579 \pm 0.128$ , respectively) was still making better predictions than NNLS (cosine similarity score:  $0.572 \pm 0.127$ ,  $0.573 \pm 0.085$ , respectively).

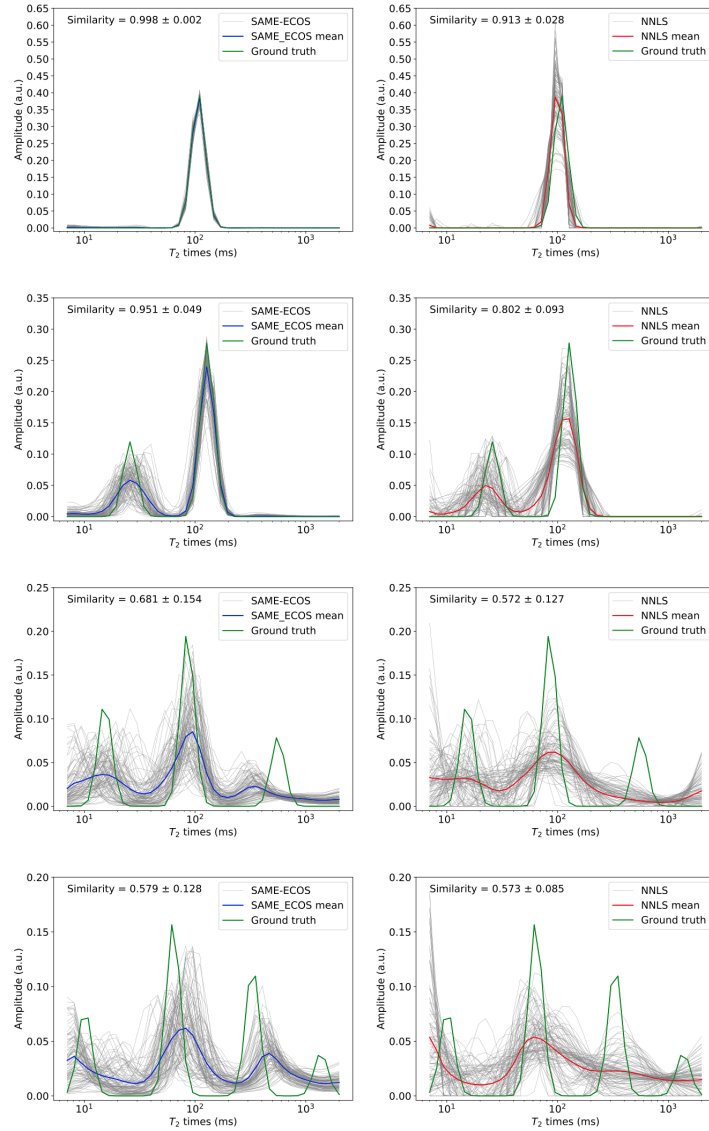


**Figure 6.2:**  $T_2$  spectra produced by SAME-ECOS (blue) and NNLS (red) respectively are compared with the ground truth spectra (green). Simulated decay data, which are generated from 4 pre-defined ground truth spectra (Table 1) each with 100 different noise realizations, are fed into the trained SAME-ECOS model and NNLS algorithm to generate the  $T_2$  spectra. Faded gray lines indicate the produced spectra for each noise realization. The mean and standard deviation of cosine similarity scores of 100 realizations are shown for each sub-figure.

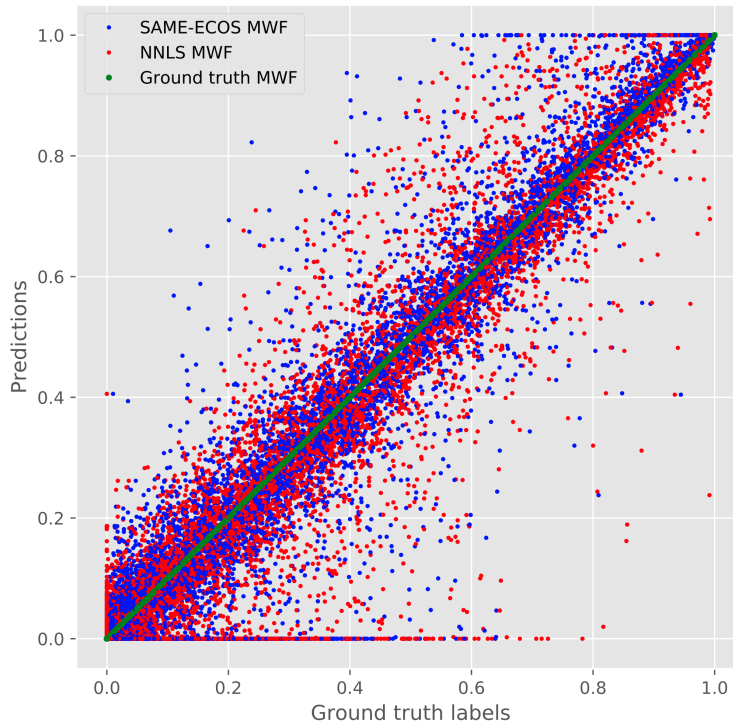


**Figure 6.3: Myelin water fraction (MWF) produced by SAME-ECOS (blue) and NNLS (red) are compared with the ground truth MWF (green).** 10,000 randomly simulated decay data examples were analyzed by SAME-ECOS and NNLS respectively. The MWF (fraction of signal with  $T_{2s} < 40\text{ms}$ ) was extracted from each predicted spectrum.

### Test 3: MWF prediction accuracy

MWF values were extracted using both SAME-ECOS and NNLS methods and plotted against 10,000 ground truth MWF values in **Figure 6.3**. SAME-ECOS MWF (blue, MAE=0.050) demonstrated slightly better agreement with the ground truth (green) than NNLS MWF (red, MAE=0.058). The MWF prediction errors of both methods are plotted against the FA in **Figure 6.4**, where the mean error of each FA was also presented for a visual check for biases. A small but noticeable positive bias (0.019, overestimation of MWF) was observed for the NNLS method, whereas SAME-ECOS did not show any obvious bias (0.007).

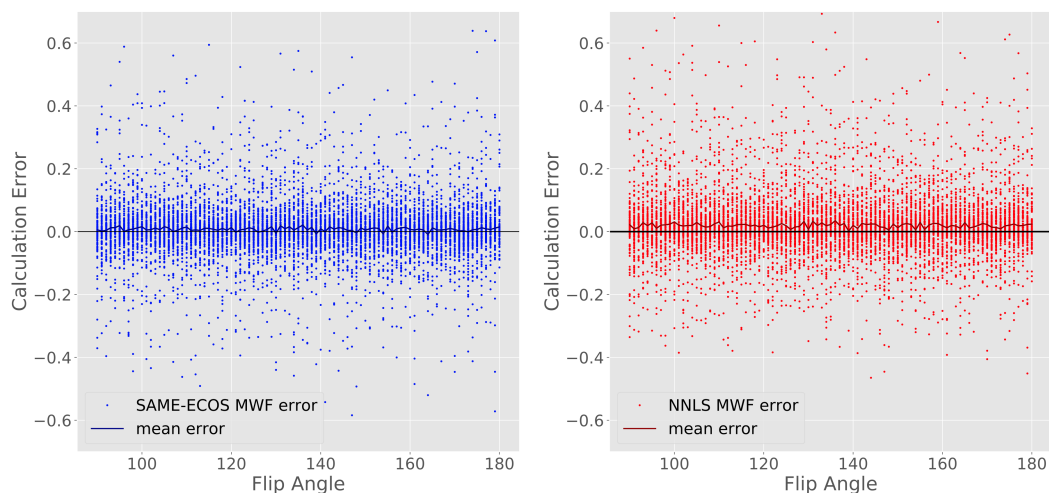


**Figure 6.4: Flip angle (FA) dependence of myelin water fraction (MWF) prediction errors.** 10,000 randomly simulated decay data examples were analyzed by SAME-ECOS and NNLS. Errors of MWF (fraction of signal with  $T_2s < 40ms$ ) was calculated and compared with FA. The mean error of each FA was also presented for a visual check for biases.

### 6.3.2 In-vivo experimental data: MWF maps

In-vivo GRASE data were analyzed by the SAME-ECOS model and NNLS. The processing times of the whole brain data were 3 minutes for the SAME-ECOS model and 86 minutes for NNLS. Six representative slices of the GRASE first echo, the resulting MWF maps produced by both methods ( $T_2s < 40ms$ ), and the voxel-wise MWF difference map (SAME-ECOS MWF – NNLS MWF), are presented in **Figure 6.5**. The SAME-ECOS MWF map is visually very similar to the NNLS MWF map, but subtle differences are still visible. Quantitatively, the SAME-ECOS mean MWF of whole white matter ( $0.131 \pm 0.080$ ) is lower than that of the NNLS approach ( $0.152 \pm 0.078$ ). **Figure 6.6** shows the voxel spectra, the mean spectra, and the mean MWF within the ROIs of the corpus callosum, corticospinal tract, forceps major and forceps minor. The SAME-ECOS mean MWF was lower than the NNLS mean MWF for most ROIs (except for forceps major). It is observed that for all ROIs, the SAME-ECOS mean spectra are able to resolve a short  $T_2$  peak (attributed to myelin water) in addition to a more dominate middle peak (attributed

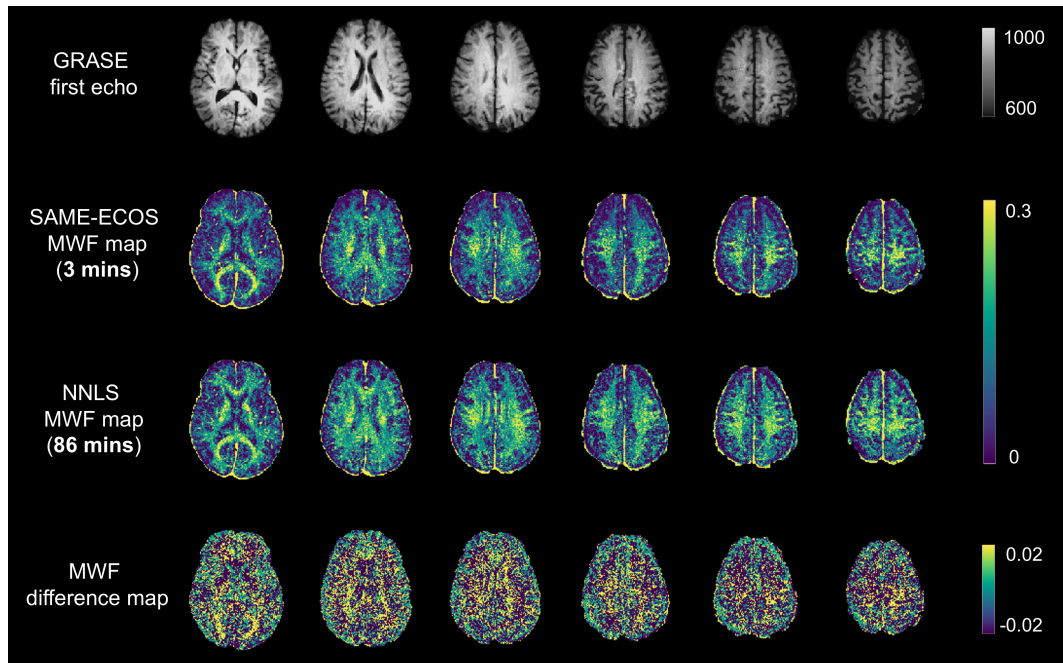


**Figure 6.5: SAME-ECOS and NNLS derived in-vivo myelin water fraction maps.** Six representative slices of the GRASE first echo, the resulting MWF maps produced by both methods ( $T_2s < 40ms$ ), and the voxel-wise MWF difference map (SAME-ECOS MWF – NNLS MWF), are shown.

to IE water), whereas the NNLS mean spectra can only resolve a single broad middle peak.

## 6.4 Discussion

### 6.4.1 SAME-ECOS vs. NNLS

From the results of all three simulation tests, the SAME-ECOS model largely outperformed NNLS. Using NNLS as the baseline, the SAME-ECOS model achieved 13.1% higher overall cosine similarity scores (**Test 1**), and 16.0% lower MAE of MWF predictions (**Test 3**), as well as demonstrated better robustness to noise (**Test 2**). Specifically, from visual inspection of the results presented in **Figure 2**, both

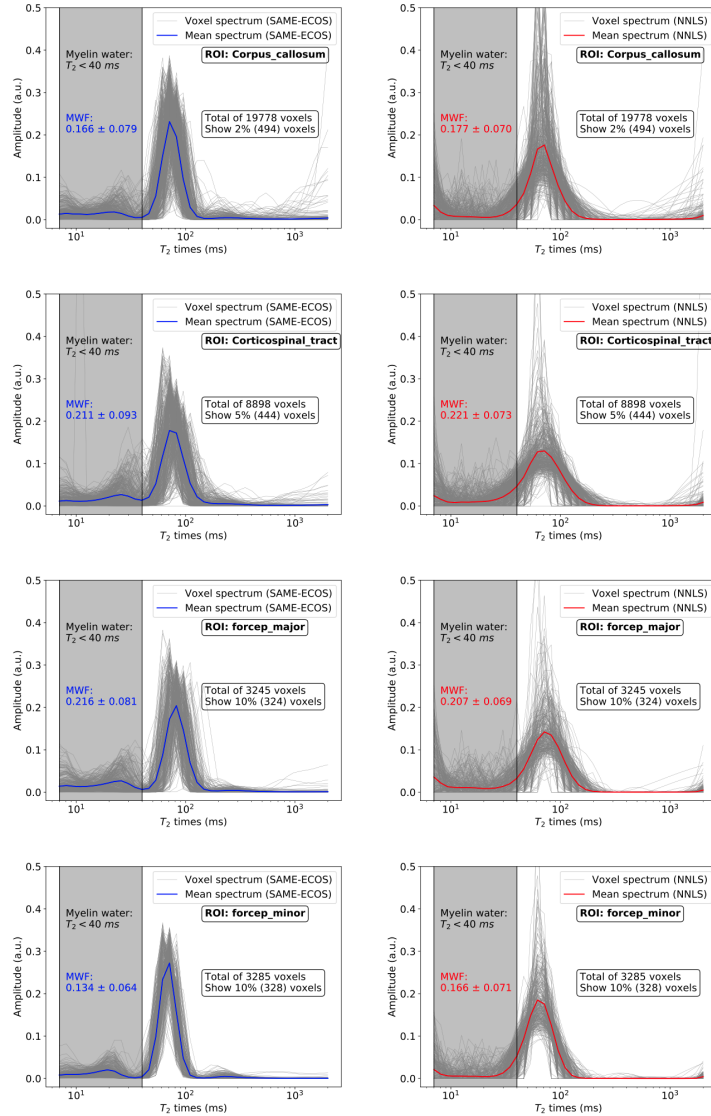


**Figure 6.6: Voxel spectra (gray), the mean spectra (blue: SAME-ECOS; red: NNLS), and the mean MWF ( $T_2 < 40\text{ms}$ ) within the four ROIs of the experimental in-vivo data. ROIs include the corpus callosum, corticospinal tract, forceps major, and forceps minor. The voxel spectra are only plotted for a fraction of the total number of voxels for a visual-friendly presentation as indicated in each subfigure. The mean spectrum and mean MWF are calculated from all voxels within each ROI.**

methods were able to produce accurate  $T_2$  spectra when the number of  $T_2$  components  $n \leq 2$ . However, when  $n > 2$ , the NNLS predictions became extremely unstable, resulting in over-smoothed mean spectra. This observation illustrates that, unlike NNLS being highly susceptible to noise, the SAME-ECOS model has a desirable feature of being relatively noise-inert. It is also noticed that both methods were incapable of producing reliable spectrum predictions particularly for the long  $T_2$  components (e.g.  $T_{2s} > 500\text{ms}$ ), which is likely due to the relatively short measurement time (the last  $TE=320\text{ms}$ ) so there was not enough information acquired to resolve the long  $T_2$  component accurately. In addition, as illustrated in **Figure 4**, NNLS was systematically overestimating MWF throughout the FA range under our investigation. In contrast, SAME-ECOS produced more accurate MWF values without any obvious biases. Overall, the current SAME-ECOS model demonstrated a better performance than NNLS in the interrogations using simulation tests.

Due to the lack of ground truth, it is difficult to judge which method is more accurate when it comes to in-vivo experimental data. However, in terms of data processing speed, SAME-ECOS is approximately 30 times faster than NNLS, achieving a whole-brain analysis in 3 minutes, which is more feasible in clinical settings. From a visual inspection of the MWF maps shown in **Figure 5**, these two methods produced similar results, but the SAME-ECOS MWF map appeared to be a little less noisy, making its white and gray matter distinction slightly more prominent. Interestingly, compared with SAME-ECOS, the NNLS mean MWF values in white matter regions were higher, which coincided with the NNLS MWF overestimation issue presented in **Figure 4**.

A thorough analysis of the NNLS spectra in a few white matter ROIs (**Figure 6**) revealed that the NNLS MWF signal ( $T_2$  cutoff at 40ms) largely originated from the broad middle peak, which is commonly designated as the IE water pool. There was not much contribution from a separate myelin water pool ( $T_{2s} < 40\text{ms}$ ) to the NNLS MWF, and the myelin water peak did not exist on the NNLS mean spectra for all ROIs. In contrast, the myelin water peak and its separation with the IE water peak were easily seen on the SAME-ECOS mean spectra for all ROIs (**Figure 6**), aligning with the intuitive interpretation of MWF arising entirely from a separate myelin water pool. Thus, this observation raises a concern that reporting MWF

values alone may not fully unveil the underlying information, especially for those myelin water imaging studies that used NNLS. Nevertheless, future studies using histological validation [111, 112] should be conducted to better compare these two analysis methods in dealing with experimental data.

#### **6.4.2 Advantages of SAME-ECOS**

The biggest advantage of SAME-ECOS lies in the fact that it is a simulation-derived solver, which takes a fundamentally different route to yield the solutions compared with conventional solvers such as NNLS. Its unique workflow makes SAME-ECOS highly tailorable to different experimental conditions and the needs of analysis. Most parameters used in SAME-ECOS are tunable. For example, the  $T_1$  parameter was set to be a constant for all  $T_2$  components in our simulation because the  $T_1$  weighting is minimized by using GRASE. But if a sequence sensitive to both  $T_1$  and  $T_2$  were used, one could simply turn the  $T_1$  parameter into another variable for the production of training data and make the training labels a 2D map that resolves distinct components with different  $T_1$ ,  $T_2$  times. [30] In contrast, it is presumably more difficult to include either  $T_1$  or any other quantities as an additional variable in the NNLS analysis. Another example would be how easily the influence of B1 inhomogeneity is handled. SAME-ECOS simply treats the refocusing FA as a variable when producing the simulated decay data to account for the FA variations caused by B1 inhomogeneity. However, the same problem was not solved using NNLS for many years until Prasloski et al. [176] proposed to integrate the stimulated echo correction into the original NNLS algorithm, which was a tremendous effort for such integration. Furthermore, if one wants to subject the data analysis to a simpler 3-pool model for instance, SAME-ECOS can easily be simplified to a 3-pool solver by fixing the number of  $T_2$  components to be  $n=3$  in the simulation, although it is not encouraged to do so for reasons discussed later. Conclusively, SAME-ECOS is extremely tunable to accommodate either a simpler or more complex model.

Another advantage of SAME-ECOS is to utilize the concept of resolution limit from information theory to prevent overfitting of noise. Due to unavoidable noise contamination,  $T_2$  components can only be recovered to a certain extent, and any

violation to the law of resolution limit should be theoretically prohibited. The essential part of SAME-ECOS workflow is to obey the resolution limit to prevent any solutions with adjacent  $T_2$  components being too close together, a feature which is not guaranteed in the solutions of NNLS or any other methods to our knowledge. One reasonable concern that is raised here is that nature does not know about resolution limits, so what happens when adjacent  $T_2$  components really are too close together? Unfortunately, the answer is that we might never resolve these two peaks in a solution where they are bound to degenerate into one peak due to the limited SNR, as Istratov et al. [89] pointed out about this particular problem: “Many physicists have discovered after much wasted effort that it is essential to understand the ill-conditioned nature of the problem before attempting to compute solutions”. On the other hand, the commonly used NNLS has incorporated regularization techniques [210] to mitigate the noise overfitting, but the choice of regularization parameters is poorly justified in most of the MR literature. From a technical perspective, the strength of regularization should be selected based on the local SNR rather than being universally fixed. Unfortunately, this has never been practiced in the NNLS analysis due to technical challenges. In addition, the noise of a magnitude MRI image originates from Gaussian distributed noise on both real and imaginary channels [27], which is not accounted for in the NNLS method [16] but is correctly modelled in the SAME-ECOS approach. Particularly in the last few echoes, when there is no residuals of MR signal (only pure noise), the noise profile would follow a Rayleigh distribution on the magnitude image that always has positive values, such that NNLS could misinterpret the Rayleigh noise as a long  $T_2$  component that has not been completely decayed yet. This phenomenon is observed in **Figure 6**, where NNLS mean spectra (red) for all ROIs always give a little rise on the far side of long  $T_2$ s ( $T_2 = 2000\text{ms}$ ), but SAME-ECOS mean spectra (blue) is free of this problem.

SAME-ECOS also takes advantage of the strong predictive power of a fine-tuned neural network. For regression problems such as our  $T_2$ -fitting task, modern machine learning methods like neural networks usually outperform conventional statistical methods in terms of better prediction accuracy and faster data processing speed [85], which is exactly what we have observed in our simulation tests. Out of various machine learning methods, the neural network approach is favored

for use in the current SAME-ECOS workflow because it has been successfully implemented in similar tasks by different research groups. [33, 124, 140] In theory, other machine learning methods may also achieve a similar predictive power. Comparisons between different machine learning methods are beyond the scope of this paper, but could be an area of future investigation.

Finally, it is worth highlighting that the simulated training dataset of SAME-ECOS is not informed by any prior knowledge (e.g. a 2-pool model is informed by the  $T_2$  times of myelin water and IE water, or a typical range of the MWF values obtained from previous studies). Instead, SAME-ECOS is completely driven by a large number of random simulations, which are only regulated by the experimental conditions such as SNR. This approach should be valued and favored because it is absolutely immune to (1) the potential errors of previous findings where the prior information is acquired from; (2) the biases that prior information may introduce into the analysis results. Simply speaking, an informed model is more likely to perform the analysis with a bias naturally towards the prior information. Similar to NNLS, no prior information being needed is a desirable and specially designed feature of SAME-ECOS.

### **6.4.3 Disadvantages of SAME-ECOS**

A major concern of SAME-ECOS is that its fitting results are not easily verified mathematically due to the use of a neural network. SAME-ECOS is capable of producing reliable results only on data that are similarly distributed as the training data. SAME-ECOS may become unpredictable and yield uninterpretable results when applied to unfamiliar data. Although we have generated a large training dataset by the simulations to account for many types of variations, there is no doubt that real experimental data have far more complexity in them. Factors such as artifacts are detrimental to any analysis methods, but SAME-ECOS is potentially less predictable. Unlike SAME-ECOS which empirically analyzes the data, conventional methods process the data either analytically or numerically, making them somewhat more mathematically explainable and predictable when encountering these problems.

Another limitation of SAME-ECOS is related to standardization. The variety

of parameters such as the  $T_2$  range, the noise profiles, the number of neural network hidden layers etc. can be manually selected at the user's will, which offers flexibility and customizability, but it is difficult to propose a standard SAME-ECOS model that works universally. The effects of changing these parameters warrants further investigation. Although SAME-ECOS demonstrated excellent performance in our simulation tests and in-vivo example application, users should further validate SAME-ECOS on their own experimental data before replacing any conventional analysis methods.

#### **6.4.4 Other quantitative MRI techniques and beyond**

Within MRI, the usage of SAME-ECOS is not just limited to multi-echo relaxation sequences. As long as the spins are trackable by simulations, then the SAME-ECOS methodology should also be applicable to other quantitative MRI techniques, such as multi-component driven equilibrium single pulse observation of  $T_1$  and  $T_2$  (mcDESPOT) [44] and neurite orientation dispersion and density imaging (NODDI) [236], by modifying the current workflow accordingly. Note that the analysis of mcDESPOT with their basis functions (and probably fingerprinting methods [144]) are conceptually similar to SAME-ECOS technique presented here but the resolution restrictions of different decay components are not considered. Beyond MRI, it is also possible to apply SAME-ECOS to any quantitative sciences that involve multi-exponential decays. In general, we believe a simulation-derived solver like SAME-ECOS is an alternative way to produce at least comparable results to conventional methods. It may deliver better performance, especially when analytical and numerical solutions start to fail due to factors such as a limited amount of data points and low SNR. Nevertheless, the SAME-ECOS methodology seems to have the potential to be generalized for the analysis of decay data within and beyond the MRI field.

### **6.5 Conclusion**

We have introduced a novel method SAME-ECOS, which can decompose multi-exponential MR relaxation data into a  $T_2$  spectrum. SAME-ECOS is highly tailorable to different experimental conditions and various analysis models. Com-

pared with the commonly used method NNLS, our results have demonstrated that SAME-ECOS can yield much more reliable  $T_2$  spectra and MWF values in a dramatically shorter processing time, by utilizing information theory and machine learning simultaneously.

## **Chapter 7**

# **Conclusion and future work**

### **7.1 Chapters recap**

Each chapter (from Chapter 2 to Chapter 6) in this thesis is specifically summarized in a short subsection below.

#### **7.1.1 MWI applied in CSM**

In Chapter 2, a common spinal cord neurodegenerative disease CSM was studied by MWI incorporated with the electrophysiologic technique SSEP. Although no significant MWF differences were found between the CSM and the control groups, significant MWF reduction ( $p < 0.05$ ) was observed in those CSM patients with functional deficits (e.g. delayed SSEP latency). Besides, in the CSM group, the SSEP latency only significantly correlated ( $p < 0.05$ ) with the MWF value, and such correlation was not found with other conventional parameters such as compression ratio, MCC, and MSCC. Our findings provide evidence of decreased myelin content in the spinal cord associated with impaired spinal cord conduction in patients with CSM. Therefore, MWI provides independent and complementary readouts to spinal cord compression, with a high specificity to detect impaired conduction.

### **7.1.2 MWI atlases**

In Chapter 3 & 4, MWI atlases for the spinal cord and the brain were created by averaging co-registered MWI images from many healthy individuals. The resulting atlases depict the population mean and regional variability of the healthy myelin content in distinct spinal cord pathways and different brain regions. Thus, the MWI atlases can be used as a normative reference to demonstrate areas of demyelination in individuals with pathological conditions such as MS. Future studies will expand the atlas age range, account for education, and other variables that may affect myelination.

### **7.1.3 MWI data analysis acceleration**

In Chapter 5, based on the NN algorithm, a super fast and easy to implement data analysis method was proposed for MWI to calculate the MWF. Using a common computer configuration, the trained NN achieved the production of a whole brain MWF map in approximately 33 seconds, which is 150 times faster compared with the ground truth NNLS method. Besides, the trained NN demonstrated almost perfect accuracy in different regions (e.g. brain, spinal cord, and lesion) and various conditions (e.g. SNR and multi-site). In summary, the time for accurate MWF calculation can be dramatically reduced to less than 1 minute by the proposed NN, addressing one of the barriers facing future clinical feasibility of MWI.

### **7.1.4 MWI data analysis accuracy improvement**

In Chapter 6, a novel  $T_2$  relaxation data analysis method SAME-ECOS was proposed by a combination use of the information theory and the NN algorithm. SAME-ECOS is a simulation-derived solver that tailored for different MR experimental conditions. Compared with the commonly used NNLS, analyzing MWI data by SAME-ECOS can yield a much more reliable  $T_2$  spectrum, which leads to a more accurate estimation in MWF. Besides, the calculation speed of SAME-ECOS is extremely fast due to the use of a trained NN. Finally, the methodology of SAME-ECOS has the potential to be generalized for data analysis within and beyond the MRI field.

## 7.2 Contributions of the thesis

The main focus of this thesis work was MWI, a myelin-specific imaging technique based on MR. Centring around MWI, the thesis expanded into multiple aspects of MWI (Figure 1.16). Retrospectively, the thesis started with one MWI application, followed by the creation of MWI atlases, and finally, finished by the improvements in the MWI analysis algorithm. In conclusion, the contributions of this thesis include the following:

1. demonstrated the correlation between the MWF values and the functional measurements for the first time;
2. created MWI atlases as normative references for the myelin distribution in the brain and the spinal cord;
3. achieved MWI data analysis in less than one minute;
4. proposed a novel  $T_2$  data analysis method SAME-ECOS that improves the accuracy of MWI metrics.

Collectively, this thesis provided more evidence for the usefulness of MWI, along with several methods to improve the feasibility of clinical use of MWI at an individual level.

## 7.3 Limitations of the thesis

There are a number of limitations regarding the MWI data acquisition and analysis used in this thesis.

1. The gold standard sequence for MWI is the MSE sequence, such as CPMG, if the scanning time is not a concern. However, the main MWI sequence used in this thesis was 32-echo GRASE, which fills the central k-space with spin echo signals but the peripheral k-space with gradient echo signals. Also, the TR (1500ms for the spinal cord, 1000ms for the brain) used in the GRASE sequence was not long enough to completely eliminate the  $T_1$  contrast. These compromises were made to achieve an acceptable scanning time but certainly affected the quality of the acquired data, which ideally should

be the pure  $T_2$  decay curve depicted by spin echoes only. Although integrating the EPG algorithm in the data analysis could account for the effect of short TR, the consequence of filling the peripheral k-space with gradient echoes was not modelled in the current analysis, and it is presumably difficult to model this effect. Recently, the compressed sensing (CS) technique was applied to accelerate the gold standard MSE sequence. [31, 54] These studies reported that the MWF maps produced from the CS-accelerated sequence were comparable to the MWF maps produced from the fully sampled gold standard sequence, making the CS acceleration a very promising approach to significantly shorten the scanning time of the ideal MWI sequence.

2. The acquired MWI data only cover the TE range from 10ms to 320ms. However, it is generally believed that the signals from some myelin water molecules (e.g.  $T_2 < 7$ ms as explained in Chapter 6) may already have decayed completely even at the first echo TE=10ms, and the signals from the long  $T_2$  component (such as CSF) may not have decayed completely at the last echo TE=320ms. The limited temporal coverage makes it impossible to recover the information of very short or very long  $T_2$  components, regardless of the analysis method being used. Since the short  $T_2$  is of most interest, pushing the measurements towards shorter echo times would be a direction for future MWI development. Note that the ultra-short echo (UTE, usually  $< 1$ ms) technique, although very hardware demanding, has been realized to directly probe the myelin content [145], thus UTE technique is out of the MWI regime and not discussed in this thesis.
3. When MWI was applied in the spinal cord (Chapter 2 & 3), only 1-2 spinal cord segments were covered due to technical challenges. The limited coverage hinders the MWI applicability in the spinal cord, especially for investigating the spinal cord injuries. For example, the MWF at levels above and below the injury epicenter would be very useful information, and could provide more correlations to the functional deficits.
4. In Chapter 3 & 4, the quality of registration to PAM50 and MNI templates was only qualitatively evaluated by visual inspection rather than assessed

quantitatively. Especially for the registration of brain images in Chapter 4, only simple FSL registration tools were applied, making the registration error a major concern of the created atlas. Fortunately, recent follow-up studies ([165] and unpublished) on the creation of myelin water atlas incorporated a more sophisticated template generation technique (Advanced Normalization Tools (ANTs)), which has demonstrated superior performance over the method of FSL template registration.

5. The NN algorithms used in Chapter 5 & 6 were not scale-invariant, requiring the 32-echo MWI data to be normalized by the first echo intensity. This data pre-processing method is conceptually simple but very costly for MWI. Because only a few early echoes contain the residual signal originated from the myelin water pool before its signal is decayed completely. Consequently, losing the first echo information could lead to underestimating the signal contribution from the myelin water pool. More strategic normalization approaches (e.g. extrapolating data to  $TE=0ms$ ) should be considered in future development.

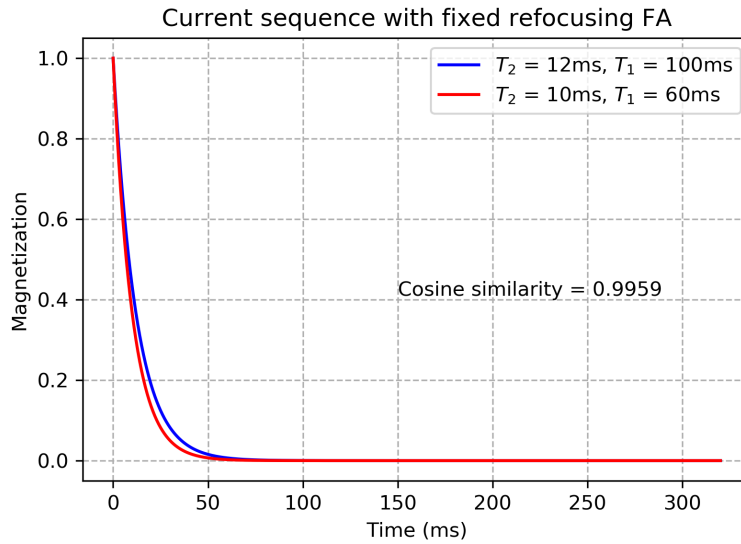
## 7.4 Future work

Finally, this thesis work unfolds many ideas for future studies. Among them, two ideas regarding SAME-ECOS stand out, and they are worth mentioning here.

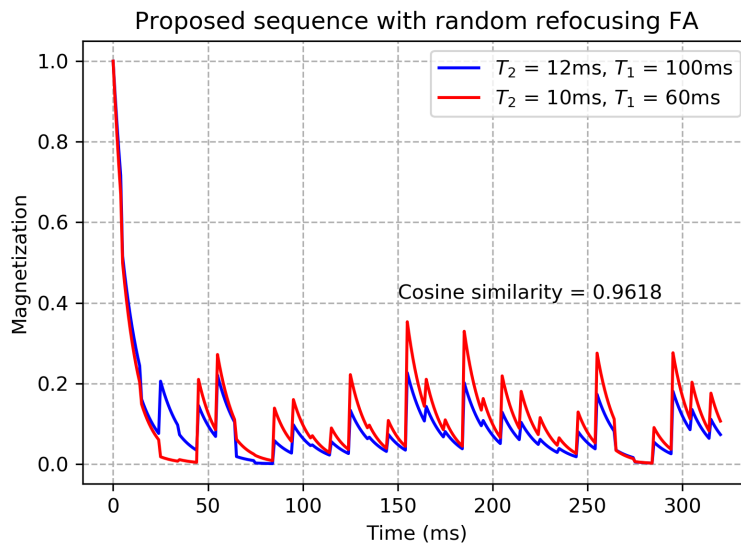
1. The current SAME-ECOS method is in its beta phase. Further improvements may rely on several points, including a more thorough simulation for the MR signal and the noise, a smarter choice of the NN or other algorithms, the use of regularization, etc. However, most importantly, histological validation of SAME-ECOS should be conducted to demonstrate whether the SAME-ECOS  $T_2$  spectrum, compared with using other analysis methods, has a better correlation with the microscopical structure of the tissue. This work would require a collaboration with other imaging techniques of much higher spatial resolution, such as scanning electron microscopy (SEM). Additionally, scan-rescan reproducibility studies can also be designed to demonstrate whether SAME-ECOS can produce similar enough results between scans, and has superior performance over other methods.

2. The current MWI sequence (MSE or GRASE) using  $90^\circ$  excitation followed by  $180^\circ$  refocusing pulses only explores the  $T_2$  characteristics and totally discards the information of  $T_1$ . Consequently, exponential decay curves generated from tissues with slightly different  $T_2$  values are often too similar to be distinguished even at high SNR and with the help of sophisticated analysis algorithms. The  $T_2$  resolution limit dictated by the nature of exponential analysis (as introduced in Chapter 6) seems to be an unbreakable barrier that prevents a solution of high precision. However, acquiring MWI data sensitive to both  $T_1$  and  $T_2$  by a different sequence might be an alternative way to go around such a fundamental limit.

In fact, the possibility of utilizing two-dimensional ( $T_1$  and  $T_2$ ) contrast have been investigated by others. [43, 48, 64] Based on these previous studies and inspired by the recent success of MR fingerprinting [144], an idea of prescribing random FA for excitation and refocusing pulses is conceived. To briefly demonstrate this idea, the evolution of transverse magnetization of two spins (spin 1:  $T_2=12\text{ms}$ ,  $T_1=100\text{ms}$ ; spin 2:  $T_2=10\text{ms}$ ,  $T_1=60\text{ms}$ ) driven by the current (excitation and refocusing FA =  $90^\circ$ ,  $180^\circ$ ) and proposed MWI sequences (excitation and refocusing FA = random choices in  $[0^\circ, 180^\circ]$ ) were simulated using Bloch equations (Figure 7.1). Clearly, the current MWI sequence produced two extremely similar decay curves (cosine similarity = 0.9959), whereas the proposed sequence generated two distinguishable evolution of the transverse magnetization (cosine similarity = 0.9618). It is also noticed that, when the  $T_2$  is short, the signals obtained by the current MWI sequence decay quickly and never come back, making the signal differences of the two spins only detectable within a small window (e.g.  $<50\text{ms}$  in the Figure 7.1(a)). In contrast, the signals obtained by the proposed sequence can maintain at a substantial intensity level during the entire measurement, leading to a much broader window to observe the signal differences. This advantage would eventually benefit the MWI data analysis as the range of 'useful' measurement for short  $T_2$  components (e.g. myelin water) is substantially larger. Similar to SAME-ECOS, a simulation-derived solver can be trained to map the measured signal to its underlying  $T_1$  and  $T_2$  proper-



(a) Current MWI sequence: refocusing FA =  $180^\circ$



(b) Proposed sequence: refocusing FA = random selections in  $[0^\circ, 180^\circ]$

**Figure 7.1: Motivation of random refocusing flip angle (FA).** The time evolution of transverse magnetization of two spins with similar  $T_2$  values driven by (a) the current and (b) proposed sequences are simulated using Bloch equations. Larger differences are observed with the proposed sequence.

ties. Note that the simulation for this idea presented here is preliminary, and further development is needed in the future.

# Bibliography

- [1] M. Abadi, A. Agarwal, P. Barham, E. Brevdo, Z. Chen, C. Citro, G. S. Corrado, A. Davis, J. Dean, M. Devin, et al. Tensorflow: Large-scale machine learning on heterogeneous distributed systems. *arXiv preprint arXiv:1603.04467*, 2016. → pages 82, 105
- [2] F. Aboitiz, A. B. Scheibel, R. S. Fisher, and E. Zaidel. Fiber composition of the human corpus callosum. *Brain research*, 598(1-2):143–153, Dec 11 1992. → page 70
- [3] A. Akhondi-Asl, O. Afacan, R. V. Mulkern, and S. K. Warfield. T2-relaxometry for myelin water fraction extraction using wald distribution and extended phase graph. In *International Conference on Medical Image Computing and Computer-Assisted Intervention*, pages 145–152. Springer, 2014. → pages 77, 100
- [4] A. L. Alexander, J. E. Lee, M. Lazar, and A. S. Field. Diffusion tensor imaging of the brain. *Neurotherapeutics*, 4(3):316–329, 7 2007. → pages 37, 46
- [5] T. S. Ali, T. A. Bjarnason, D. L. Senger, J. F. Dunn, J. T. Joseph, and J. R. Mitchell. Quantitative t2: interactive quantitative t2 mri witnessed in mouse glioblastoma. *Journal of medical imaging (Bellingham, Wash.)*, 2(3):036002, Jul 2015. → page 52
- [6] E. Alonso-Ortiz, I. R. Levesque, and G. B. Pike. Mri-based myelin water imaging: a technical review. *Magnetic resonance in medicine*, 73(1):70–81, 2015. → pages xvii, xviii, 21, 22
- [7] R. Ansorge and M. J. Graves. *The Physics and Mathematics of MRI*. Morgan & Claypool Publishers, 2016. → pages xvi, 7
- [8] M. Arshad, J. A. Stanley, and N. Raz. Adult age differences in subcortical myelin content are consistent with protracted myelination and unrelated to

diffusion tensor imaging indices. *NeuroImage*, 143:26–39, Dec 2016. → page 64

- [9] T. R. Baumeister, J. L. Kim, M. Zhu, and M. J. McKeown. White matter myelin profiles linked to clinical subtypes of parkinson’s disease. *Journal of magnetic resonance imaging : JMRI*, Nov 15 2018. → page 76
- [10] C. Beaulieu. The basis of anisotropic water diffusion in the nervous system - a technical review. *NMR in biomedicine*, 15(7-8):435–455, Nov-Dec 2002. → page 50
- [11] H. H. Berlet and B. Volk. Studies of human myelin proteins during old age. *Mechanisms of ageing and development*, 14(1-2):211–222, Sep-Oct 1980. → page 72
- [12] M. Bertero, P. Boccacci, and E. R. Pike. On the recovery and resolution of exponential relaxation rates from experimental data: a singular-value analysis of the laplace transform inversion in the presence of noise. *Proceedings of the Royal Society of London. A. Mathematical and Physical Sciences*, 383(1784):15–29, 1982. → page 100
- [13] T. Billiet, B. Madler, F. D’Arco, R. Peeters, S. Deprez, E. Plasschaert, A. Leemans, H. Zhang, B. V. den Bergh, M. Vandebulcke, E. Legius, S. Sunaert, and L. Emsell. Characterizing the microstructural basis of "unidentified bright objects" in neurofibromatosis type 1: A combined in vivo multicomponent t2 relaxation and multi-shell diffusion mri analysis. *NeuroImage.Clinical*, 4:649–658, Apr 13 2014. → page 76
- [14] T. Billiet, M. Vandebulcke, B. Madler, R. Peeters, T. Dhollander, H. Zhang, S. Deprez, B. R. V. den Bergh, S. Sunaert, and L. Emsell. Age-related microstructural differences quantified using myelin water imaging and advanced diffusion mri. *Neurobiology of aging*, 36(6):2107–2121, Jun 2015. → pages 64, 73
- [15] C. M. Bishop. *Pattern recognition and machine learning*. springer, 2006. → page 105
- [16] T. A. Bjarnason, C. R. McCreary, J. F. Dunn, and J. R. Mitchell. Quantitative t2 analysis: the effects of noise, regularization, and multivoxel approaches. *Magnetic Resonance in Medicine: An Official Journal of the International Society for Magnetic Resonance in Medicine*, 63(1):212–217, 2010. → page 116

- [17] C. Bjartmar and B. D. Trapp. Axonal and neuronal degeneration in multiple sclerosis: mechanisms and functional consequences. *Current opinion in neurology*, 14(3):271–278, 2001. → page 17
- [18] F. Bloch. Nuclear induction. *Physical review*, 70(7-8):460, 1946. → page 3
- [19] F. Block, W. Hansen, and M. Packard. The nuclear induction experiment. *Physical review*, 70(7-8):474–485, 1946. → page 2
- [20] S. D. Boden, P. R. McCowin, D. O. Davis, T. S. Dina, A. S. Mark, and S. Wiesel. Abnormal magnetic-resonance scans of the cervical spine in asymptomatic subjects. a prospective investigation. *The Journal of bone and joint surgery.American volume*, 72(8):1178–1184, Sep 1990. → page 37
- [21] M. R. Borich, A. L. Mackay, I. M. Vavasour, A. Rauscher, and L. A. Boyd. Evaluation of white matter myelin water fraction in chronic stroke. *NeuroImage.Clinical*, 2:569–580, Apr 21 2013. → pages 52, 64, 76
- [22] S. E. Boucher, M. A. Cypher, L. R. Carlock, and R. P. Skoff. Proteolipid protein gene modulates viability and phenotype of neurons. *Journal of Neuroscience*, 22(5):1772–1783, 2002. → page 17
- [23] M. Bouhrara, M. C. Maring, and R. G. Spencer. A simple and fast adaptive nonlocal multispectral filtering algorithm for efficient noise reduction in magnetic resonance imaging. *Magnetic resonance imaging*, 55:133–139, Jan 2019. → page 60
- [24] M. Bouhrara and R. G. Spencer. Rapid simultaneous high-resolution mapping of myelin water fraction and relaxation times in human brain using bmc-mcdespot. *NeuroImage*, 147:800–811, Feb 15 2017. → page 52
- [25] W. Bruck, A. Bitsch, H. Kolenda, Y. Bruck, M. Stiefel, and H. Lassmann. Inflammatory central nervous system demyelination: correlation of magnetic resonance imaging findings with lesion pathology. *Annals of Neurology*, 42(5):783–793, Nov 1997. → page 37
- [26] J. F. Budzik, V. Balbi, V. L. Thuc, A. Duhamel, R. Assaker, and A. Cotten. Diffusion tensor imaging and fibre tracking in cervical spondylotic myelopathy. *European radiology*, 21(2):426–433, Feb 2011. → pages 37, 46

- [27] A. Cárdenas-Blanco, C. Tejos, P. Irarrazaval, and I. Cameron. Noise in magnitude magnetic resonance images. *Concepts in Magnetic Resonance Part A: An Educational Journal*, 32(6):409–416, 2008. → pages 104, 116
- [28] H. Y. Carr and E. M. Purcell. Effects of diffusion on free precession in nuclear magnetic resonance experiments. *Physical review*, 94(3):630, 1954. → page 6
- [29] R. Carter. *The human brain book: An illustrated guide to its structure, function, and disorders*. Penguin, 2019. → page 15
- [30] H. Celik, M. Bouhrara, D. A. Reiter, K. W. Fishbein, and R. G. Spencer. Stabilization of the inverse laplace transform of multiexponential decay through introduction of a second dimension. *Journal of Magnetic Resonance*, 236:134–139, 2013. → page 115
- [31] H. S. Chen, A. Majumdar, and P. Kozlowski. Compressed sensing cpmg with group-sparse reconstruction for myelin water imaging. *Magnetic resonance in medicine*, 71(3):1166–1171, 2014. → page 123
- [32] M. M. Cheung, D. T. Li, E. S. Hui, S. Fan, A. Y. Ding, Y. Hu, and E. X. Wu. In vivo diffusion tensor imaging of chronic spinal cord compression in rat model. *Conference proceedings : ...Annual International Conference of the IEEE Engineering in Medicine and Biology Society.IEEE Engineering in Medicine and Biology Society. Annual Conference*, 2009:2715–2718, 2009. → page 46
- [33] O. Cohen, B. Zhu, and M. S. Rosen. Mr fingerprinting deep reconstruction network (drone). *Magnetic resonance in medicine*, 80(3):885–894, 2018. → pages 100, 117
- [34] J. Cohen-Adad, M. M. E. Mendili, S. Lehericy, P. F. Pradat, S. Blanche, S. Rossignol, and H. Benali. Demyelination and degeneration in the injured human spinal cord detected with diffusion and magnetization transfer mri. *NeuroImage*, 55(3):1024–1033, Apr 1 2011. → page 50
- [35] A. J. E. Combes, L. Matthews, J. S. Lee, D. K. B. Li, R. Carruthers, A. L. Traboulsee, G. J. Barker, J. Palace, and S. Kolind. Cervical cord myelin water imaging shows degenerative changes over one year in multiple sclerosis but not neuromyelitis optica spectrum disorder. *NeuroImage.Clinical*, 16:17–22, Jun 16 2017. → page 64
- [36] W. Commons. File:neuron hand-tuned.svg — wikimedia commons, the free media repository, 2019. → pages xvii, 16

- [37] A. Compston and A. Coles. Multiple sclerosis. *The Lancet*, 359(9313):1221–1231, 4/6 2002. → page 37
- [38] J. L. Cui, X. Li, T. Y. Chan, K. C. Mak, K. D. Luk, and Y. Hu. Quantitative assessment of column-specific degeneration in cervical spondylotic myelopathy based on diffusion tensor tractography. *European spine journal : official publication of the European Spine Society, the European Spinal Deformity Society, and the European Section of the Cervical Spine Research Society*, 24(1):41–47, Jan 2015. → page 37
- [39] A. Curt, H. J. V. Hedel, D. Klaus, V. Dietz, and E.-S. S. Group. Recovery from a spinal cord injury: significance of compensation, neural plasticity, and repair. *Journal of neurotrauma*, 25(6):677–685, Jun 2008. → page 39
- [40] J. Davies-Thompson, I. Vavasour, M. Scheel, A. Rauscher, and J. J. Barton. Reduced myelin water in the white matter tracts of patients with niemann-pick disease type c. *AJNR.American journal of neuroradiology*, 37(8):1487–1489, Aug 2016. → pages 64, 76
- [41] B. De Leener, S. Lévy, S. M. Dupont, V. S. Fonov, N. Stikov, D. L. Collins, V. Callot, and J. Cohen-Adad. Sct: Spinal cord toolbox, an open-source software for processing spinal cord mri data. *Neuroimage*, 145:24–43, 2017. → page 54
- [42] A. Demir, M. Ries, C. T. Moonen, J. M. Vital, J. Dehais, P. Arne, J. M. Caille, and V. Dousset. Diffusion-weighted mr imaging with apparent diffusion coefficient and apparent diffusion tensor maps in cervical spondylotic myelopathy. *Radiology*, 229(1):37–43, Oct 2003. → page 37
- [43] S. C. Deoni. Quantitative relaxometry of the brain. *Topics in magnetic resonance imaging: TMRI*, 21(2):101, 2010. → page 125
- [44] S. C. Deoni, B. K. Rutt, T. Arun, C. Pierpaoli, and D. K. Jones. Gleaning multicomponent t1 and t2 information from steady-state imaging data. *Magnetic Resonance in Medicine: An Official Journal of the International Society for Magnetic Resonance in Medicine*, 60(6):1372–1387, 2008. → pages 52, 96, 118
- [45] S. C. Deoni, J. R. Zinkstok, E. Daly, C. Ecker, M. A. Consortium, S. C. Williams, and D. G. Murphy. White-matter relaxation time and myelin water fraction differences in young adults with autism. *Psychological medicine*, 45(4):795–805, Mar 2015. → page 64

- [46] A. Deshmane, V. Gulani, M. A. Griswold, and N. Seiberlich. Parallel mr imaging. *Journal of Magnetic Resonance Imaging*, 36(1):55–72, 2012. → page 102
- [47] L. Dobaczewski, P. Kaczor, I. Hawkins, and A. Peaker. Laplace transform deep-level transient spectroscopic studies of defects in semiconductors. *Journal of applied physics*, 76(1):194–198, 1994. → page 103
- [48] M. D. Does. Inferring brain tissue composition and microstructure via mr relaxometry. *NeuroImage*, 182:136–148, 2018. → page 125
- [49] M. D. Does and R. E. Snyder. T2 relaxation of peripheral nerve measured in vivo. *Magnetic resonance imaging*, 13(4):575–580, 1995. → page 52
- [50] Y. P. Du, R. Chu, D. Hwang, M. S. Brown, B. K. Kleinschmidt-DeMasters, D. Singel, and J. H. Simon. Fast multislice mapping of the myelin water fraction using multicompartiment analysis of t decay at 3t: A preliminary postmortem study. *Magnetic Resonance in Medicine: An Official Journal of the International Society for Magnetic Resonance in Medicine*, 58(5):865–870, 2007. → pages 52, 77, 95, 100
- [51] T. Duval, A. Salianni, H. Nami, A. Nanci, N. Stikov, H. Leblond, and J. Cohen-Adad. Axons morphometry in the human spinal cord. *NeuroImage*, 185:119–128, Jan 15 2019. → page 59
- [52] T. Duval, S. L. Vy, N. Stikov, J. Campbell, A. Mezer, T. Witzel, B. Keil, V. Smith, L. L. Wald, E. Klawiter, and J. Cohen-Adad. g-ratio weighted imaging of the human spinal cord in vivo. *NeuroImage*, 145(Pt A):11–23, Jan 15 2017. → page 59
- [53] A. V. Dvorak, E. Ljungberg, I. M. Vavasour, H. Liu, P. Johnson, A. Rauscher, J. L. Kramer, R. Tam, D. K. Li, C. Laule, et al. Rapid myelin water imaging for the assessment of cervical spinal cord myelin damage. *NeuroImage: Clinical*, 23:101896, 2019. → pages 54, 82, 106
- [54] A. V. Dvorak, V. Wiggermann, G. Gilbert, I. M. Vavasour, E. L. MacMillan, L. Barlow, N. Wiley, P. Kozlowski, A. L. MacKay, A. Rauscher, et al. Multi-spin echo t2 relaxation imaging with compressed sensing (metrics) for rapid myelin water imaging. *Magnetic Resonance in Medicine*, 84(3):1264–1279, 2020. → page 123
- [55] C. A. Dyer. The structure and function of myelin: from inert membrane to perfusion pump. *Neurochemical research*, 27(11):1279–1292, 2002. → page 18

- [56] J. Edgar and J. Garbern. The myelinated axon is dependent on the myelinating cell for support and maintenance: molecules involved. *Journal of neuroscience research*, 76(5):593–598, 2004. → page 17
- [57] J. M. Edgar, M. McLaughlin, D. Yool, S.-C. Zhang, J. H. Fowler, P. Montague, J. A. Barrie, M. C. McCulloch, I. D. Duncan, J. Garbern, et al. Oligodendroglial modulation of fast axonal transport in a mouse model of hereditary spastic paraplegia. *The Journal of cell biology*, 166(1):121–131, 2004. → page 17
- [58] S. B. Eickhoff, K. E. Stephan, H. Mohlberg, C. Grefkes, G. R. Fink, K. Amunts, and K. Zilles. A new spm toolbox for combining probabilistic cytoarchitectonic maps and functional imaging data. *NeuroImage*, 25(4):1325–1335, May 1 2005. → page 66
- [59] B. M. Ellingson, S. N. Kurpad, and B. D. Schmit. Functional correlates of diffusion tensor imaging in spinal cord injury. *Biomedical sciences instrumentation*, 44:28–33, 2008. → page 47
- [60] B. M. Ellingson, N. Salamon, and L. T. Holly. Advances in mr imaging for cervical spondylotic myelopathy. *European spine journal : official publication of the European Spine Society, the European Spinal Deformity Society, and the European Section of the Cervical Spine Research Society*, 24 Suppl 2:197–208, Apr 2015. → pages 46, 47
- [61] I. Elshafiey, M. Bilgen, R. He, and P. A. Narayana. In vivo diffusion tensor imaging of rat spinal cord at 7 t. *Magnetic resonance imaging*, 20(3):243–247, Apr 2002. → page 50
- [62] S. E. Emery. Cervical spondylotic myelopathy: diagnosis and treatment. *The Journal of the American Academy of Orthopaedic Surgeons*, 9(6):376–388, Nov-Dec 2001. → page 36
- [63] S. E. Emery, H. H. Bohlman, M. J. Bolesta, and P. K. Jones. Anterior cervical decompression and arthrodesis for the treatment of cervical spondylotic myelopathy. two to seventeen-year follow-up. *The Journal of bone and joint surgery.American volume*, 80(7):941–951, Jul 1998. → page 36
- [64] A. English, K. Whittall, M. Joy, and R. Henkelman. Quantitative two-dimensional time correlation relaxometry. *Magnetic resonance in medicine*, 22(2):425–434, 1991. → page 125

- [65] T. D. Faizy, D. Kumar, G. Broocks, C. Thaler, F. Flottmann, H. Leischner, D. Kutzner, S. Hewera, D. Dotzauer, J. P. Stellmann, R. Reddy, J. Fiehler, J. Sedlacik, and S. Gellissen. Age-related measurements of the myelin water fraction derived from 3d multi-echo grase reflect myelin content of the cerebral white matter. *Scientific reports*, 8(1):14991–018–33112–8, Oct 9 2018. → pages 64, 73
- [66] T. D. Faizy, C. Thaler, D. Kumar, J. Sedlacik, G. Broocks, M. Grosser, J. P. Stellmann, C. Heesen, J. Fiehler, and S. Siemonsen. Heterogeneity of multiple sclerosis lesions in multislice myelin water imaging. *PloS one*, 11(3):e0151496, Mar 18 2016. → page 64
- [67] M. G. Fehlings, J. R. Wilson, B. Kopjar, S. T. Yoon, P. M. Arnold, E. M. Massicotte, A. R. Vaccaro, D. S. Brodke, C. I. Shaffrey, J. S. Smith, E. J. Woodard, R. J. Banco, J. R. Chapman, M. E. Janssen, C. M. Bono, R. C. Sasso, M. B. Dekutoski, and Z. L. Gokaslan. Efficacy and safety of surgical decompression in patients with cervical spondylotic myelopathy: results of the aospine north america prospective multi-center study. *The Journal of bone and joint surgery.American volume*, 95(18):1651–1658, Sep 18 2013. → page 43
- [68] C. Filley. *The Behavioural Neurology of White Matter*. Oxford University Press, New York, 2001. → pages 18, 50, 51
- [69] C. Filley. *The behavioral neurology of white matter*. Oxford University Press, 2012. → pages 63, 73
- [70] S. W. Flynn, D. J. Lang, A. L. Mackay, V. Goghari, I. M. Vavasour, K. P. Whittall, G. N. Smith, V. Arango, J. J. Mann, A. J. Dwork, P. Falkai, and W. G. Honer. Abnormalities of myelination in schizophrenia detected in vivo with mri, and post-mortem with analysis of oligodendrocyte proteins. *Molecular psychiatry*, 8(9):811–820, Sep 2003. → pages 37, 63, 73
- [71] M. Fukui, K. Chiba, M. Kawakami, S. Kikuchi, S. Konno, M. Miyamoto, A. Seichi, T. Shimamura, O. Shirado, T. Taguchi, K. Takahashi, K. Takeshita, T. Tani, Y. Toyama, E. Wada, K. Yonenobu, T. Tanaka, Y. Hirota, S. on Low Back Pain, and C. M. E. of the Clinical Outcome Committee of the Japanese Orthopaedic Association. Japanese orthopaedic association cervical myelopathy evaluation questionnaire (joacmeq): Part 2. endorsement of the alternative item. *Journal of orthopaedic science : official journal of the Japanese Orthopaedic Association*, 12(3):241–248, May 2007. → page 38

- [72] S. Gazdzinski, J. Kornak, M. W. Weiner, and D. J. Meyerhoff. Body mass index and magnetic resonance markers of brain integrity in adults. *Annals of Neurology*, 63(5):652–657, May 2008. → page 73
- [73] R. F. Gledhill, B. M. Harrison, and W. I. McDonald. Demyelination and remyelination after acute spinal cord compression. *Experimental neurology*, 38(3):472–487, Mar 1973. → page 46
- [74] E. L. Hahn. Spin echoes. *Physical review*, 80(4):580, 1950. → page 6
- [75] D. E. Haines. *Neuroanatomy: an atlas of structures, sections, and systems*, volume 153. Lippincott Williams & Wilkins, 2004. → page 59
- [76] J. Han, J. Pei, and M. Kamber. *Data mining: concepts and techniques*. Elsevier, 2011. → page 106
- [77] B. K. Hartman, H. C. Agrawal, D. Agrawal, and S. Kalmbach. Development and maturation of central nervous system myelin: comparison of immunohistochemical localization of proteolipid protein and basic protein in myelin and oligodendrocytes. *Proceedings of the National Academy of Sciences of the United States of America*, 79(13):4217–4220, Jul 1982. → page 72
- [78] A. Hazra, G. Lube, and H.-G. Raumer. Numerical simulation of bloch equations for dynamic magnetic resonance imaging. *Applied Numerical Mathematics*, 123:241–255, 2018. → pages xvi, 4
- [79] J. Hennig. Multiecho imaging sequences with low refocusing flip angles. *Journal of Magnetic Resonance (1969)*, 78(3):397–407, 1988. → pages 22, 104
- [80] S. Herculano-Houzel. The human brain in numbers: a linearly scaled-up primate brain. *Frontiers in Human Neuroscience*, 3:31, 2009. → page 15
- [81] S. J. Hickman and D. H. Miller. Imaging of the spine in multiple sclerosis. *Neuroimaging clinics of North America*, 10(4):689–704 ,viii, Nov 2000. → page 47
- [82] C. A. Holder, R. Muthupillai, S. M. Jr, J. D. Eastwood, and P. A. Hudgins. Diffusion-weighted mr imaging of the normal human spinal cord in vivo. *AJNR.American journal of neuroradiology*, 21(10):1799–1806, Nov-Dec 2000. → page 50

- [83] R. A. Horch, J. C. Gore, and M. D. Does. Origins of the ultrashort-t2 1h nmr signals in myelinated nerve: a direct measure of myelin content? *Magnetic resonance in medicine*, 66(1):24–31, Jul 2011. → page 37
- [84] K. Hornik, M. Stinchcombe, and H. White. Multilayer feedforward networks are universal approximators, 1989 1989. → page 79
- [85] K. Hornik, M. Stinchcombe, H. White, et al. Multilayer feedforward networks are universal approximators. *Neural networks*, 2(5):359–366, 1989. → pages 101, 116
- [86] Y. Hu, C. Y. Wen, T. H. Li, M. M. Cheung, E. X. Wu, and K. D. Luk. Somatosensory-evoked potentials as an indicator for the extent of ultrastructural damage of the spinal cord after chronic compressive injuries in a rat model. *Clinical neurophysiology : official journal of the International Federation of Clinical Neurophysiology*, 122(7):1440–1447, Jul 2011. → page 47
- [87] D. Hwang and Y. P. Du. Improved myelin water quantification using spatially regularized non-negative least squares algorithm. *Journal of magnetic resonance imaging : JMRI*, 30(1):203–208, Jul 2009. → pages 54, 77, 82
- [88] D. Hwang, D. H. Kim, and Y. P. Du. In vivo multi-slice mapping of myelin water content using t2\* decay. *NeuroImage*, 52(1):198–204, Aug 1 2010. → page 77
- [89] A. A. Istratov and O. F. Vyvenko. Exponential analysis in physical phenomena. *Review of Scientific Instruments*, 70(2):1233–1257, 1999. → pages 100, 103, 104, 116
- [90] T. Ito, K. Oyanagi, H. Takahashi, H. E. Takahashi, and F. Ikuta. Cervical spondylotic myelopathy. clinicopathologic study on the progression pattern and thin myelinated fibers of the lesions of seven patients examined during complete autopsy. *Spine*, 21(7):827–833, Apr 1 1996. → pages 37, 46
- [91] I. H. Jeong, J. Y. Choi, S. H. Kim, J. W. Hyun, A. Joung, J. Lee, and H. J. Kim. Comparison of myelin water fraction values in periventricular white matter lesions between multiple sclerosis and neuromyelitis optica spectrum disorder. *Multiple sclerosis (Houndmills, Basingstoke, England)*, 22(12):1616–1620, Oct 2016. → page 64
- [92] E. John. *SF-36 health survey: manual and interpretation guide*. Health Assessment Lab, 2000. → page 38

- [93] B. M. Keegan and J. H. Noseworthy. Multiple sclerosis. *Annual Review of Medicine*, 53:285–302, 2002. → page 90
- [94] M. Kerkovsky, J. Bednarik, L. Dusek, A. Sprlakova-Pukova, I. Urbanek, M. Mechl, V. Valek, and Z. Kadanka. Magnetic resonance diffusion tensor imaging in patients with cervical spondylotic spinal cord compression: correlations between clinical and electrophysiological findings. *Spine*, 37(1):48–56, Jan 1 2012. → page 47
- [95] D. P. Kingma and J. Ba. Adam: A method for stochastic optimization. *arXiv preprint arXiv:1412.6980*, 2014. → pages 82, 105
- [96] H. C. Kinney, J. Karthigasan, N. I. Borenshteyn, J. D. Flax, and D. A. Kirschner. Myelination in the developing human brain: biochemical correlates. *Neurochemical research*, 19(8):983–996, Aug 1994. → page 72
- [97] L. L. Kirkpatrick, A. S. Witt, H. R. Payne, H. D. Shine, and S. T. Brady. Changes in microtubule stability and density in myelin-deficient shiverer mouse cns axons. *Journal of Neuroscience*, 21(7):2288–2297, 2001. → page 17
- [98] S. C. Kirshblum, S. P. Burns, F. Biering-Sorensen, W. Donovan, D. E. Graves, A. Jha, M. Johansen, L. Jones, A. Krassioukov, M. Mulcahey, et al. International standards for neurological classification of spinal cord injury (revised 2011). *The journal of spinal cord medicine*, 34(6):535–546, 2011. → page 39
- [99] A. J. Kiruluta and R. G. González. Mr imaging: deconstructing timing diagrams and demystifying k-space. In *Handbook of clinical neurology*, volume 135, pages 21–37. Elsevier, 2016. → pages xvii, 13
- [100] G. Klambauer, T. Unterthiner, A. Mayr, and S. Hochreiter. Self-normalizing neural networks. In *Advances in neural information processing systems*, pages 971–980, 2017. → page 105
- [101] S. Kolind, L. Matthews, H. Johansen-Berg, M. I. Leite, S. C. Williams, S. Deoni, and J. Palace. Myelin water imaging reflects clinical variability in multiple sclerosis. *NeuroImage*, 60(1):263–270, Mar 2012. → pages 55, 64
- [102] S. Kolind, A. Seddigh, A. Combes, B. Russell-Schulz, R. Tam, V. Yogendrakumar, S. Deoni, N. A. Sibtain, A. Traboulsee, S. C. Williams, G. J. Barker, and P. A. Brex. Brain and cord myelin water imaging: a progressive multiple sclerosis biomarker. *NeuroImage.Clinical*, 9:574–580, Oct 3 2015. → page 60

- [103] P. Kozlowski, J. Liu, A. C. Yung, and W. Tetzlaff. High-resolution myelin water measurements in rat spinal cord. *Magnetic resonance in medicine*, 59(4):796–802, Apr 2008. → page 73
- [104] P. Kozlowski, D. Raj, J. Liu, C. Lam, A. C. Yung, and W. Tetzlaff. Characterizing white matter damage in rat spinal cord with quantitative mri and histology. *Journal of neurotrauma*, 25(6):653–676, Jun 2008. → page 52
- [105] J. K. Kramer, P. Taylor, J. D. Steeves, and A. Curt. Dermatomal somatosensory evoked potentials and electrical perception thresholds during recovery from cervical spinal cord injury. *Neurorehabilitation and neural repair*, 24(4):309–317, May 2010. → page 36
- [106] R. M. Kroeker and R. M. Henkelman. Analysis of biological nmr relaxation data with continuous distributions of relaxation times. *Journal of Magnetic Resonance (1969)*, 69(2):218–235, 1986. → pages 77, 100, 103
- [107] S. Kullmann, M. F. Callaghan, M. Heni, N. Weiskopf, K. Scheffler, H. U. Haring, A. Fritsche, R. Veit, and H. Preissl. Specific white matter tissue microstructure changes associated with obesity. *NeuroImage*, 125:36–44, Jan 15 2016. → page 73
- [108] S. Kullmann, F. Schweizer, R. Veit, A. Fritsche, and H. Preissl. Compromised white matter integrity in obesity. *Obesity reviews : an official journal of the International Association for the Study of Obesity*, 16(4):273–281, Apr 2015. → page 73
- [109] A. Kutzelnigg and H. Lassmann. Pathology of multiple sclerosis and related inflammatory demyelinating diseases. *Handbook of clinical neurology*, 122:15–58, 2014. → page 37
- [110] D. J. Lang, E. Yip, A. L. MacKay, A. E. Thornton, F. Vila-Rodriguez, G. W. MacEwan, L. C. Kopala, G. N. Smith, C. Laule, C. B. MacRae, and W. G. Honer. 48 echo t(2) myelin imaging of white matter in first-episode schizophrenia: evidence for aberrant myelination. *NeuroImage.Clinical*, 6:408–414, Oct 15 2014. → pages 64, 76
- [111] C. Laule, P. Kozlowski, E. Leung, D. K. Li, A. L. MacKay, and G. W. Moore. Myelin water imaging of multiple sclerosis at 7 t: correlations with histopathology. *Neuroimage*, 40(4):1575–1580, 2008. → pages 19, 37, 46, 52, 61, 64, 73, 77, 115

- [112] C. Laule, E. Leung, D. K. Li, A. Traboulsee, D. Paty, A. MacKay, and G. R. Moore. Myelin water imaging in multiple sclerosis: quantitative correlations with histopathology. *Multiple Sclerosis Journal*, 12(6):747–753, 2006. → pages 19, 37, 46, 52, 64, 73, 77, 115
- [113] C. Laule, I. M. Vavasour, S. H. Kolind, D. K. Li, T. L. Traboulsee, G. R. Moore, and A. L. MacKay. Magnetic resonance imaging of myelin. *Neurotherapeutics : the journal of the American Society for Experimental NeuroTherapeutics*, 4(3):460–484, Jul 2007. → pages 63, 73
- [114] C. Laule, I. M. Vavasour, S. H. Kolind, A. L. Traboulsee, G. R. Moore, D. K. Li, and A. L. Mackay. Long t2 water in multiple sclerosis: what else can we learn from multi-echo t2 relaxation? *Journal of neurology*, 254(11):1579–1587, Nov 2007. → page 52
- [115] C. Laule, I. M. Vavasour, E. Leung, D. K. Li, P. Kozlowski, A. L. Traboulsee, J. Oger, A. L. Mackay, and G. R. Moore. Pathological basis of diffusely abnormal white matter: insights from magnetic resonance imaging and histology. *Multiple sclerosis (Houndmills, Basingstoke, England)*, 17(2):144–150, Feb 2011. → page 52
- [116] C. Laule, I. M. Vavasour, G. R. Moore, J. Oger, D. K. Li, D. W. Paty, and A. L. MacKay. Water content and myelin water fraction in multiple sclerosis. a t2 relaxation study. *Journal of neurology*, 251(3):284–293, Mar 2004. → pages 61, 64, 73, 90, 96
- [117] C. Laule, I. M. Vavasour, E. Shahinfard, B. Madler, J. Zhang, D. K. B. Li, A. L. MacKay, and S. M. Sirrs. Hematopoietic stem cell transplantation in late-onset krabbe disease: No evidence of worsening demyelination and axonal loss 4 years post-allograft. *Journal of neuroimaging : official journal of the American Society of Neuroimaging*, 28(3):252–255, May 2018. → page 76
- [118] C. Laule, I. M. Vavasour, Y. Zhao, A. L. Traboulsee, J. Oger, J. D. Vavasour, A. L. Mackay, and D. K. Li. Two-year study of cervical cord volume and myelin water in primary progressive multiple sclerosis. *Multiple sclerosis (Houndmills, Basingstoke, England)*, 16(6):670–677, Jun 2010. → pages 47, 64, 76
- [119] C. Laule, A. Yung, V. Pavolva, B. Bohnet, P. Kozlowski, S. A. Hashimoto, S. Yip, D. K. Li, and G. W. Moore. High-resolution myelin water imaging in post-mortem multiple sclerosis spinal cord: A case report. *Multiple*

*sclerosis (Houndmills, Basingstoke, England)*, Jan 27 2016. → pages 37, 46, 73, 96

- [120] P. C. Lauterbur. Image formation by induced local interactions: examples employing nuclear magnetic resonance. *nature*, 242(5394):190–191, 1973. → page 8
- [121] C. L. Lawson and R. J. Hanson. *Solving least squares problems*. SIAM, 1995. → pages 21, 77, 100
- [122] D. R. Lebl, A. Hughes, and F. P. Cammisa. Cervical spondylotic myelopathy: Pathophysiology, clinical presentation, and treatment. *HSS Journal*, 7(2):170–178, Jul 2011. → page 36
- [123] Y. LeCun, Y. Bengio, and G. Hinton. Deep learning. *nature*, 521(7553):436–444, 2015. → page 105
- [124] J. Lee, D. Lee, J. Y. Choi, D. Shin, H.-G. Shin, and J. Lee. Artificial neural network for myelin water imaging. *Magnetic Resonance in Medicine*, 83(5):1875–1883, 2020. → page 117
- [125] J. G. Lee, S. Jun, Y. W. Cho, H. Lee, G. B. Kim, J. B. Seo, and N. Kim. Deep learning in medical imaging: General overview. *Korean journal of radiology*, 18(4):570–584, Jul-Aug 2017. → page 79
- [126] L. E. Lee, J. K. Chan, E. Nevill, A. Soares, I. M. Vavasour, E. L. MacMillan, H. Garren, D. Clayton, B. M. Keegan, R. Tam, A. L. Traboulsee, S. H. Kolind, and R. L. Carruthers. Advanced imaging findings in progressive solitary sclerosis: a single lesion or a global disease? *Multiple sclerosis journal - experimental, translational and clinical*, 5(1):2055217318824612, Jan 16 2019. → page 76
- [127] L. E. Lee, E. Ljungberg, D. Shin, C. R. Figley, I. M. Vavasour, A. Rauscher, J. Cohen-Adad, D. K. Li, A. L. Traboulsee, A. L. MacKay, et al. Inter-vendor reproducibility of myelin water imaging using a 3d gradient and spin echo sequence. *Frontiers in Neuroscience*, 12:854, 2018. → pages 64, 77, 82, 106
- [128] B. D. Leener, V. S. Fonov, D. L. Collins, V. Callot, N. Stikov, and J. Cohen-Adad. Pam50: Unbiased multimodal template of the brainstem and spinal cord aligned with the icbm152 space. *NeuroImage*, 165:170–179, Jan 15 2018. → page 54

- [129] B. D. Leener, S. Levy, S. M. Dupont, V. S. Fonov, N. Stikov, D. L. Collins, V. Callot, and J. Cohen-Adad. Sct: Spinal cord toolbox, an open-source software for processing spinal cord mri data. *NeuroImage*, Oct 5 2016. → pages 49, 80
- [130] I. R. Levesque, C. L. Chia, and G. B. Pike. Reproducibility of in vivo magnetic resonance imaging-based measurement of myelin water. *Journal of magnetic resonance imaging : JMRI*, 32(1):60–68, Jul 2010. → pages 54, 82
- [131] I. R. Levesque, P. S. Giacomini, S. Narayanan, L. T. Ribeiro, J. G. Sled, D. L. Arnold, and G. B. Pike. Quantitative magnetization transfer and myelin water imaging of the evolution of acute multiple sclerosis lesions. *Magnetic resonance in medicine*, 63(3):633–640, Mar 2010. → page 64
- [132] S. Levy, M. C. Guertin, A. Khatibi, A. Mezer, K. Martinu, J. I. Chen, N. Stikov, P. Rainville, and J. Cohen-Adad. Test-retest reliability of myelin imaging in the human spinal cord: Measurement errors versus region- and aging-induced variations. *PloS one*, 13(1):e0189944, Jan 2 2018. → page 59
- [133] R. S. Likes. Moving gradient zeugmatography, Dec. 22 1981. US Patent 4,307,343. → page 8
- [134] N. Link, S. Bauer, and B. Ploss. Analysis of signals from superposed relaxation processes. *Journal of applied physics*, 69(5):2759–2767, 1991. → pages 100, 103, 104
- [135] I. Lipp, D. K. Jones, S. Bells, E. Sgarlata, C. Foster, R. Stickland, A. E. Davidson, E. C. Tallantyre, N. P. Robertson, R. G. Wise, and V. Tomassini. Comparing mri metrics to quantify white matter microstructural damage in multiple sclerosis. *Human brain mapping*, 0(0), 03/19; 2019/04 2019. → page 51
- [136] F. Liu, L. Vidarsson, J. D. Winter, H. Tran, and A. Kassner. Sex differences in the human corpus callosum microstructure: a combined t2 myelin-water and diffusion tensor magnetic resonance imaging study. *Brain research*, 1343:37–45, Jul 9 2010. → page 66
- [137] H. Liu, E. Ljungberg, A. V. Dvorak, L. E. Lee, J. T. Yik, E. L. MacMillan, L. Barlow, D. K. Li, A. Traboulsee, S. H. Kolind, et al. Myelin water fraction and intra/extracellular water geometric mean t2 normative atlases

for the cervical spinal cord from 3t mri. *Journal of Neuroimaging*, 30(1):50–57, 2020. → pages 77, 82, 106

- [138] H. Liu, E. L. MacMillan, C. R. Jutzeler, E. Ljungberg, A. L. MacKay, S. H. Kolind, B. Madler, D. K. B. Li, M. F. Dvorak, A. Curt, C. Laule, and J. L. K. Kramer. Assessing structure and function of myelin in cervical spondylotic myelopathy: Evidence of demyelination. *Neurology*, Jul 12 2017. → pages 64, 76
- [139] H. Liu, C. Rubino, A. V. Dvorak, M. Jarrett, E. Ljungberg, I. M. Vavasour, L. E. Lee, S. H. Kolind, E. L. MacMillan, A. Traboulsee, et al. Myelin water atlas: a template for myelin distribution in the brain. *Journal of Neuroimaging*, 29(6):699–706, 2019. → pages 77, 82, 106
- [140] H. Liu, Q.-S. Xiang, R. Tam, A. V. Dvorak, A. L. MacKay, S. H. Kolind, A. Traboulsee, I. M. Vavasour, D. K. Li, J. K. Kramer, et al. Myelin water imaging data analysis in less than one minute. *NeuroImage*, 210:116551, 2020. → pages 100, 117
- [141] E. Ljungberg, I. Vavasour, R. Tam, Y. Yoo, A. Rauscher, D. K. Li, A. Traboulsee, A. MacKay, and S. Kolind. Rapid myelin water imaging in human cervical spinal cord. *Magnetic resonance in medicine*, 78(4):1482–1487, 2017. → pages 49, 51, 53, 54, 57, 80, 82, 106
- [142] S. Ljunggren. A simple graphical representation of fourier-based imaging methods. *Journal of Magnetic Resonance*, 54:338–343, 1983. → page 8
- [143] A. S. Lundervold and A. Lundervold. An overview of deep learning in medical imaging focusing on mri. *Zeitschrift für Medizinische Physik*, 29(2):102–127, 2019. → pages 79, 100
- [144] D. Ma, V. Gulani, N. Seiberlich, K. Liu, J. L. Sunshine, J. L. Duerk, and M. A. Griswold. Magnetic resonance fingerprinting. *Nature*, 495(7440):187–192, 2013. → pages 118, 125
- [145] Y.-J. Ma, A. C. Searleman, H. Jang, J. Wong, E. Y. Chang, J. Corey-Bloom, G. M. Bydder, and J. Du. Whole-brain myelin imaging using 3d double-echo sliding inversion recovery ultrashort echo time (desire ute) mri. *Radiology*, 294(2):362–374, 2020. → page 123
- [146] A. Mackay, K. Whittall, J. Adler, D. Li, D. Paty, and D. Graeb. In vivo visualization of myelin water in brain by magnetic resonance. *Magnetic resonance in medicine*, 31(6):673–677, 1994. → pages 19, 37, 51, 63, 66, 76, 82, 99, 103

- [147] E. L. MacMillan, B. Mädler, N. Fichtner, M. F. Dvorak, D. K. B. Li, A. Curt, and A. L. MacKay. Myelin water and t2 relaxation measurements in the healthy cervical spinal cord at 3.0t: Repeatability and changes with age. *NeuroImage*, 54(2):1083–1090, 1/15 2011. → pages 40, 47, 48, 61, 95, 96
- [148] B. Madler, S. A. Drabycz, S. H. Kolind, K. P. Whittall, and A. L. MacKay. Is diffusion anisotropy an accurate monitor of myelination? correlation of multicomponent t2 relaxation and diffusion tensor anisotropy in human brain. *Magnetic resonance imaging*, 26(7):874–888, Sep 2008. → page 40
- [149] C. J. Mahoney, I. J. Simpson, J. M. Nicholas, P. D. Fletcher, L. E. Downey, H. L. Golden, C. N. Clark, N. Schmitz, J. D. Rohrer, J. M. Schott, H. Zhang, S. Ourselin, J. D. Warren, and N. C. Fox. Longitudinal diffusion tensor imaging in frontotemporal dementia. *Annals of Neurology*, 77(1):33–46, Jan 2015. → page 64
- [150] P. Mandira. *What is gray matter a term for?* Socratic Q&A, May 2017. → pages xvii, 16
- [151] P. Manogaran, I. Vavasour, M. Borich, S. H. Kolind, A. P. Lange, A. Rauscher, L. Boyd, D. K. Li, and A. Traboulsee. Corticospinal tract integrity measured using transcranial magnetic stimulation and magnetic resonance imaging in neuromyelitis optica and multiple sclerosis. *Multiple sclerosis (Houndmills, Basingstoke, England)*, 22(1):43–50, Jan 2016. → pages 64, 76
- [152] P. Mansfield. Multi-planar image formation using nmr spin echoes. *Journal of Physics C: Solid State Physics*, 10(3):L55, 1977. → page 8
- [153] M. Matsumoto, Y. Fujimura, N. Suzuki, Y. Nishi, M. Nakamura, Y. Yabe, and H. Shiga. Mri of cervical intervertebral discs in asymptomatic subjects. *The Journal of bone and joint surgery.British volume*, 80(1):19–24, Jan 1998. → page 37
- [154] W. E. McCormick, M. P. Steinmetz, and E. C. Benzel. Cervical spondylotic myelopathy: make the difficult diagnosis, then refer for surgery. *Cleveland Clinic journal of medicine*, 70(10):899–904, Oct 2003. → page 36
- [155] C. R. McCreary, T. A. Bjarnason, V. Skihar, J. R. Mitchell, V. W. Yong, and J. F. Dunn. Multiexponential t2 and magnetization transfer mri of demyelination and remyelination in murine spinal cord. *NeuroImage*, 45(4):1173–1182, May 1 2009. → page 52

- [156] J. McWhirter and E. R. Pike. On the numerical inversion of the laplace transform and similar fredholm integral equations of the first kind. *Journal of Physics A: Mathematical and General*, 11(9):1729, 1978. → pages 100, 104
- [157] R. Mehanna and J. Jankovic. Movement disorders in multiple sclerosis and other demyelinating diseases. *Journal of the neurological sciences*, 328(1-2):1–8, May 15 2013. → page 37
- [158] S. Meiboom and D. Gill. Modified spin-echo method for measuring nuclear relaxation times. *Review of scientific instruments*, 29(8):688–691, 1958. → page 7
- [159] R. S. Menon, M. S. Rusinko, and P. S. Allen. Proton relaxation studies of water compartmentalization in a model neurological system. *Magnetic resonance in medicine*, 28(2):264–274, Dec 1992. → page 52
- [160] S. M. Meyers, S. H. Kolind, and A. L. MacKay. Simultaneous measurement of total water content and myelin water fraction in brain at 3t using a t2 relaxation based method. *Magnetic resonance imaging*, 37:187–194, Apr 2017. → page 61
- [161] S. M. Meyers, I. M. Vavasour, B. Madler, T. Harris, E. Fu, D. K. Li, A. L. Traboulsee, A. L. MacKay, and C. Laule. Multicenter measurements of myelin water fraction and geometric mean t2 : intra- and intersite reproducibility. *Journal of magnetic resonance imaging : JMRI*, 38(6):1445–1453, Dec 2013. → pages 64, 73
- [162] E. P. Minty, T. A. Bjarnason, C. Laule, and A. L. MacKay. Myelin water measurement in the spinal cord. *Magnetic resonance in medicine*, 61(4):883–892, Apr 2009. → pages 40, 47, 60
- [163] G. R. Moore, C. Laule, A. Mackay, E. Leung, D. K. Li, G. Zhao, A. L. Traboulsee, and D. W. Paty. Dirty-appearing white matter in multiple sclerosis: preliminary observations of myelin phospholipid and axonal loss. *Journal of neurology*, 255(11):1802–1811, Nov 2008. → page 37
- [164] S. Mori, K. Oishi, and A. V. Faria. White matter atlases based on diffusion tensor imaging. *Current opinion in neurology*, 22(4):362–369, Aug 2009. → page 73
- [165] S. R. Morris, R. D. Holmes, A. V. Dvorak, H. Liu, Y. Yoo, I. M. Vavasour, S. Mazabel, B. Mädler, S. H. Kolind, D. K. Li, et al. Brain myelin water

fraction and diffusion tensor imaging atlases for 9-10 year-old children. *Journal of Neuroimaging*, 30(2):150–160, 2020. → page 124

- [166] O. E. Mougin, R. C. Coxon, A. Pitiot, and P. A. Gowland. Magnetization transfer phenomenon in the human brain at 7 t. *NeuroImage*, 49(1):272–281, Jan 1 2010. → page 73
- [167] P. V. Mummaneni, M. G. Kaiser, P. G. Matz, P. A. Anderson, M. W. Groff, R. F. Heary, L. T. Holly, T. C. Ryken, T. F. Choudhri, E. J. Vresilovic, D. K. Resnick, J. S. on Disorders of the Spine, P. N. of the American Association of Neurological Surgeons, and C. of Neurological Surgeons. Cervical surgical techniques for the treatment of cervical spondylotic myelopathy. *Journal of neurosurgery.Spine*, 11(2):130–141, Aug 2009. → page 36
- [168] R. K. Murphy, P. Sun, R. H. Han, K. J. Griffin, J. M. Wagner, C. K. Yarbrough, N. M. Wright, I. G. Dorward, D. K. Riew, M. P. Kelly, P. Santiago, L. P. Zebala, K. Trinkaus, W. Z. Ray, and S. K. Song. Fractional anisotropy to quantify cervical spondylotic myelopathy severity. *Journal of neurosurgical sciences*, May 5 2016. → page 37
- [169] V. Nair and G. E. Hinton. Rectified linear units improve restricted boltzmann machines. In *Proceedings of the 27th International Conference on International Conference on Machine Learning, ICML'10*, pages 807–814, USA, 2010. Omnipress. → page 82
- [170] G. Nataraj, J. F. Nielsen, C. Scott, and J. A. Fessler. Dictionary-free mri perk: Parameter estimation via regression with kernels. *IEEE Transactions on Medical Imaging*, 37(9):2103–2114, Sep 2018. → pages 77, 97
- [171] A. Nouri, L. Tetreault, P. Cote, J. J. Zamorano, K. Dalzell, and M. G. Fehlings. Does magnetic resonance imaging improve the predictive performance of a validated clinical prediction rule developed to evaluate surgical outcome in patients with degenerative cervical myelopathy? *Spine*, 40(14):1092–1100, Jul 15 2015. → page 41
- [172] S. Nurick. The pathogenesis of the spinal cord disorder associated with cervical spondylosis. *Brain : a journal of neurology*, 95(1):87–100, 1972. → page 38
- [173] J. Oh, E. T. Han, D. Pelletier, and S. J. Nelson. Measurement of in vivo multi-component t2 relaxation times for brain tissue using multi-slice t2

prep at 1.5 and 3 t. *Magnetic resonance imaging*, 24(1):33–43, Jan 2006.  
→ page 77

- [174] K. Oshio and D. A. Feinberg. Grase (gradient-and spin-echo) imaging: a novel fast mri technique. *Magnetic resonance in medicine*, 20(2):344–349, 1991. → page 20
- [175] C. S. Poon and R. M. Henkelman. Practical t2 quantitation for clinical applications. *Journal of Magnetic Resonance Imaging*, 2(5):541–553, 1992. → pages 19, 20
- [176] T. Prasloski, B. Mädler, Q.-S. Xiang, A. MacKay, and C. Jones. Applications of stimulated echo correction to multicomponent t2 analysis. *Magnetic resonance in medicine*, 67(6):1803–1814, 2012. → pages 22, 40, 53, 65, 77, 78, 79, 81, 82, 84, 95, 104, 106, 115
- [177] T. Prasloski, A. Rauscher, A. L. MacKay, M. Hodgson, I. M. Vavasour, C. Laule, and B. Mädler. Rapid whole cerebrum myelin water imaging using a 3d grase sequence. *Neuroimage*, 63(1):533–539, 2012. → pages 20, 21, 65, 77, 80, 102
- [178] S. W. Provencher. Contin: a general purpose constrained regularization program for inverting noisy linear algebraic and integral equations. *Computer Physics Communications*, 27(3):229–242, 1982. → pages 77, 100
- [179] E. M. Purcell, H. C. Torrey, and R. V. Pound. Resonance absorption by nuclear magnetic moments in a solid. *Physical review*, 69(1-2):37, 1946.  
→ page 2
- [180] I. I. Rabi, S. Millman, P. Kusch, and J. R. Zacharias. The molecular beam resonance method for measuring nuclear magnetic moments. the magnetic moments of li 6 3, li 7 3 and f 19 9. *Physical review*, 55(6):526, 1939. → page 1
- [181] I. I. Rabi, J. R. Zacharias, S. Millman, and P. Kusch. A new method of measuring nuclear magnetic moment. *Physical Review*, 53(4):318, 1938.  
→ page 1
- [182] A. Rahimi and B. Recht. Random features for large-scale kernel machines. In *Advances in neural information processing systems*, pages 1177–1184, 2008. → page 97

- [183] C. S. Raine. Morphology of myelin and myelination. In *Myelin*, pages 1–50. Springer, 1984. → pages 15, 17
- [184] A. Raj, S. Pandya, X. Shen, E. LoCastro, T. D. Nguyen, and S. A. Gauthier. Multi-compartment t2 relaxometry using a spatially constrained multi-gaussian model. *PloS one*, 9(6):e98391, Jun 4 2014. → page 77
- [185] R. Rao. Neck pain, cervical radiculopathy, and cervical myelopathy: pathophysiology, natural history, and clinical evaluation. *Instructional course lectures*, 52:479–488, 2003. → page 36
- [186] M. Ries, R. A. Jones, V. Dousset, and C. T. Moonen. Diffusion tensor mri of the spinal cord. *Magnetic resonance in medicine*, 44(6):884–892, Dec 2000. → page 37
- [187] J. Riise and B. Pakkenberg. Stereological estimation of the total number of myelinated callosal fibers in human subjects. *Journal of anatomy*, 218(3):277–284, Mar 2011. → page 70
- [188] Roadnottaken. Transmission electron micrograph of a myelinated axon, generated and deposited into the public domain by the electron microscopy facility at trinity college, source: <http://en.wikipedia.org/wiki/myelin>, 2007. → pages xvii, 17
- [189] S. Ropele, T. Seifert, C. Enzinger, and F. Fazekas. Method for quantitative imaging of the macromolecular 1h fraction in tissues. *Magnetic resonance in medicine*, 49(5):864–871, May 2003. → pages 50, 63
- [190] B. Russell-Schulz, C. Laule, D. K. Li, and A. L. MacKay. What causes the hyperintense t2-weighting and increased short t2 signal in the corticospinal tract? *Magnetic resonance imaging*, 31(3):329–335, Apr 2013. → page 74
- [191] A. Saliani, B. Perraud, T. Duval, N. Stikov, S. Rossignol, and J. Cohen-Adad. Axon and myelin morphology in animal and human spinal cord. *Frontiers in neuroanatomy*, 11:129, Dec 22 2017. → page 59
- [192] S. D. Santis, M. Drakesmith, S. Bells, Y. Assaf, and D. K. Jones. Why diffusion tensor mri does well only some of the time: variance and covariance of white matter tissue microstructure attributes in the living human brain. *NeuroImage*, 89:35–44, Apr 1 2014. → page 64
- [193] C. Saunders, A. Gammerman, and V. Vovk. Ridge regression learning algorithm in dual variables. In *Proceedings of the Fifteenth International*

*Conference on Machine Learning, ICML '98*, pages 515–521, San Francisco, CA, USA, 1998. Morgan Kaufmann Publishers Inc. → page 96

- [194] J. Schmidhuber. Deep learning in neural networks: An overview. *Neural networks*, 61:85–117, 2015. → pages 25, 33, 78, 79, 100
- [195] F. R. Shapiro, S. D. Senturia, and D. Adler. The use of linear predictive modeling for the analysis of transients from experiments on semiconductor defects. *Journal of applied physics*, 55(10):3453–3459, 1984. → page 103
- [196] S. M. Sirrs, C. Laule, B. Madler, E. E. Brief, S. A. Tahir, C. Bishop, and A. L. MacKay. Normal-appearing white matter in patients with phenylketonuria: water content, myelin water fraction, and metabolite concentrations. *Radiology*, 242(1):236–243, Jan 2007. → pages 37, 64, 76
- [197] J. G. Sled. Modelling and interpretation of magnetization transfer imaging in the brain. *NeuroImage*, 182:128–135, Nov 15 2018. → page 73
- [198] J. G. Sled, I. Levesque, A. C. Santos, S. J. Francis, S. Narayanan, S. D. Brass, D. L. Arnold, and G. B. Pike. Regional variations in normal brain shown by quantitative magnetization transfer imaging. *Magnetic resonance in medicine*, 51(2):299–303, Feb 2004. → pages 50, 63
- [199] S. A. Smith, X. Golay, A. Fatemi, A. Mahmood, G. V. Raymond, H. W. Moser, P. C. van Zijl, and G. J. Stanisz. Quantitative magnetization transfer characteristics of the human cervical spinal cord in vivo: application to adrenomyeloneuropathy. *Magnetic resonance in medicine*, 61(1):22–27, Jan 2009. → page 50
- [200] S. M. Smith. Fast robust automated brain extraction. *Human brain mapping*, 17(3):143–155, Nov 2002. → page 80
- [201] S. M. Smith, M. Jenkinson, M. W. Woolrich, C. F. Beckmann, T. E. Behrens, H. Johansen-Berg, P. R. Bannister, M. De Luca, I. Drobnjak, D. E. Flitney, et al. Advances in functional and structural mr image analysis and implementation as fsl. *Neuroimage*, 23:S208–S219, 2004. → pages 40, 65
- [202] S. K. Song, S. W. Sun, W. K. Ju, S. J. Lin, A. H. Cross, and A. H. Neufeld. Diffusion tensor imaging detects and differentiates axon and myelin degeneration in mouse optic nerve after retinal ischemia. *NeuroImage*, 20(3):1714–1722, Nov 2003. → pages 50, 63

- [203] S. K. Song, S. W. Sun, M. J. Ramsbottom, C. Chang, J. Russell, and A. H. Cross. Dysmyelination revealed through mri as increased radial (but unchanged axial) diffusion of water. *NeuroImage*, 17(3):1429–1436, Nov 2002. → pages 50, 63
- [204] T. Song, W. J. Chen, B. Yang, H. P. Zhao, J. W. Huang, M. J. Cai, T. F. Dong, and T. S. Li. Diffusion tensor imaging in the cervical spinal cord. *European spine journal : official publication of the European Spine Society, the European Spinal Deformity Society, and the European Section of the Cervical Spine Research Society*, 20(3):422–428, Mar 2011. → page 37
- [205] G. J. Stanisiz, S. Webb, C. A. Munro, T. Pun, and R. Midha. Mr properties of excised neural tissue following experimentally induced inflammation. *Magnetic Resonance in Medicine: An Official Journal of the International Society for Magnetic Resonance in Medicine*, 51(3):473–479, 2004. → page 19
- [206] N. Stikov, J. S. Campbell, T. Stroh, M. Lavelee, S. Frey, J. Novek, S. Nuara, M. K. Ho, B. J. Bedell, R. F. Dougherty, I. R. Leppert, M. Boudreau, S. Narayanan, T. Duval, J. Cohen-Adad, P. A. Picard, A. Gasecka, D. Cote, and G. B. Pike. In vivo histology of the myelin g-ratio with magnetic resonance imaging. *NeuroImage*, 118:397–405, Sep 2015. → page 70
- [207] P. W. Stroman, C. Wheeler-Kingshott, M. Bacon, J. M. Schwab, R. Bosma, J. Brooks, D. Cadotte, T. Carlstedt, O. Ciccarelli, J. Cohen-Adad, A. Curt, N. Evangelou, M. G. Fehlings, M. Filippi, B. J. Kelley, S. Kollias, A. Mackay, C. A. Porro, S. Smith, S. M. Strittmatter, P. Summers, and I. Tracey. The current state-of-the-art of spinal cord imaging: methods. *NeuroImage*, 84:1070–1081, Jan 1 2014. → page 51
- [208] J. I. Tamir, F. Ong, S. Anand, E. Karasan, K. Wang, and M. Lustig. Computational mri with physics-based constraints: Application to multicontrast and quantitative imaging. *IEEE Signal Processing Magazine*, 37(1):94–104, 2020. → pages xvii, 15
- [209] W. Thomasson and J. Clark Jr. Analysis of exponential decay curves: A three-step scheme for computing exponents. *Mathematical Biosciences*, 22:179–195, 1974. → page 103
- [210] A. N. Tihonov. Solution of incorrectly formulated problems and the regularization method. *Soviet Math.*, 4:1035–1038, 1963. → pages 24, 77, 116

- [211] Z. O. Toktas, B. Tanrikulu, O. Koban, T. Kilic, and D. Konya. Diffusion tensor imaging of cervical spinal cord: A quantitative diagnostic tool in cervical spondylotic myelopathy. *Journal of craniovertebral junction & spine*, 7(1):26–30, Jan-Mar 2016. → page 37
- [212] J. L. Trotter, C. L. Wegescheide, and W. F. Garvey. Regional studies of myelin proteins in human brain and spinal cord. *Neurochemical research*, 9(1):133–146, Jan 1984. → page 72
- [213] M. N. Uddin, T. D. Figley, K. G. Solar, A. S. Shatil, and C. R. Figley. Comparisons between multi-component myelin water fraction, t1w/t2w ratio, and diffusion tensor imaging measures in healthy human brain structures. *Scientific reports*, 9(1):2500–019–39199–x, Feb 21 2019. → page 64
- [214] P. van Gelderen and J. H. Duyn. White matter intercompartmental water exchange rates determined from detailed modeling of the myelin sheath. *Magnetic resonance in medicine*, 81(1):628–638, Jan 2019. → page 73
- [215] W. S. Vargas, E. Monohan, S. Pandya, A. Raj, T. Vartanian, T. D. Nguyen, S. M. H. Rua, and S. A. Gauthier. Measuring longitudinal myelin water fraction in new multiple sclerosis lesions. *NeuroImage.Clinical*, 9:369–375, Sep 12 2015. → pages 64, 76
- [216] V. Vasilescu, E. Katona, V. Simplaceanu, and D. Demco. Water compartments in the myelinated nerve. iii. pulsed nmr results. *Experientia*, 34(11):1443–1444, Nov 15 1978. → page 52
- [217] I. M. Vavasour, C. Laule, D. K. Li, J. Oger, G. R. Moore, A. Traboulsee, and A. L. MacKay. Longitudinal changes in myelin water fraction in two ms patients with active disease. *Journal of the neurological sciences*, 276(1-2):49–53, Jan 15 2009. → pages 37, 64
- [218] I. M. Vavasour, D. K. Li, C. Laule, A. L. Traboulsee, G. R. Moore, and A. L. Mackay. Multi-parametric mr assessment of t(1) black holes in multiple sclerosis : evidence that myelin loss is not greater in hypointense versus isointense t(1) lesions. *Journal of neurology*, 254(12):1653–1659, Dec 2007. → page 61
- [219] M. Veilleux and J. R. Daube. The value of ulnar somatosensory evoked potentials (seps) in cervical myelopathy. *Electroencephalography and clinical neurophysiology*, 68(6):415–423, Nov 1987. → page 36

- [220] S. Wakana, A. Caprihan, M. M. Panzenboeck, J. H. Fallon, M. Perry, R. L. Gollub, K. Hua, J. Zhang, H. Jiang, P. Dubey, A. Blitz, P. van Zijl, and S. Mori. Reproducibility of quantitative tractography methods applied to cerebral white matter, 1 July 2007 2007. → page 84
- [221] D. J. West, R. P. A. G. Teixeira, T. C. Wood, J. V. Hajnal, J.-D. Tournier, and S. J. Malik. Inherent and unpredictable bias in multi-component despot myelin water fraction estimation, 15 July 2019 2019. → page 52
- [222] C. A. Wheeler-Kingshott and M. Cercignani. About "axial" and "radial" diffusivities. *Magnetic resonance in medicine*, 61(5):1255–1260, May 2009. → page 37
- [223] K. P. Whittall, M. J. Bronskill, and R. M. Henkelman. Investigation of analysis techniques for complicated nmr relaxation data. *Journal of Magnetic Resonance (1969)*, 95(2):221–234, 1991. → page 25
- [224] K. P. Whittall and A. L. MacKay. Quantitative interpretation of nmr relaxation data. *Journal of Magnetic Resonance (1969)*, 84(1):134–152, 1989. → pages 19, 22, 51, 54, 63, 76, 77, 82, 100
- [225] K. P. Whittall, A. L. MacKay, D. A. Graeb, R. A. Nugent, D. K. Li, and D. W. Paty. In vivo measurement of t2 distributions and water contents in normal human brain. *Magnetic resonance in medicine*, 37(1):34–43, Jan 1997. → pages 52, 77, 95
- [226] K. P. Whittall, A. L. MacKay, and D. K. Li. Are mono-exponential fits to a few echoes sufficient to determine t2 relaxation for in vivo human brain? *Magnetic Resonance in Medicine: An Official Journal of the International Society for Magnetic Resonance in Medicine*, 41(6):1255–1257, 1999. → pages 99, 103
- [227] K. P. Whittall, A. L. MacKay, D. K. Li, I. M. Vavasour, C. K. Jones, and D. W. Paty. Normal-appearing white matter in multiple sclerosis has heterogeneous, diffusely prolonged t(2). *Magnetic resonance in medicine*, 47(2):403–408, Feb 2002. → page 52
- [228] V. Wiggermann, I. M. Vavasour, S. Kolind, A. L. MacKay, G. Helms, and A. Rauscher. Non-negative least squares computation for in vivo myelin mapping using simulated multi-echo spin-echo t2 decay data. *NMR in Biomedicine*, page e4277, 2020. → page 25

- [229] A. D. Wright, M. Jarrett, I. Vavasour, E. Shahinfard, S. Kolind, P. van Donkelaar, J. Taunton, D. Li, and A. Rauscher. Myelin water fraction is transiently reduced after a single mild traumatic brain injury—a prospective cohort study in collegiate hockey players. *PloS one*, 11(2):e0150215, Feb 25 2016. → pages 64, 76
- [230] C. K. Yarbrough, R. K. Murphy, W. Z. Ray, and T. J. Stewart. The natural history and clinical presentation of cervical spondylotic myelopathy. *Advances in orthopedics*, 2012:480643, 2012. → page 37
- [231] K. Yonenobu, K. Abumi, K. Nagata, E. Taketomi, and K. Ueyama. Interobserver and intraobserver reliability of the japanese orthopaedic association scoring system for evaluation of cervical compression myelopathy. *Spine*, 26(17):1890–4; discussion 1895, Sep 1 2001. → page 38
- [232] Y. Yoo, T. Prasloski, I. Vavasour, A. MacKay, A. L. Traboulsee, D. K. Li, and R. C. Tam. Fast computation of myelin maps from mri t(2) relaxation data using multicore cpu and graphics card parallelization. *Journal of magnetic resonance imaging : JMRI*, 41(3):700–707, Mar 2015. → page 78
- [233] Y. Yoo and R. Tam. Non-local spatial regularization of mri t2 relaxation images for myelin water quantification. *Medical image computing and computer-assisted intervention : MICCAI ...International Conference on Medical Image Computing and Computer-Assisted Intervention*, 16(Pt 1):614–621, 2013. → pages 60, 77, 95
- [234] Y. L. Yu and S. J. Jones. Somatosensory evoked potentials in cervical spondylosis. correlation of median, ulnar and posterior tibial nerve responses with clinical and radiological findings. *Brain : a journal of neurology*, 108 ( Pt 2)(Pt 2):273–300, Jun 1985. → page 36
- [235] F. Zhang, Y. Wu, I. Norton, L. Rigolo, Y. Rathi, N. Makris, and L. J. O’Donnell. An anatomically curated fiber clustering white matter atlas for consistent white matter tract parcellation across the lifespan. *NeuroImage*, 179:429–447, Oct 1 2018. → page 73
- [236] H. Zhang, T. Schneider, C. A. Wheeler-Kingshott, and D. C. Alexander. Noddi: practical in vivo neurite orientation dispersion and density imaging of the human brain. *Neuroimage*, 61(4):1000–1016, 2012. → pages 96, 118

- [237] J. Zhang, S. H. Kolind, C. Laule, and A. L. MacKay. Comparison of myelin water fraction from multiecho t2 decay curve and steady-state methods. *Magnetic resonance in medicine*, 73(1):223–232, Jan 2015. → pages 74, 78
- [238] J. Zhang, I. Vavasour, S. Kolind, B. Baumeister, A. Rauscher, and A. L. MacKay. Advanced myelin water imaging techniques for rapid data acquisition and long t2 component measurements. *Proc. Int. Soc. Mag. Reson. Med*, 23, 2015. → pages 52, 74
- [239] Y. Zhang, M. Brady, and S. Smith. Segmentation of brain mr images through a hidden markov random field model and the expectation-maximization algorithm. *IEEE transactions on medical imaging*, 20(1):45–57, 2001. → page 108